ABSTRACT

MECHANISMS OF LAYER-TRANSFER RELATED TO SILICON-ON-INSULATOR STRUCTURES

by
Bo Chen

The objective of this dissertation was to study the mechanisms that affect an efficient hydrogenation process in silicon and to validate a hypothesis concerning the hydrogenation mechanism of pre-implanted silicon wafers under hydrogen-plasma processing. These studies are related to a general process. A trapping layer for hydrogen was introduced by ion beam implantation into the silicon wafer. Next, this wafer was hydrogenated using a hydrogen plasma. It was hypothesized that the trapping layer acts as a getterer for the hydrogen diffusing into the silicon wafer. It was found that a large amount of hydrogen could be absorbed in the trapping layer by hydrogen plasma processing. The depth of layer transfer and surface blistering could be controlled by the trapping layer after annealing.

This research focused on the mechanism of hydrogen plasma reacting with the buried, heavily disordered silicon layer, deep level defects in the wafer, and nano-/micro-crack growth enhanced by the effect of inertial gas bubbles and hydrogen plasma processing. This dissertation also studied suitable wafer bonding methods for a novel method to produce nanoscale silicon-on-insulator materials.

Silicon wafers were implanted by different elements (He, N, Ne, Ar) at appropriate energy. A hydrogen trapping layer formed in the depth of ~100 nm based on calculations. Two different types of trapping layers were formed, one composed of a vacancy cluster, and the other was a gas bubble formation.

In the trap layer, there were many vacancies, interstitials and micro-voids. Due to the presence in the plasma of molecular and atomic hydrogen and extremely strong acids H_3^+ and H_2^+, the surface of Si wafer could be modified by H^+, H_2^+, H_3^+ in H-plasma. The surface strained Si-Si bonds were damaged. H_2 readily dissociated, bound to the surface and diffused into the Si bulk at low temperatures (150~200 °C). At higher temperatures (300~350°C), the trapped in silane-like species was detrapped, and hydrogen atoms diffused deeper into the Si bulk. When these atoms met the buried disorder layer and bubbles, they formed another Si-H structure and molecular hydrogen accumulated in the interstitial voids.

In plasma-ion-immersion-implantation processing, compared with non-implantation samples, less hydrogen was trapped in the disordered structure and many hydrogen was trapped in the internal surface of the voids. Many small defects could be generated in normal H PIII processing. Inertial gas pre-implantation may help remove these small defects and produce good quality transferred layer in the later layer exfoliation

It is found that many voids could be generated in bonding wafers by using only RCA clean activation, annealed at temperature above 200 °C. These voids could not disappear until annealed to above 1050 °C. These voids were induced from dissociated H_2 from water and evaporated CH_x. Plasma activation and hot nitric acid activation for direct wafer bonding may be a good choice for SOI fabrication.

MECHANISMS OF LAYER-TRANSFER RELATED TO SILICON-ON-INSULATOR STRUCTURES

by
Bo Chen

A Dissertation
Submitted to the Faculty of
New Jersey Institute of Technology
In Partial Fulfillment of the Requirements for the Degree of
Doctor of Philosophy in Materials Science and Engineering

Interdisciplinary Program in Materials Science and Engineering

May 2004

APPROVAL PAGE

MECHANISMS OF LAYER-TRANSFER RELATED TO SILICON-ON-INSULATOR STRUCTURES

Bo Chen

Dr. William N. Carr, Dissertation Advisor — Date
Professor of Electrical and Computer Engineering, NJIT

Dr. Alexander Y. Usenko, Committee Member — Date
CTO of Silicon Wafer Technology Inc.

Dr. Yves Chabal, Committee Member — Date
Professor of Chemistry and Biomedical Engineering, Rutgers-New Brunswick

Dr. Nuggehalli M. Ravindra, Committee Member — Date
Professor of Physics, NJIT

Dr. Ken Chin, Committee Member — Date
Professor of Physics, NJIT

Dr. Robert Marcus, Committee Member — Date
Professor of Electrical and Computer Engineering, NJIT

BIOGRAPHICAL SKETCH

Author: Bo Chen

Degree: Doctor of Philosophy

Date: May 2004

Undergraduate and Graduate Education:

- Doctor of Philosophy in Materials Science and Engineering
  New Jersey Institute of Technology, Newark, NJ, 2004

- Master of Science in Materials Science and Engineering
  Nanjing University of Chemical Technology, Nanjing, P. R. China, 1996

- Bachelor of Science in Materials Engineering
  Yanshan University, Qinghuangdao, P. R. China, 1993

Major: Materials Science and Engineering

Presentation and Publications:

Bo Chen, A. Y. Usenko, W. N. Carr,
A New Method to Produce Silicon-on-Insulator Wafer by Ar Implantation with H-plasma Processing, presented in 50th AVS conference, Nov. 1-4, 2003, Baltimore, MD.

Bo Chen, Y. Jiang, A.Y. Usenko, W.N. Carr,
The SOI Exfoliation by Ar+ implantation with H+ Plasma Processing, presented at Annual APS March meeting 2003, March 2-7, Austin, TX.

B. Chen, A.Y. Usenko, W. N. Carr
Nano-crack Growth by Ar+ Implantation with H+ Plasma Processing for SOI Exfoliation, 17th Annual Symposium Laboratory for Surface Modification, February 27, 2003 Rutgers University, Piscataway, NJ.

A.Y. Usenko, W.N. Carr, Bo Chen,
Plasma Hydrogenation of A Buried Trap Layer in Silicon: Formation of A Platelet Layer, in: PV 2002-17 Plasma Processing XIV, ed. by G. S. Mathad, M. Yang, R. E. Sah, and M. D. Allendorf, presented at 201st Meeting of

Electrochemical Society, Philadelphia, PA, May 12-17, 2002, The Electrochemical Society, Pennington, NJ, pp.50-60, 2002.

A.Y. Usenko, W.N. Carr, B. Chen,
Hydrogen Platelet Layer in Silicon Formed From Hydrogen Trapped onto Microbubbles Of Gases, Materials Research Society Symposium Proceeding Vol.719E, 2002, pp.F9.6.1-F9.6.6, presented at MRS Spring Meeting, San Francisco, CA, April 1-5, 2002.

A.Y. Usenko, W.N. Carr, Bo Chen,
Transformation of Hydrogen Trapped onto Microbubbles into H Platelet Layer in Si , The Journal of Materials Science: Materials in Electronics, 14(5), 305~309, May 2003.

Bo Chen, Alexander Usenko, William Carr,
Hydrogen Layer Formed in the Implanted Wafer – An Important Step to Produce SOI Wafer, 2nd AIMS Materials Research Symposium, May 8, 2002, NJIT, Newark, NJ.

W.N. Carr, B. Chen, A.Y. Usenko,
Delamination of Crystalline Silicon Film from Substrate through Hydrogenation of Trap Layer, Annual American Physical Society March Meeting 2002, March 18 - 22, 2002, Indiana Convention Center; Indianapolis, Indiana.

To my beloved family

ACKNOWLEDGMENT

I would like to express my deepest appreciation to Prof. William Carr and Dr. Alexander Usenko, who not only served as my research advisors, providing valuable and countless resources, insight, and intuition, but also constantly gave me support, encouragement, and reassurance.

Special thanks are given to the other committee members: Prof. Yves Chabal, Prof. N. M. Ravindra and Prof. Ken Chin for their careful review and helpful suggestions.

I would also like to thanks Dr. Frank Martin and Mr. Stan Christman for FTIR measurement, Mr. Yingbing Jiang for TEM and Stuff Group in Cornell Nanofacility for their instruction of cleanroom processing.

I'm grateful to Mr. Tao Yan, Dr. Lijun Jiang and other fellow students who share their ideas and experience with the author.

Finally, I would like to thank my family and friends for their continuous moral support and best wishes.

TABLE OF CONTENTS

TABLE OF CONTENTS
(Continued)

Chapter **Page**

TABLE OF CONTENTS
(Continued)

Chapter **Page**

TABLE OF CONTENTS
(Continued)

Chapter **Page**

LIST OF TABLES

Table **Page**

LIST OF FIGURES

LIST OF FIGURES
(Continued)

Figure **Page**

LIST OF FIGURES
(Continued)

Figure **Page**

LIST OF FIGURES
(Continued)

Figure **Page**

CHAPTER 1

INTRODUCTION

1.1 What is SOI (Silicon-on-Insulator)

The SOI stands for "silicon on insulator". Unlike the existing bulk silicon wafers, SOI wafers consist of three layers: a thin, single crystal silicon layer (SOI) layer that is the surface on which the semiconductor devices are formed, an insulating layer underneath, and a substrate, which takes up most of thickness.

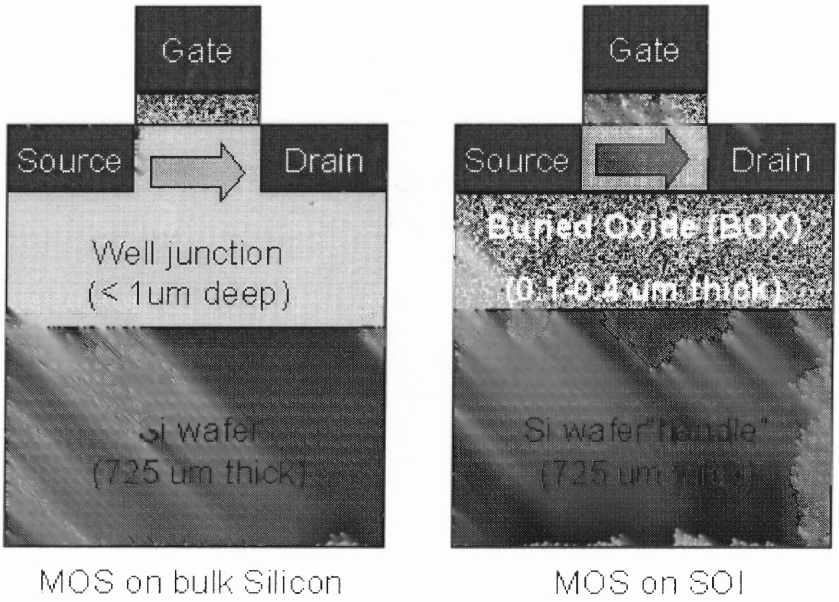

Figure 1.1 Sketch of metal-oxide-semiconductor (MOS) transistors on a bulk silicon wafer (left) and silicon-on-insulator(SOI) wafer (right).

In the field of semiconductor devices, where technology is advancing very rapidly, higher processing speeds and lower power consumptions are constantly demanded. The

challenge of reducing power consumption is said to be the most crucial challenge due to the popularity labtop PCs and PDA terminals. In view of this challenge, SOI technology is one of the technologies next-generation semiconductors that are getting the most attention these days.

Why and how do SOI wafers increase speed and reduce power consumption?

Current semiconductor devices are made with bulk silicon wafers with a thickness of hundreds of micons. However, only the portion that is less than 1 micron from the surface is actually used as a semiconductor device; the rest of the wafer functions mainly as a base board supporting the semiconductor device. When a semiconductor device is made of a bulk wafer, so-called "parasitic capacitance" is generated in the circuit on the substrate (Fig.1.2).

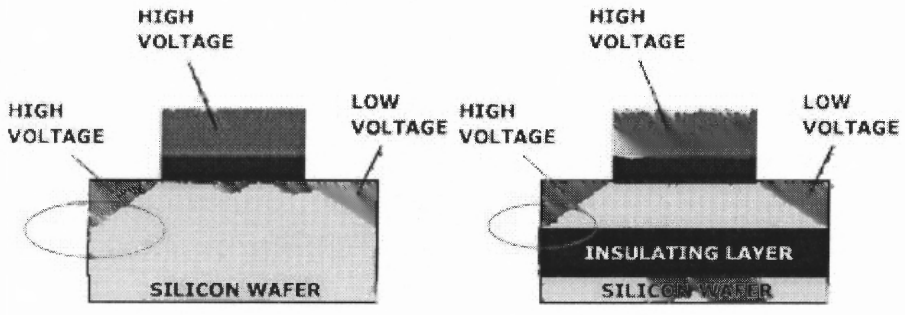

Figure 1.2 The parasitic capacitance between diffused source and drain and substrate.

The presence of such capacitance inhibits the start-up of current, limiting the

processing speed when instantaneous start-up of current is required. On the other hand, power consumption P can be expressed by the following equation

$$P=\Sigma CV^2f$$

Where C is the parasitic capacitance, V the driving voltage, and f the operating frequency. This equation suggests that parasitic capacitance has an adverse effect on power saving. In other words, by charging and discharging the parasitic capacitance, which becomes a load during operation, the device consumes excessive power needlessly. Since an SOI wafer has a single-crystal thin silicon layer (SOI layer) above the insulating layer, the semiconductor device formed in the SOI layer is not affected by the supporting substrate. Hence, a semiconductor device made with a SOI wafer allows current to be started immediately, with significantly reduced parasitic capacitance. In other words, both higher processing speeds and lower consumption can be expected.

The principal advantages of electrical devices fabricated in SOI wafers are:

(1) A 20% to 50% increase in switching speed compared to similar circuits built on conventional "bulk" silicon wafers.

(2) Because of high endurance in high temperature operation, cosmic ray and radiation, SOI technology has been used for a relatively long time in fields that require environmental endurance and fields such as aerospace.

(3) Increased circuit packing due to simplification of the lateral and vertical isolation structures, increasing chip yield and die count per wafer.

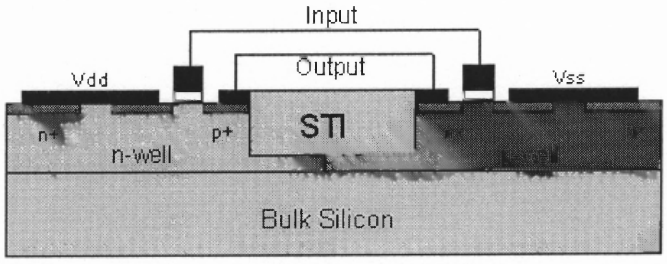

CMOS inverter on bulk Silicon

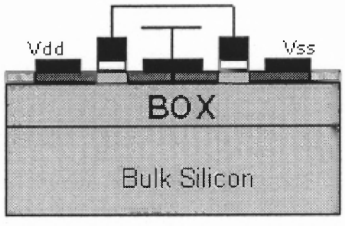

CMOS inverter on SOI

Figure1.3 CMOS inverter transistors on bulk silicon and SOI wafers sketched with the same gate size (critical dimensions). The smaller size of the SOI inverter is due to the more efficient isolation of SOI transistors.

After a long development history, Silicon-on-Insulator (SOI) technology has started to be used as the mainstream Silicon technology. Practical applications at present are mostly for high performance microprocessor using SOI CMOS[1], but the possibilities are expanding from high-speed/low-power logic Large-Scale-Integration Circuits (LSIs) to RF/analog LSIs, DRAMs, very low-voltage logic LSIs, imagers, system on a chip (SoC) and so on[2]. As a result, market demand for SOI wafers is rapidly increasing.

Over the last three decades, the main barrier to SOI as a substrate for mainstream applications is how to get high quality and low cost SOI material[3, 4, 6]. At present market, the commercial SOIs are mainly produced by two method, SIMOX[5] and Wafer-bonding technology[8].

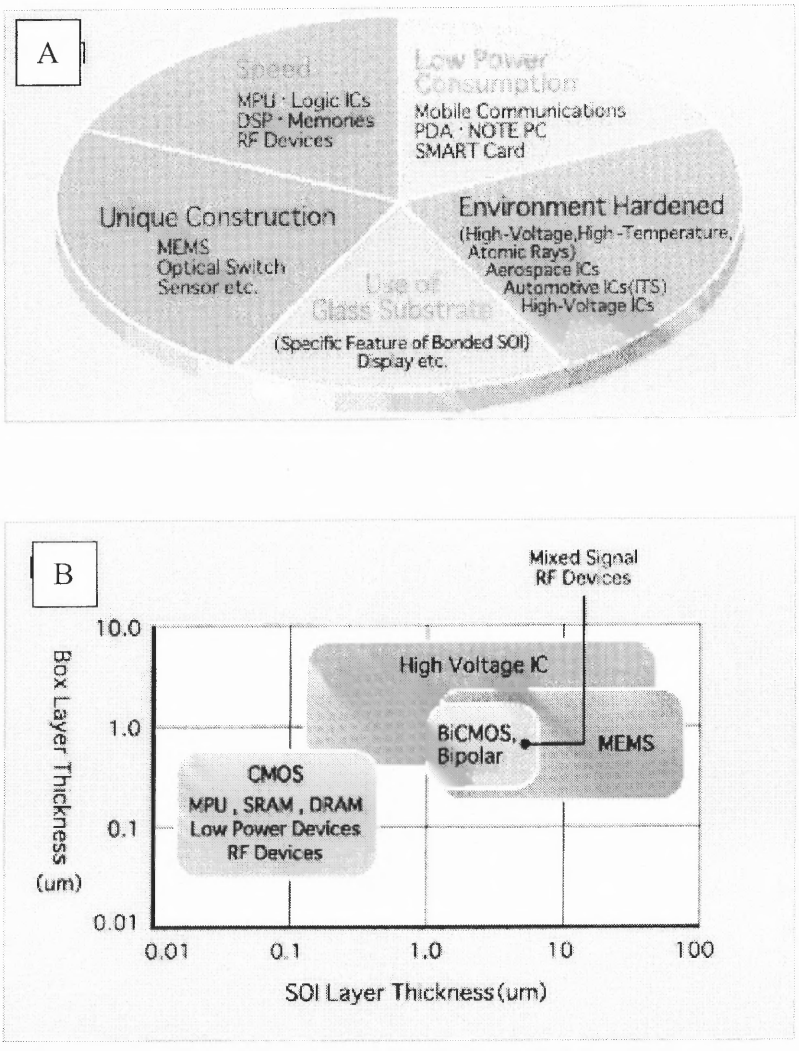

Figure 1.4 (a) Shows various application proposals for SOI technology according to its features; (b) Shows one per-device example of the thin film structure of an SOI wafer.

1.2 Brief Description of SIMOX

The acronym SIMOX stands for "Separation by IMplanted OXygen". In SIMOX, a high oxygen dose is implanted into a silicon wafer. Typical doses are in the $10^{18}/cm^2$ range at energies of 200-300 KeV. The implant leaves the wafers significantly damaged and the silicon near the surface is initially amorphous. The as-implanted wafer is annealed at temperatures above 1300 °C. This allows the implanted oxygen to chemically grow into a sub-surface layer of silicon dioxide through a process called Ostwald ripening, while simultaneously regrowing the surface amorphous silicon layer into crystalline silicon.

The process is conceptually simple but its execution relies on complex defect annihilation mechanisms. The important limitations of SIMOX include 1) low manufacturability/high cost [6], and 2) low buried oxide quality [7].

1.3 Wafer-bonding Technology for SOI Fabrication

The SOI manufacturing technology based on wafer-bonding is attracting attention for its capability to significantly reduce wafer production costs while ensuring high-quality (low defect level) SOI wafers[8]. In this method, two silicon wafers are bonded, and the SOI layer is formed. Then either silicon layer is peeled off and recycled for a new process. Canon (ELTRAN©), SOITEC (Smart-Cut©) have already implemented the manufacturing technique based on the concept.

1.3.1 ELTRAN (SOI-Epi) technology

SOI wafers are fabricated by bonding of epitaxial layers grown on top of porous silicon. This method has been called ELTRAN (Epitaxial Layer Transfer) and has been developed by Canon. It employs BESOI (bond and etch-back SOI) and the selective etching of porous silicon [9,10]. The method used involves combining BESOI with epitaxial growth on porous silicon that is capable of being etched with very high selectivity and surface smoothing by hydrogen annealing.

The ELTRAN manufacturing process consists of seven important processes:

- Anodization

A single-crystal silicon silicon wafer called a seed wafer is taken and porous silicon is formed on the surface by means of anodization. The anodization involves passing a current through a solution of HF and ethanol with the single-crystal silicon wafer as the anode in order to form microscopic pores of diameter a few nm on the surface of the wafer at a density of about $10^{11}/cm^2$.

- Epitaxial growth

Silicon epitaxial growth is carried out at about 1000~1100 °C in a hydrogen atmosphere in a CVD epitaxial reactor. Then, the surface of the epitaxial silicon layer is thermally oxidized. The resulting oxide film will become the BOX (buried oxide) film of the SOI wafer.

- Bonding and splitting

The surface of the thermally grown oxide film and the silicon handle wafer are pushed together at room temperature, upon which they bond to one another by van der waals forces. After that, heat treatment is carried out in order to form covalent bonds and thus strengthen the bonding between the two surfaces. The porous silicon layer in the bonded wafer has a double-layered structure. The bonded wafer is split parallel to its surface close to the interface between these two layers using a water-jet method.

- Selective Etching

The etching solution penetrates into the pores of the porous silicon by capillarity, and then etches into the walls of the porous in a sideways direction. Eventually, the porous structure collapse.

- Hydrogen annealing

After the porous silicon layer has been removed by selective etching, the epitaxial silicon/porous silicon interface is left at the SOI surface with a distinctive 'micro-roughness'. The surface will become atomically smooth by heat treatment in a hydrogen-contained atmosphere.

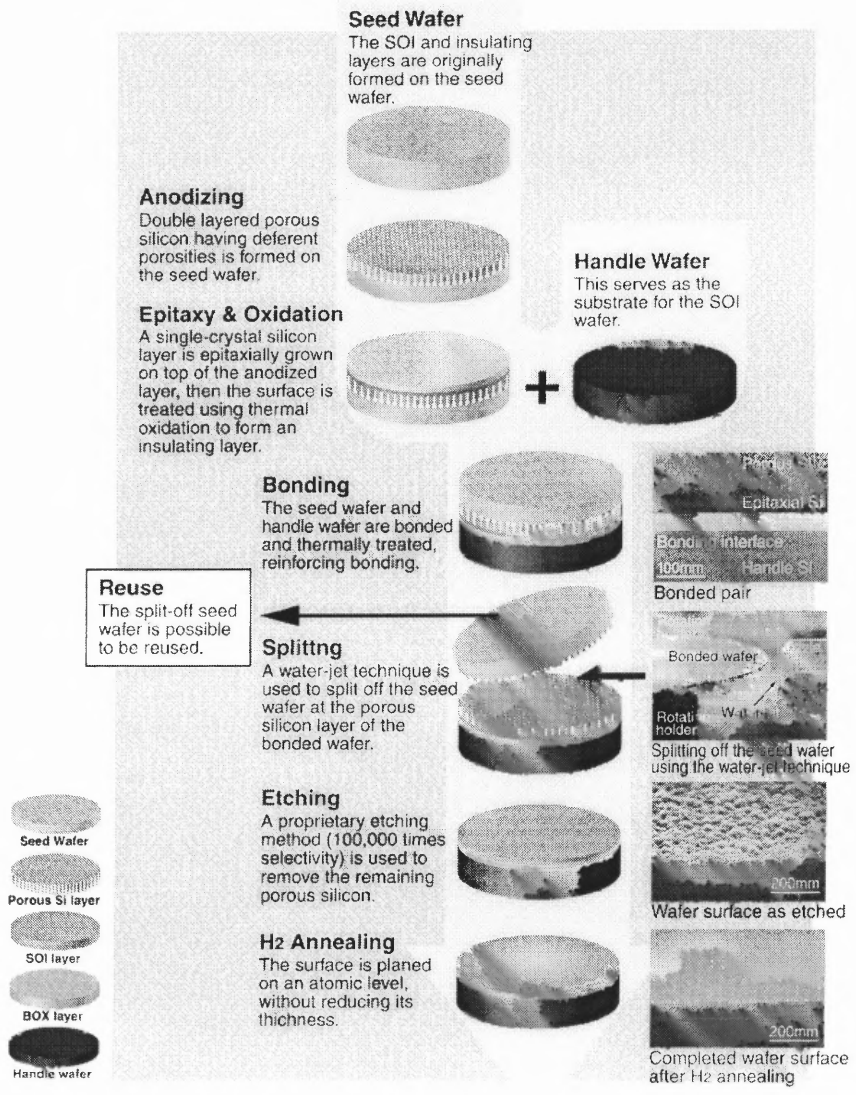

Figure 1.5 ELTRAN process for SOI wafer.

1.3.2 Description of Smart-cut process

The Smart-cut SOI fabrication combines ion implantation and wafer bonding technologies[11,12]. Ion implantation (hydrogen, helium etc.) induces formation of an in-depth weakened layer, located at the mean ion penetration depth, which leads to delamination of a thin film from a thick substrate (a process known as 'exfoliation'). Wafer bonding and layer transfer enable different materials to be associated to form multi-layer substrates. This process, first developed to obtain SOI, materials, is now an industrial process which provides high quality materials in large quantities [13,14]. As it enables a large number of material combinations to achieve, numerous studies are under way to develop new structures using this process. These new structures combining different materials and different bonding layers highlight the generic aspect of this process.

The Smart-cut process allows SOI wafers to be obtained following the different steps (Fig.1.6):

- A wafer is oxidized to form what will become the buried oxide layer of the SOI structure.
- A high dose ($\geq 5\times10^{16}$ ions/cm^2) hydrogen ion implantation through the oxide forms cavities or micro-bubbles at the implantation range.
- This wafer is bonded to another wafer using Van der Waals force.
- A 500 °C thermal activation merges all the hydrogen cavities, causing the top section of the wafer to delaminate.

This process has several advantages from both technical and economic points of view. Among these, the possibility of transferring thin layers of very good thickness

homogeneity and with a high crystalline quality onto different materials deserves to be highlighted. In Smart-cut, the long implantation time to attain high dose of hydrogen (5×10^{16} ions/cm^2) continues to be the major part of fabrication expense for the SOI wafers[15].

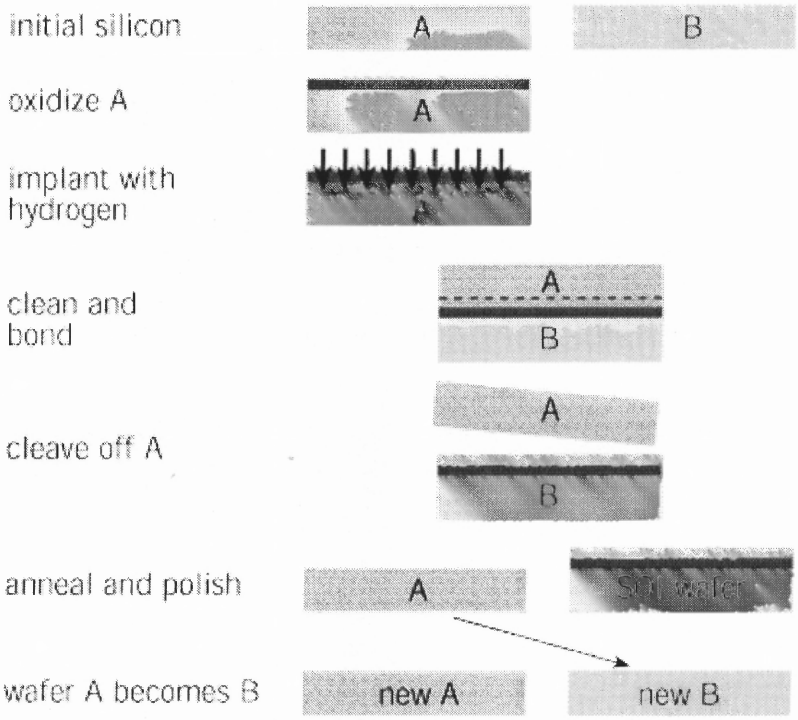

Figure 1.6 Schematic fabrication steps for Smart-cut process.

1.4 The Improvements to the Smart-cut Process

Many researchers want to use H^+ plasma as a cheap way to fabricate SOI wafer, for example plasma immersion ion implantation (PIII)[16,17,20]. Plasma immersion ion implantation (PIII) is a burgeoning technique offering many applications in materials and semiconductor processing. In PIII, the sample is immersed in plasma from which ion are extracted and accelerated through a high voltage sheath into the target (as shown at Fig 1.7). The use of PIII to synthesize SOI materials has been investigated for a long time, but the result seems not good[18,19]. In PIII, different hydrogen ion species exist in the plasma, such as H^+, H_2^+, and H_3^+, and all of them are co-implanted into the silicon wafer. The damage profile is different for each ion species due to different in the net impact energy (For example, each H atom in the H_3^+ molecular ion possesses 1/3 of the kinetic energy of the H atom in the H^+ atomic ion) and dose (for instance, there are three hydrogen atoms in each H_3^+), so the damage zone and H profile stretches all the way from the vicinity of the ion-projected range to the surface and will lead to final failure of layer transfer in SOI fabrication.

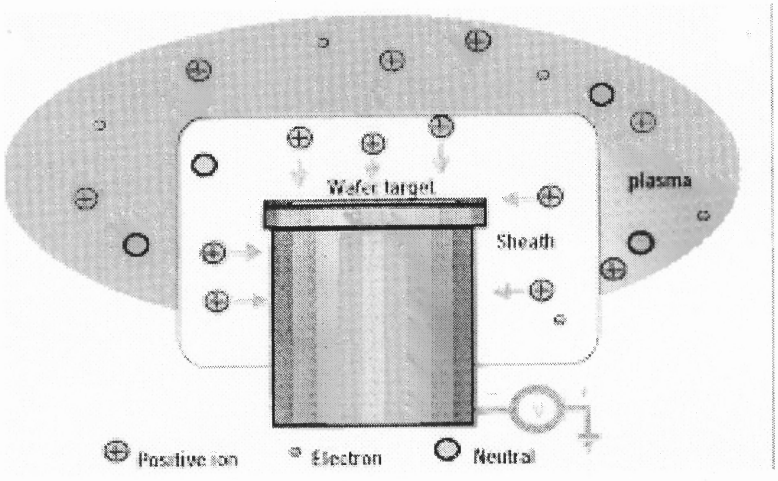

Figure 1.7 The concept of plasma immersion implantation (PIII) for SOI fabrication. The silicon wafer target is immersed in plasma from which hydrogen ions are extracted and accelerated through a high voltage sheath into the target.

1.5 New Process for SOI Fabrication

In this dissertation, noble gas implantation will be used to form buried disorder layer for hydrogen trapping, and hydrogen will be introduced by H-plasma through diffusion and trapping, then do wafer bonding and annealing to produce SOI finally [21-29].

1. The silicon wafer was implanted at appropriate temperature to form a buried disorder layer for trapping hydrogen

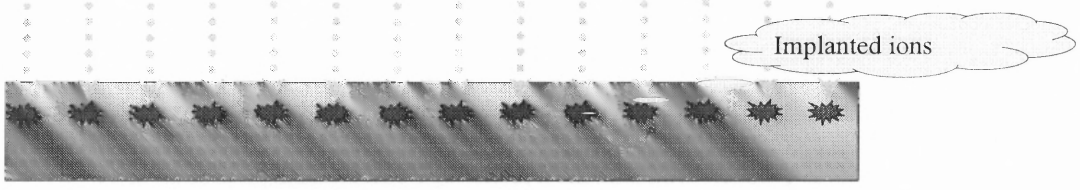

2. The implanted wafer was annealed at 600 °C before hydrogen plasma processing. The epitaxial growth consuming the disorder layer occurs from its both sides. The buried disorder layer will be thinner and bubbles may appear and grow.

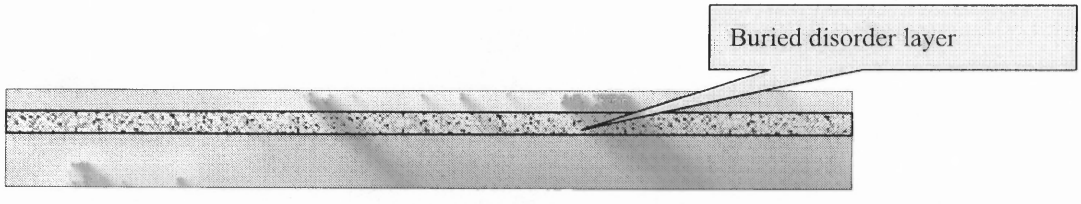

3. The wafer was processed by low energy or high energy H+ plasma. Hydrogen atoms pass through the top crystal layer, and then they are trapped by the buried disorder Si layer, by the internal surface and by bubbles.

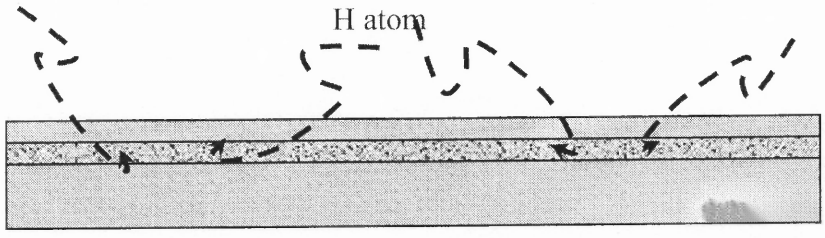

4. The hydrogenated wafer was bonded with another Si wafer which one surface was oxidized, forming a Si-Sandwich structure.

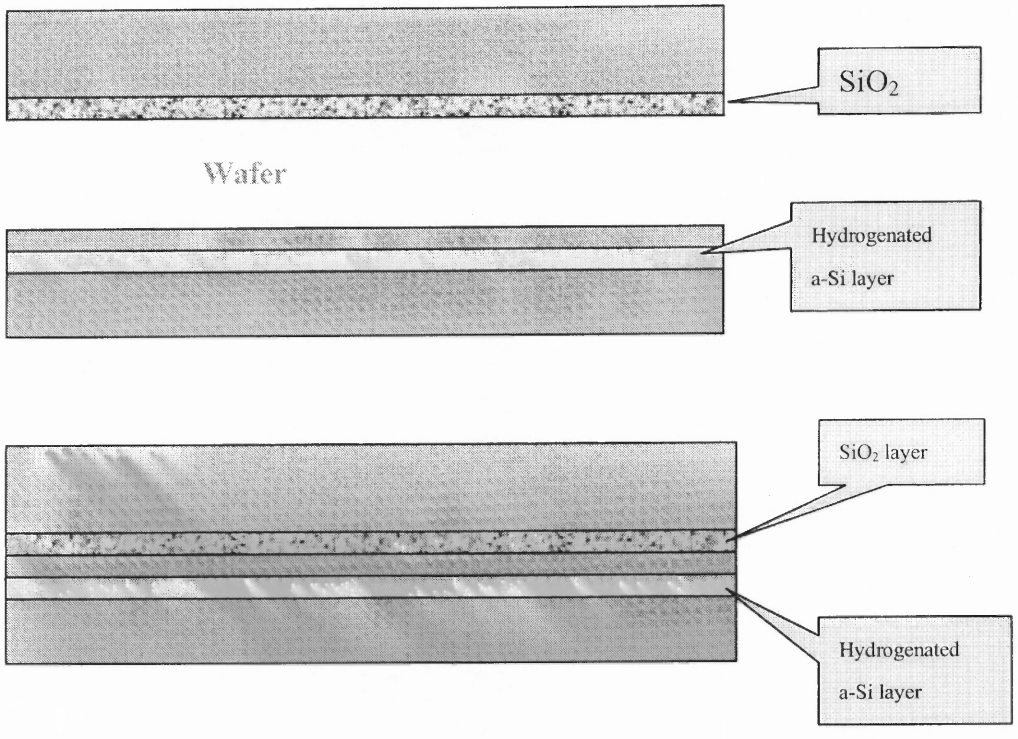

5. The bonded composite wafer was annealed at about 600 °C. Bubbles grow in the hydrogenated disorder layer. Layer exfoliation occurs along this layer.

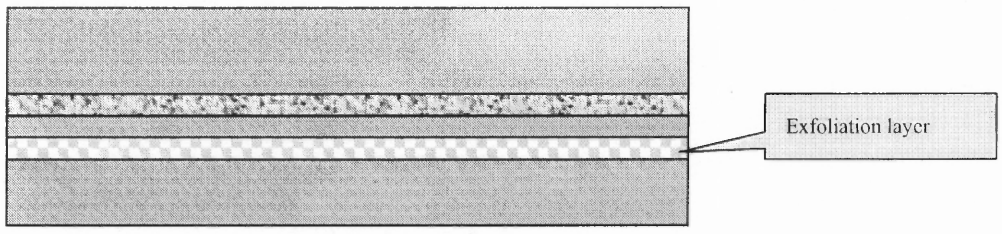

6. After annealing, layer transfer occurs. We can get good quality SOI wafer.

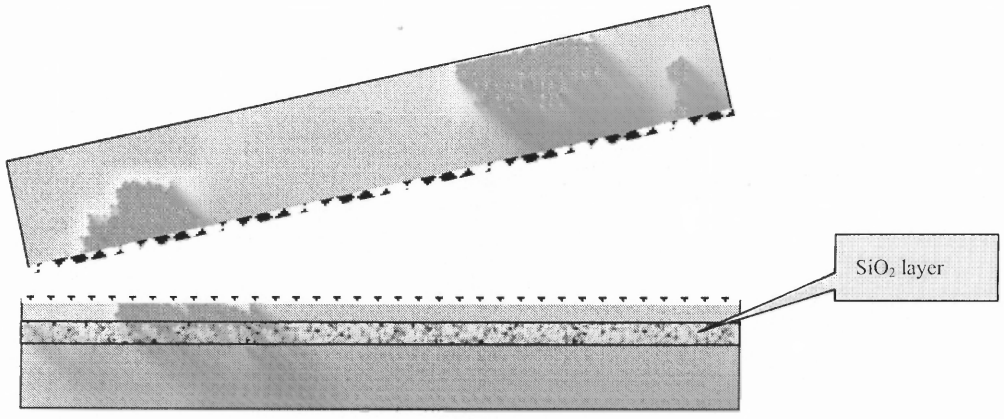

The proposed SOI fabrication technology has some advantages compared with SIMOX, Smart-Cut and PIII.

(1) The dose of noble gas implantation is about 10^{15}~10^{16}/cm^2, which is much lower than the implantation dose for Smart-Cut (>5×10^{16}/cm^{-2}) and SIMOX (~10^{18}/cm^{-2}), and the entire wafer is hydrogenated simultaneously by hydrogen plasma, thereby offering an extremely attractive approach for 300 mm wafers.

(2) The buried disorder layer is an efficient gettering site for impurity introduced by fabrication [30,31,32].

CHAPTER 2

THEORY AND SIMULATION OF HYDROGEN PLASMA PROCESSING

2.1 Fundamentals of H Plasma Physics [33-35]

2.1.1 Plasma Species

Let us now consider the interior of the hydrogen plasma, i.e., a partially ionized gas composed of respective densities of electrons (n_e), ions (n_i), and neutral gas species (n_0). Electrons and ions have more or less independent velocity distributions with electrons possessing far higher velocities than ions. On the average, the plasma is electrically neutral so that $n_e=n_i=n$. Collisions between neutral gas species essentially cause them to execute random Brownian motion. However, the applied electric field disrupts this haphazard motion because of ionization. If the density of charged particles is high enough compared with the dimensions of the plasma, significant columbic interaction exists among particles. This interaction enables the charged species to flow in a fluid-like fashion that determines many of the plasma properties.

The degree of gas ionization (f_i) is defined by

$$f_i = n_e/(n_e + n_0)$$

and typically has a magnitude of $\sim 10^{-4}$ in the glow discharges used in our hydrogenation processing.

2.1.2 Particle Energy and Temperatures

Measurements on glow discharges yield electron energies (Ee) that span the range 1 to 10 eV with 2~4 eV being a typical average value for calculation purposes. The effective or characteristic temperature T associated with a given energy E is simply given by $T=E/k_B$, where k_B is the Boltzmann constant. Substituting Ee=2eV, we find that electrons have an astoundingly high temperature T_e of some 23,000 K. However, because there are so few of them, their heat content is small and the chamber walls do not heat appreciably. Neutral gas atoms or molecules and ions are far less energetic. Ions have higher energies than neutrals because they acquire energy from the applied electric field.

2.1.3 Sheaths

The plasma sheath is a sharp interface between the bulk plasma and the chamber walls or any other material surface. Sheaths are particular important in our hydrogenation processing because their properties determine how charged particles from the plasma interact with the surface being processed. In particular, the energy and direction of ions striking the substrate is determined by their fall through the sheath. Voltage drops of tens to hundreds of volts can occur across sheaths, which impart kinetic energies of tens to hundreds of electron volts to the ions. These ion energies lead to chemical activation of surfaces in contact with the plasma.

2.1.4 Plasma Criteria

Ionized hydrogen gas can be characterized as plasmas if they meet three criteria

1. The system dimensions must considerably exceed sheath distance. Only in this way can the quasineutrality of the bulk of the plasma be ensured.

2. The total number (N_D) of shielding electrons drawn into the Debye sphere must be large; at very least N_D should be greater than unity.

3. Electrons should interact more strongly with each other than with the neutral gas. Under these conditions, particle motion in the plasma will be controlled by electromagnetic forces rather than by gas fluid dynamics.

2.2 Model Description of Hydrogen Plasma Processing [36-43]

A model that is capable of predicting the energy distribution function of ion bombarding a rf-biased electrode surface as a function of plasma operating conditions must be able to account for the spatiotemporal variation of the electric field and the potential distribution that accelerates the ions in the sheath. Since the electric field profiles depend on the charge distribution in the sheath, the model must also take into account the ion and electron density variations as a function of time and position. Thus, the equations that describe electron and ion transport are coupled to Poisson's equation which must be solved simultaneously and self-consistently for the charge and electric field distributions. The "sheath model" is used to calculate the spatiotemporal variation of the electric field, the sheath potential, the sheath thickness, the ion drift velocity, and the ion and electron concentrations given the time variation of the spatially integrated sheath potential across

the sheath. A nonlinear equivalent circuit model of the sheath is the second module and it is used to calculate the spatially integrated sheath potential wave form consistent with the given bias power and the sheath thickness as calculated in the sheath module. The final module is a Monte Carlo simulation that is used to compute the ion trajectories as they are accelerated by the electric fields that calculated self-consistently using the sheath and the equivalent circuit models.

We consider the sheath near a rf-biased electrode in a low pressure regime where collisions in the sheath may be neglected. The sheath thickness calculated using the model were typically several hundred microns, much less than the mean free path of ions and neutrals which is several millimeters at 10 mTorr. We assume that the sheath is infinite in the direction parallel to the electrode surface. The model geometry and coordinate system are shown in Fig. 2.1

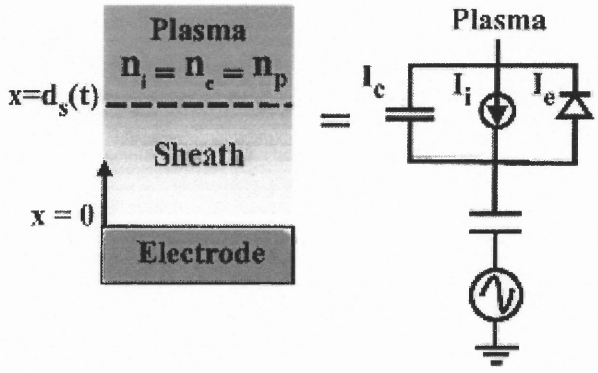

Figure 2.1 Model geometry and the equivalent circuit used to model the sheath.

The one-dimensional spatiotemporal variation of the ion density, $n_i(x,t)$, the ion drift velocity, $u_i(x,t)$, and the electric potential, $V_i(x,t)$ are described by the ion continuity equation,

$$\frac{\partial n_i}{\partial t} + \frac{\partial}{\partial x}(u_i n_i) = 0 \qquad (2\text{-}1)$$

the ion momentum balance

$$\frac{\partial u_i}{\partial t} + u_i \frac{\partial u_i}{\partial x} = -\frac{e}{m_i}\frac{\partial V}{\partial x} \qquad (2\text{-}2)$$

and the Poisson's equation

$$\frac{\partial^2 V}{\partial x^2} = -\frac{e}{\varepsilon_0}(n_i - n_e) \qquad (2\text{-}3)$$

In Eqs. (2-1)-(2-3) e is the electron charge, ε_0 is the permittivity of free space, and m_i is the ion mass. The three equations are not only coupled to each other but also to the electron density, n_e. We assume that the energy distribution of the electrons in the plasma is given by a Maxwell-Boltzmann distribution and characterized by an electron

temperature T_e. Furthermore, we limit ourselves to bias frequencies in the radio frequency range and well below the electron plasma frequency such that the electrons respond to the changes in the potential instantaneously. With these assumptions and taking the potential at the plasma-sheath edge to be zero, the reference potential, the electron density as a function of position in the sheath is given by

$$n_e(x,t) = n_p \exp(\frac{eV(x,t)}{kT_e}) \tag{2-4}$$

where n_p is the electron density at the plasma-sheath boundary and k is the Boltzmann's constant.

Suitable boundary conditions at the plasma-sheath interface must be chosen to completely define the problem. Artificial delineation of the sheath from the plasma forces one to define the sheath-boundary. We take the plasma-sheath interface as the point at which the electric field has increased to $kT_e / 2e\lambda_D$ where $\lambda_D = (\varepsilon_0 kT_e / n_p e^2)^{1/2}$ is the Debye length. This is the field required to accelerate the ions to the Bohm velocity across a distance equal to one Debye length. In terms of the potential this boundary condition may be written as

$$\frac{\partial V}{\partial x} = \frac{kT_e}{2e\lambda_D}, \text{ at x=ds(t)} \tag{2-5}$$

where ds(t) is the time dependent sheath thickness. Since potential reference can be taken arbitrarily, we set

$$\text{V=0, at x=ds(t)} \tag{2-6}$$

$$V=Ve(t), \text{ at } x=0 \qquad (2\text{-}7)$$

Ve(t) is obtained by coupling this model to an equivalent circuit model of sheath. We note that only two boundary conditions are needed to solve for V(x,t); the third boundary condition defines the location of the sheath, ds(t), as a function of time. Consistent with boundary condition (2-5), we assume that the ions enter the sheath with a velocity equal to the Bohm velocity and use

$$u_B = \sqrt{\frac{kT_e}{m_i}} \qquad \text{at } x=ds(t) \qquad (2\text{-}8)$$

as a boundary condition for the ion velocity. Finally, we assume that the ion density at the plasma-sheath edge is known:

$$n=n_p, \text{ at } x=ds(t)$$

A bulk plasma model would normally provide the concentration at this location and two solutions would be matched at the plasma-sheath interface.

2.3 Simulation Model and Result of Tegal-100 Plasma System

2.3.1 Equipment Description

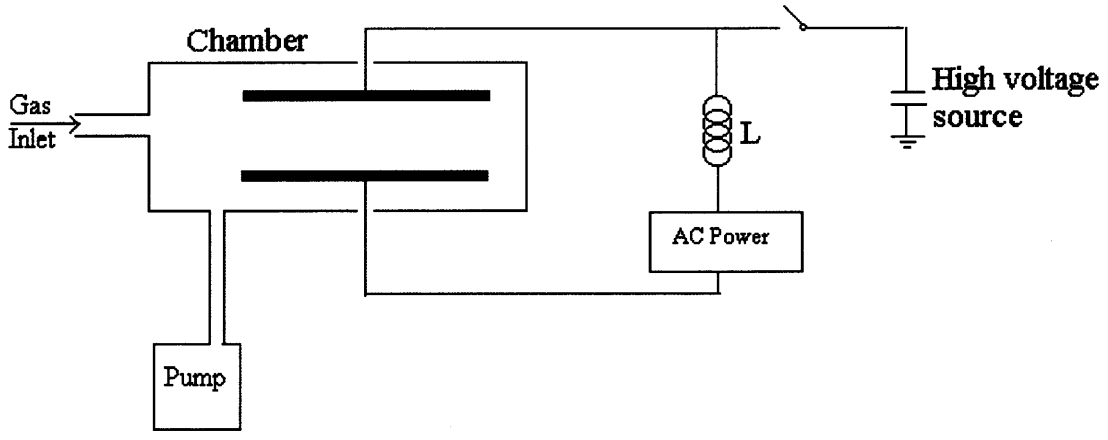

Figure 2.2 Schematic Figure of Tegal-100 system.

One of plasma equipment that we used is Tegal-100 system, as shown in Fig. 2.2. In this system, the electrode area is about $0.01m^2$; the maximum RF power is 300~400 W; and the typical ion density is 10^{16}~10^{18} atoms/m^3.

2.3.2 Model for Tegal-100 system

In Tegal-100 system, we suppose

$$I \approx I_i = eAu_B n_p \tag{2-9}$$

where A is the area of electrode, u_B is Bohr velocity, n_p is the density of ions.

Considering that there are two sheaths in the plasma area and two electrode areas are same, then

$$P = 2VI = 2eAu_B n_p V(x) \tag{2-10}$$

where P is the total power that is consumed in the plasma, V is the potential drop across the sheath.

From the equation (2-10)

$$n_p = P / 2eAu_B V(x) \tag{2-11}$$

From Poison equation (2-3)

$$\frac{\partial^2 V(x)}{\partial x^2} = -\frac{P}{2\varepsilon Au_B V(x)} \tag{2-12}$$

The boundary conditions for equation (2-12) are

X=0, V(x)=V

X=s, V(x)=0

Then

$$V^2 = \frac{P}{\varepsilon Au_B} s \tag{2-13}$$

where s is sheath distance.

2.3.3 Simulation Results

In Tegal-100 system, the main ion species are H_2^+ and H_3^+.

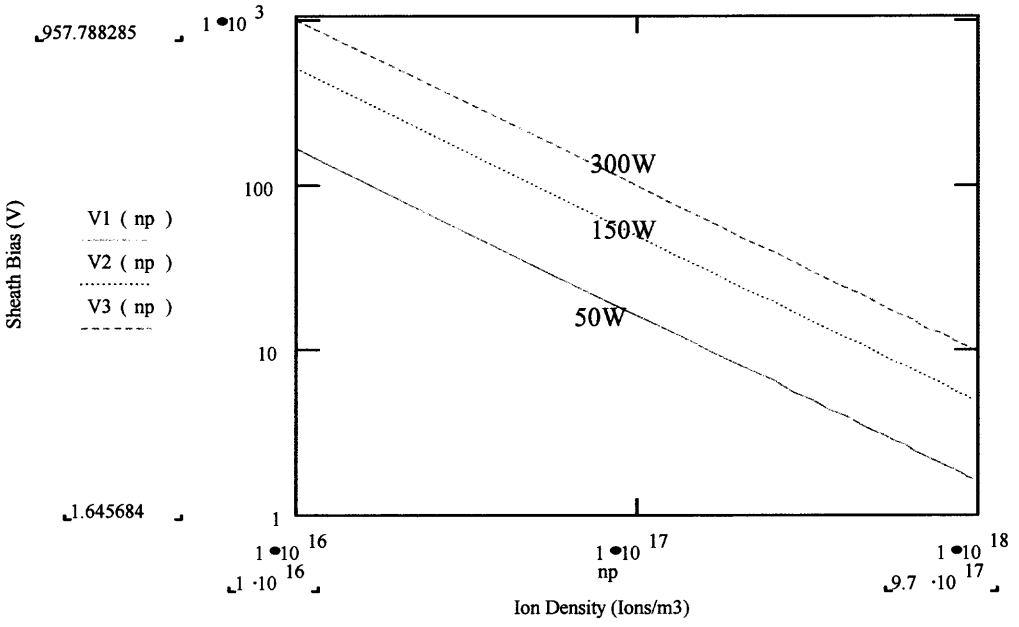

Figure 2.3 Simulating sheath bias as a function of ion density in Tegal-100 system.

From Fig. 2.3, we can find the sheath bias range is from 0~1000 V in Tegal-100 if the maximum power is 300 W. The sheath potential will increase as the power increase, and decrease as ions concentration increase.

2.4 Sheath Model and Simulation for DC plasma and Low Pressure Plasma Ion Immersion Implantation

In order to solve equation (2-1)~(2-3), we will simplify our models. There are two simple models in the following calculations.

2.4.1 Model Simplifying

2.4.1.1 Matrix Sheath

Sheath Voltages are often driven to be very large compared to Te. The potential ϕ in these sheaths is highly negative with respect to the plasma-sheath edge; hence $n_e \sim 0$ and only ions are present in the sheath. The simplest high-voltage sheath, with a uniform ion density, is known as a matrix sheath. In the matrix sheath, $\partial n_i / \partial t = 0$ and $\partial u_i / \partial t = 0$. Letting ni=ns=const within the sheath of thickness s and choosing x=0 at the plasma-sheath edge, then equation (2-1)~(2-3) can be written as

$$\frac{\partial (u_i n_i)}{\partial x} = 0 \qquad (2\text{-}1a)$$

$$u_i \frac{\partial u_i}{\partial x} = -\frac{e}{m}\frac{\partial V}{\partial x} \qquad (2\text{-}2a)$$

$$\frac{\partial^2 V}{\partial x^2} = -e\frac{n_s}{\varepsilon} \qquad (2\text{-}3a)$$

from equation (2-3a)

$$\frac{dE}{dx} = \frac{en_s}{\varepsilon_0} \qquad (2\text{-}14)$$

which yields a linear variation of E with x:

$$E = \frac{en_s}{\varepsilon_0} x \tag{2-15}$$

Setting $V=-V_0$ at $x=s$, we obtain the matrix sheath thickness

$$s = \left(\frac{2\varepsilon_0 V_0}{en_s} \right)^{1/2} \tag{2-16}$$

In terms of the electron Debye length $\lambda_{De} = (\varepsilon_0 T_e / en_s)^{1/2}$ at the sheath edge, we see that

$$s = \lambda_{De} \left(\frac{2V_0}{T_e} \right)^{1/2} \tag{2-17}$$

Hence the sheath thickness can be tens of Debye lengths.

2.4.1.2 Child Law Sheath [44]

In the steady state, the matrix sheath is not self-consistent since it does not account for the decrease in ion density as the ions accelerate across the sheath. In the limit that the initial ion energy is small compared to the potential, the ion energy and flux conservation are

$$\frac{\partial (u_i n_i)}{\partial x} = 0 \tag{2-1b}$$

$$u_i \frac{\partial u_i}{\partial x} = -\frac{e}{m} \frac{\partial V}{\partial x} \tag{2-2b}$$

$$\frac{\partial^2 V}{\partial x^2} = -e \frac{n_i}{\varepsilon} \tag{2-3b}$$

from (2-2b)

$$\tfrac{1}{2}Mu^2(x) = -e\phi(x) \tag{2-18}$$

$$en(x)u(x) = J_0 \tag{2-19}$$

where J_0 is the constant ion current. Solving for n(x), we obtain

$$n(x) = \frac{J_0}{e}(-\frac{2e\phi}{M})^{-1/2} \tag{2-20}$$

Using this in Poisson's equations (2-3b), we have

$$\frac{d^2\phi}{dx^2} = -\frac{J_0}{\varepsilon_0}\left(-\frac{2e\phi}{M}\right)^{-1/2} \tag{2-21}$$

Letting ϕ=-V_0 at x=s and solving for J_0, we obtain

$$J_0 = \frac{4}{9}\varepsilon_0\left(\frac{2e}{M}\right)^{1/2}\frac{V_0^{3/2}}{s^2} \tag{2-22}$$

Equation (2-22) is the well known Child law of space-charge-limited current in a plane diode. With fixed spacing s, it gives the current between two electrodes as a function of the potential difference between them and has been traditionally used for electron diodes. However, with J_0 given explicitly as

$$J_0 = en_s\mu_B \tag{2-23}$$

In (2-22), we have a relation between the sheath potential, the sheath thickness and the plasma parameters, which can be used to determine the sheath thickness s. Substituting (2-23) in (2-22) and introducing electron Debye length at the sheath edge, we obtain

$$s = \frac{\sqrt{2}}{3}\lambda_{De}\left(\frac{2V_0}{T_e}\right)^{3/4} \tag{2-24}$$

Comparing this to the matrix sheath width, we see that the Child law sheath is larger by a factor order $(V_0/T_e)^{1/4}$. Hence the child law sheath can be of order 100 Debye length (~1cm) in a typical processing discharge. Since there are no electrons within the sheath to excite the gas, the sheath region appears dark when observed visually.

The potential with the sheath as a function of position

$$\phi = -V_0\left(\frac{x}{s}\right)^{4/3} \tag{2-25}$$

The electric field E is

$$E = -\frac{d\phi}{dx} = -\frac{4}{3}\frac{V_0}{s}\left(\frac{x}{s}\right)^{1/3} \tag{2-26}$$

and the ion density is

$$n = \frac{\varepsilon_0}{e}\frac{dE}{dx} = \frac{4}{9}\frac{\varepsilon_0}{e}\frac{V_0}{s^2}\left(\frac{x}{s}\right)^{-2/3} \tag{2-27}$$

The Child law solution is valid if the sheath potentials are large compared to the electron temperature. It is therefore not appropriate for use where the sheath potential is the potential between a plasma and a floating electrode. Because the ion motion was assumed collisionless, it is also not appropriate for higher pressure discharges.

2.4.2 Equipment Description [45]

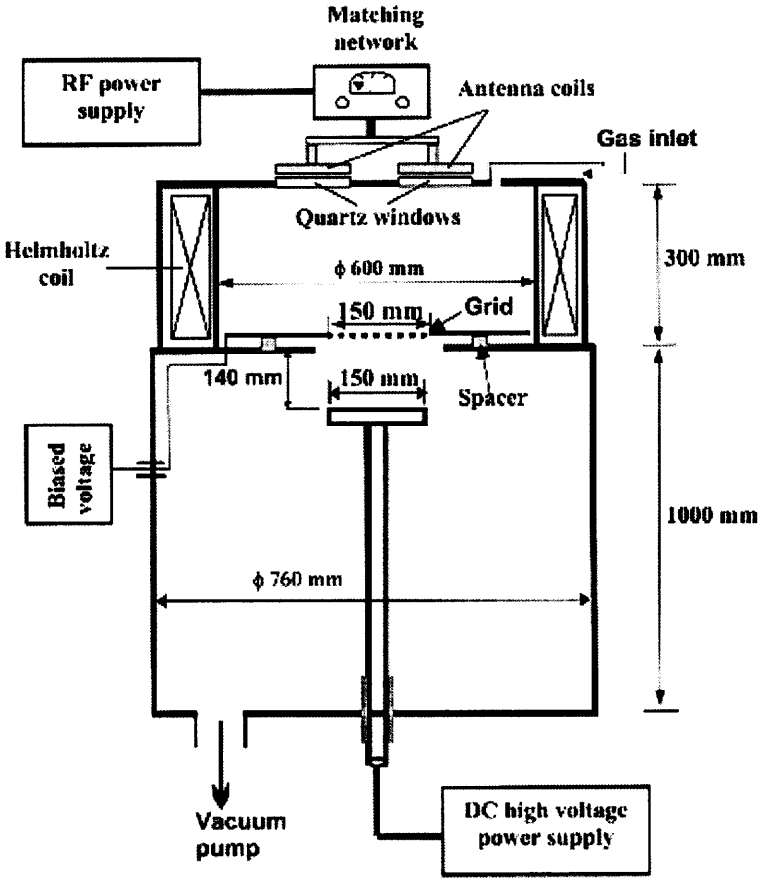

Figure2.4 Schematic diagram of the rf-ICP direct current plasma implantation hardware.

The schematic diagram of the rf-ICP dc-PIII hardware is depicted in Fig.2.4. It consists of two cylindrical vacuum chambers made of stainless steel with different inner diameters separated by a conducting grid. The upper part acts as the plasma source whereas the bottom part is the processing chamber containing the wafer chuck. Four planar circular antenna coils are placed outside the plasma source chamber on top of the four quartz

windows. There are also magnetic coils outside the plasma source chamber to confine the plasma and adjust the plasma density uniformity radically. The conducting grid is placed on insulating spacers, and so the size (height) of the plasma source can be easily adjusted by changing the spacers. The grid is made of stainless steel with 5 mm diameter holes in a circular area 150 mm in diameter. The outer rim of the grid is solid and does not have holes.

2.4.3 Simulation Description

An important parameter is the threshold voltage V_{DC} in the dc PIII mode. If the applied voltage V_0 goes beyond V_{dc}, the dc (or static) sheath edge will hit the chamber wall or the plasma source and the plasma will extinguish. Taking a slab geometry, the collisionless sheath thickness can be calculated by Child's law.

To limit the sheath in the chamber of which the length is L

$$V_0 \le V_{DC} = \left[\frac{9}{4\varepsilon_0} \left(\frac{eM}{2} \right)^{1/2} n_0 u_b L^2 \right]^{2/3} \qquad (2\text{-}28)$$

H_2^+ is the dominant ion density for different chamber length. The electron temperature Te is set to 3 eV. V_{DC} is the maximum voltage at which the PIII system can be operated in a stable condition [46].

In the pulsed PIII mode, if the voltage V_0 applied to the sample stage is less than the dc threshold voltage V_{DC}, the sheath will never hit the chamber wall regardless of the

pulse duration. Even though the pulse voltage is higher than V_{DC}, the plasma may not extinguish if the pulse is turn off before the sheath edge dynamically propagates to the chamber wall where the RF source is. Thus, there are two interrelated parameters, the threshold pulse voltage Vpl and the threshold pulse duration Tpl. Every PIII system with a certain chamber size and plasma properties has its Tpl-Vpl characteristic curve in the operational phase space. If a working point is above that curve, the plasma cannot be sustained and implantation will be prematurely terminated as the plasma goes off.

When a pulsed voltage V_0 is applied to the sample stage, electrons are expelled from the region adjacent to the sample stage and leave the ion-matrix sheath in a very short time on the order of the inverse electron plasma frequency ω_{pe}. In a low plasma density (10^8-10^{10} ions/cm3) condition, this time scale is around 10^{-8}-10^{-9} s. Next, the sheath edge expands as ions are accelerated toward the sample stage. To derive the dynamic sheath propagation equation, several assumptions are made here. The sheath is collisionless since the selected implantation pressure is around 0.4 mTorr. The time to form the Child's law sheath is much shorter than that for the sheath to make an observable movement. Therefore, we can use quasi-static Child's law to describe the sheath propagation

$$s = \sqrt{\frac{4}{9}\varepsilon_0\left(\frac{2e}{M}\right)^{1/2}\frac{V_0^{3/2}}{J}}$$

$$J = en_s(u_b + \frac{ds}{dt}) \qquad (2\text{-}29)$$

where the sheath thickness s, ion current density J, and plasma density n are functions of time t.

To solve (2-29), we need the initial condition and plasma density distribution n(x,t). Using the model in Fig. 2.1, the plasma enters from the up side with a constant flux Γ0 and a negative voltage is applied to the lower side. Assuming that there is no ion creation in the space, the plasma density distribution n(x,t) satisfies the diffusion equation at all time

$$\frac{dn(x,t)}{dt} - D\frac{d^2n(x,t)}{dx^2} = 0 \qquad (2\text{-}30)$$

where D is the ambipolar diffusion coefficient. The initial plasma density n(x,0) can be solved without time dependence

$$-D\frac{d^2n(x,0)}{dx^2} = 0 \qquad (2\text{-}31)$$

The solution is a linear decay across the plasma region

$$n(x,0) = \frac{\Gamma_0}{D}(L-x) + B \qquad (2\text{-}32)$$

To determine the coefficient B, we must investigate the boundary condition. Before the voltage is applied, there is a very thin sheath around the right wall. This initial sheath thickness is several Debye lengths and can be omitted in our calculation. The ion flux lost to the right wall must be

$$\Gamma = n_s u_b \qquad (2\text{-}33)$$

In a steady state, Γ must be Equal to Γ_0. Thus, ns is assigned to be the plasma

density at the right side n(L,0) since the initial sheath thickness is neglected. The initial plasma density across the region is

$$n(x,0) = \frac{\Gamma_0}{D}(L-x) + \frac{\Gamma_0}{u_b} \tag{2-34}$$

We assume that an abrupt negative voltage $-V_0$ is applied to the right wall and the matrix sheath is formed in a very short time before the ions go into motion. Hence, the ion distribution still satisfies (2-34). The matrix sheath thickness s_0 can be calculated by solving Poisson's equation

$$\frac{d^2\phi}{dx^2} = -\frac{e}{\varepsilon_0} n_i \tag{2-35}$$

Substitution (2-34) into the right-hand side of (2-35), we obtain

$$\phi = -\frac{e}{\varepsilon_0}\left[\frac{1}{6}\frac{\Gamma_0}{D}x^3 + \frac{1}{2}\frac{\Gamma_0}{u_b}x^2\right] \tag{2-36}$$

Setting ϕ=-V_0, the ion matrix sheath thickness satisfies the following

$$V_0 = \frac{e}{\varepsilon_0}\left[\frac{1}{6}\frac{\Gamma_0}{D}s_0^3 + \frac{1}{2}\frac{\Gamma_0}{u_b}s^2\right] \tag{2-37}$$

By applying the initial and boundary conditions, the sheath propagation and ion current can be solved from the dynamic sheath equation (2-29) and diffusion equation (2-30). Adopting the criterion that the sheath edge propagates to the left side, we can derive the T_{pl}-V_{pl} characteristic curves.

2.4.3 Simulation Results

The equations can be solved numerically by the finite difference method assuming H^2_+ to be the dominant ion species in the plasma. The electron temperature is assumed to be 3 eV. Fig.2.5 illustrates the threshold voltage versus hydrogen density for different chamber length. Vdc is the maximum voltage at which the PIII system can be operated in a stable condition.

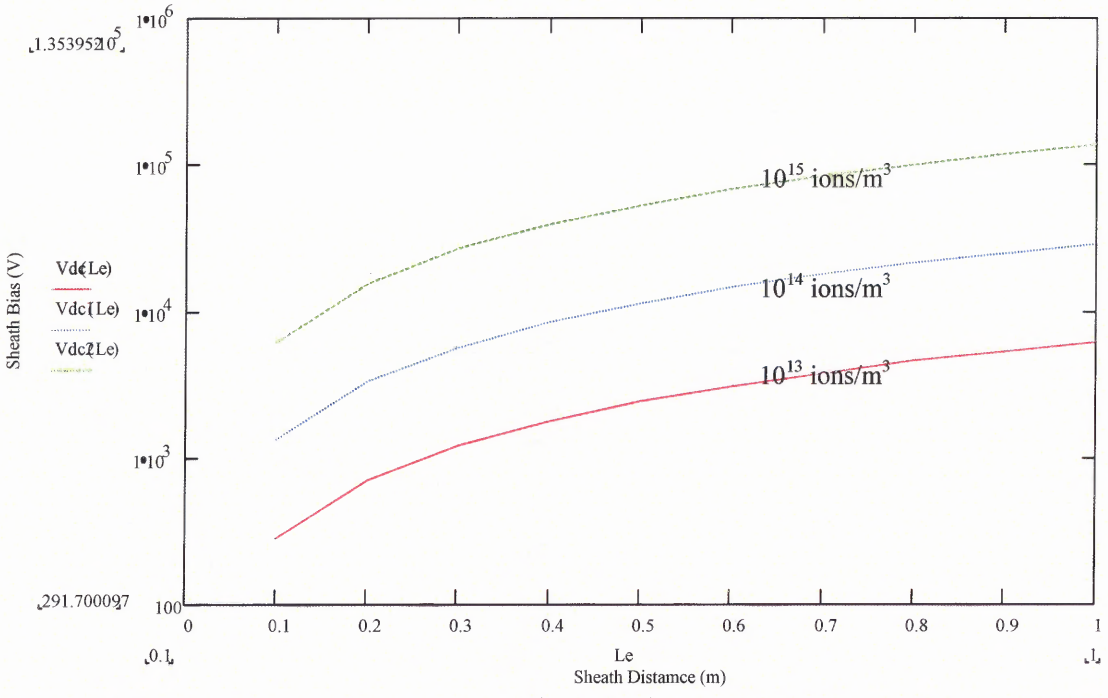

Figure 2.5 DC threshold voltage versus H_2^+ and H_3^+ plasma density for different chamber size.

The relationship of the threshold pulse Tpl versus the threshold voltage Vpl is systematically studied for plasma diffusion coefficient D, ion flux Γ_0, and chamber size L. In a fast diffusion system, the plasma sheath expands rapidly and the time needed to

reach equilibrium is short. Fig. 2.6 displays Vpl and Tpl for different ion flux Γ_0. The diffusion coefficient D=100 m^2/s and the chamber size is 1 m in this derivation. It is obvious that an efficient plasma source capable of a high plasma creation rate is beneficial to long pulse PIII.

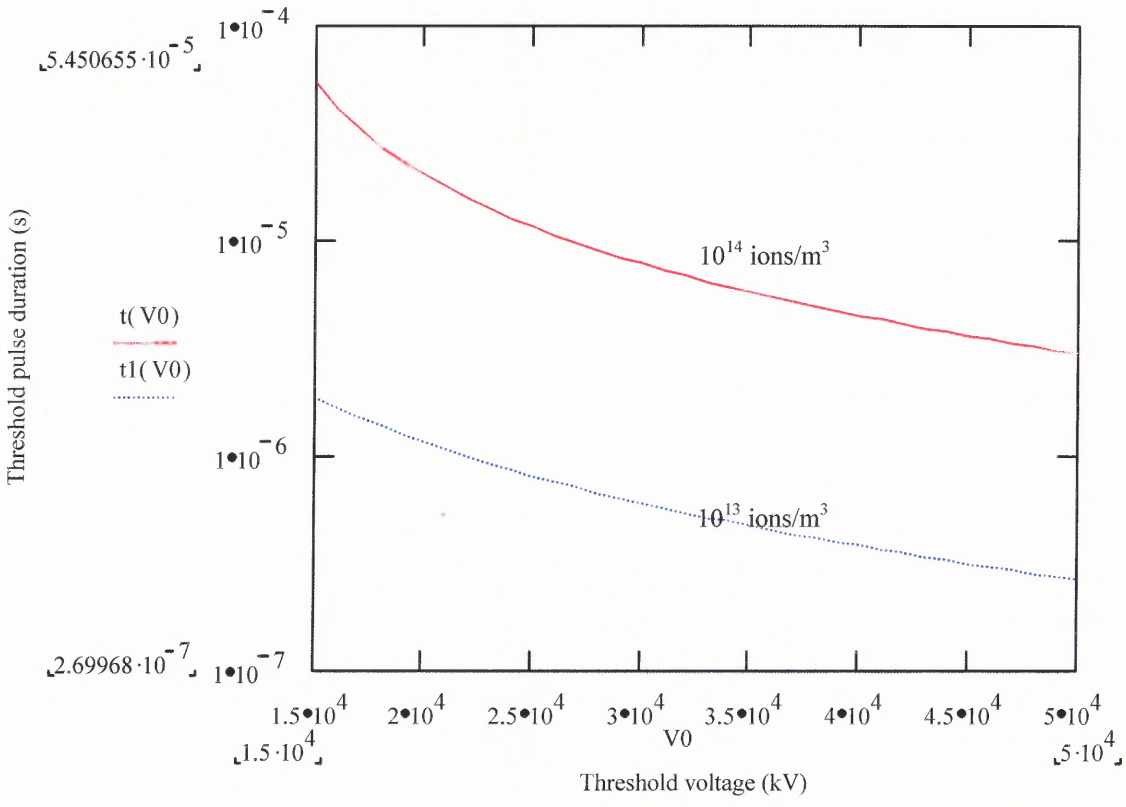

Figure 2.6 Threshold pulse duration versus threshold voltage for different ion fluxes in pulsed PIII.

2.5 Summary and Conclusions

Ionized hydrogen gas can be characterized as plasmas if they meet three criteria

1. The system dimensions must considerably exceed sheath distance. Only in this way can the quasineutrality of the bulk of the plasma be ensured.

2. The total number (N_D) of shielding electrons drawn into the Debye sphere must be large; at very least N_D should be greater than unity.

3. Electrons should interact more strongly with each other than with the neutral gas. Under these conditions, particle motion in the plasma will be controlled by electromagnetic forces rather than by gas fluid dynamics.

In our Tegal-100 plasma system, we can find the sheath bias range is from 0~1000 V if the maximum power is 300 W. The sheath potential will increase as the power increase, and decrease as ions concentration increase.

In the pulsed PIII mode, if the voltage V_0 applied to the sample stage is less than the dc threshold voltage V_{DC}, the sheath will never hit the chamber wall regardless of the pulse duration. Even though the pulse voltage is higher than V_{DC}, the plasma may not extinguish if the pulse is turn off before the sheath edge dynamically propagates to the chamber wall where the RF source is. Thus, there are two interrelated parameters, the threshold pulse voltage Vpl and the threshold pulse duration Tpl. Every PIII system with a certain chamber size and plasma properties has its Tpl-Vpl characteristic curve in the operational phase space. If a working point is above that curve, the plasma cannot be sustained and implantation will be prematurely terminated as the plasma goes off. It is obvious that an efficient plasma source capable of a high plasma creation rate is

beneficial to long pulse PIII. In our PIII system, the chamber distance is ~1m, so the maximum voltage is ~30 KV, the effective pulse duration is ~0.0001s.

CHAPTER 3

CHARACTERIZATION EXPERIMENTS

3.1 IR measurement

Figure 3.1 Nicolet 60 SX FTIR in Prof. Chabal's lab.

The infrared data were obtained using a Nicolet 60 SX FTIR spectrometer equipped with a broadband MCT detector and operating at 4 cm^{-1} resolution in a transmission reflection geometry. All spectra were collected under ambient conditions and referenced to an identical un-hydrogenated sample. Additional baseline subtraction was usually required to remove oscillations that result from interference between beams reflected from the implanted region (after partial separation/crack development) and the sample surface. In each case, this subtraction was performed using the same high order polynomial function

that was fit to the entire broadband spectrum (400-4000 cm^{-1}) to minimize the preferential selection of spectral features.

3.2 Scanning Electron Microscopy

The scanning electron microscope (SEM) scans a focused electron beam across the sample surface. Scintillator-photomultiplier detectors collect backscattered electrons and/or electrons emitted from the sample. The output from the sample. The output from the detectors is scanned synchronously with the scan of the electron beam on the sample, producing two dimensional images of the sample surface. The magnification of the SEM image equals the ratio between the distance on the sample surface scanned by the electron beam and the portrayed distance on the SEM image. Fig3.2 shows schematic the setup of a SEM. In the SEM used for this work, the electron beam is produced by a field emission gun. An electronmagnetic condenser lens system reduces the electron beam to a highly focused electron probe. The upper and lower deflection coil deflects the electron beam in a manner that the beam scans the whole specimen surface to be imaged. An aperture is placed in the electron optical column to decrease the divergence angle of the electron beam. The base pressure in the sample chamber is 10^{-6} mbar.

The secondary electrons with energy <50 eV are collected to provide topographic information, whereas backscattered electrons have far higher energies and are used to gather atomic number or orientation information.

For topographic measurements, only secondary electrons are collected. To ensure efficient accumulation of secondary electrons a positive biased grid is placed in front of the secondary electron detector, a scintillator-photomultipiler. The contrast arises from

changes in surface topography: when the surface is locally nearly parallel with the electron beam a large number of incident will be elastically scattered, generating a high secondary electron signal. Because the parts of the sample surface, which have the most direct path to the detector, appear brightest, the image of a rough specimen appears as if it is viewed from above.

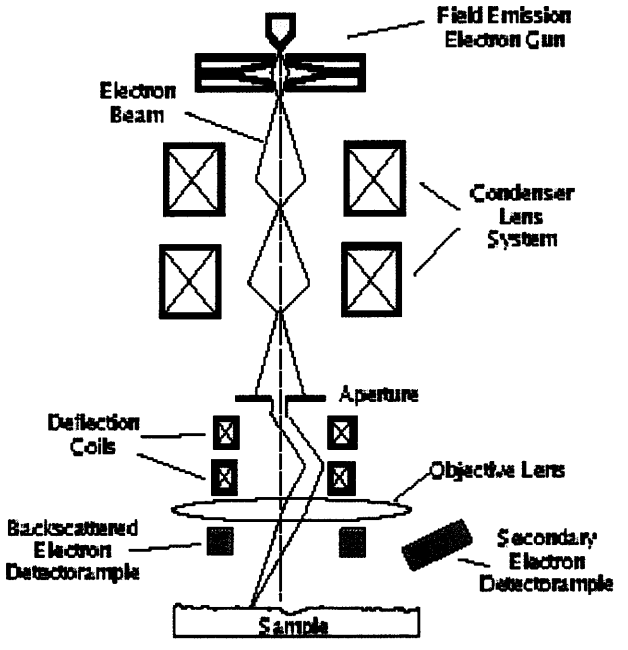

Figure 3.2 Setup of a scanning electron microscope.

The strength of the SEM in the topographical mode lies in the very large depth of field, i.e. the distance D the sample surface can be displaced from the point of focus without the sample surface going out of electron optical focus (Fig 3.3). The convergence angle α of the electron probe determines the depth of field of a SEM. Thus, the large depth of field D, which is commonly associated with SEM images, is due to the convergence angle α at the specimen, which is much smaller than the corresponding

angles in optical microscopes [47].

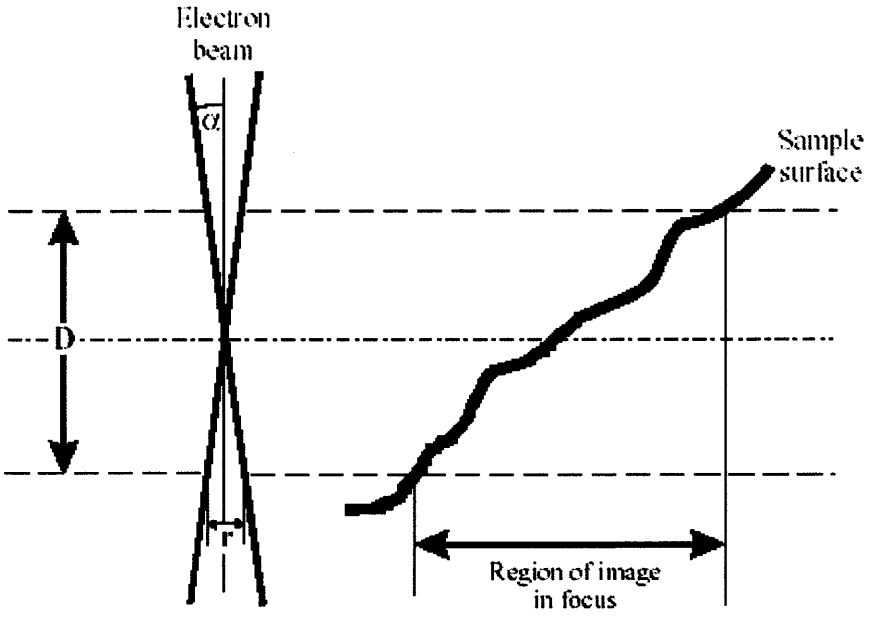

Figure 3.3 Schematic illustration of the depth of field D.

To a first approximation, the vertical distance D/2 required to broaden the electron beam of a minimum radius to a radius r is

$$D/2 \cong r/\alpha$$

The electron beam divergence α depends on the aperture radius R and the working distance WD, i.e. the distance between the bottom pole piece of the objective lens and the sample surface (α=R/WD). For the SEM imaging in this work, an aperture with a radius of 25 μm was chosen and the working distance was kept at ~9 mm for all measurement. We set r=5nm. Hence, the depth of field is calculated to be:

$$D=2r/(R/WD)=2*0.005/(25/9000)=3.6\ \mu m$$

3.3 Atomic Force Microscope

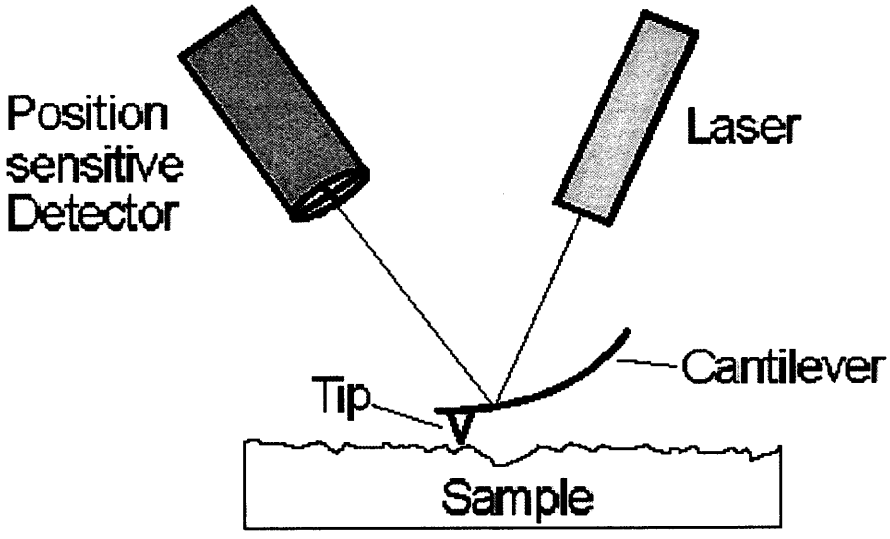

Figure 3.4 Schematic illustration of the AFM measurement setup.

The atomic force microscope (AFM) offers the possibility to obtain the surface topography quantitatively under atmospheric conditions. In this work, atomic force microscopy was applied to measure the thickness of exfoliated layers after ion-cutting and the depths of hydrogenation induced surface blisters. Furthermore, three dimensional surface topography of the silicon samples was obtained to gain information of the roughness of surfaces created by the ion-cut.

The functionality of the AFM is based on the interaction of a very thin tip (radius<25 nm) with the potential of the sample surface. The setup of AFM is presented in Fig 3.4. The tip is mounted on a cantilevel spring and scans the sample surface. The electron cloud of the tip pushes against the clouds of individual atoms in the sample, generating a repulsive force that varies with the surface topography. The force deflects

the tip. These tip movements are monitored by a laser beam deflected from the top of the cantilever to a position sensitive photo detector.

3.4 Transmission Electron Microscope [48,99]

Transmission electron microscope is used to obtain information from samples, which are thin enough to transmit electrons. Because of excellent resolution (~0.2 nm), the TEM provides access to the microstructure down to molecular dimensions. Fig.3.5 shows a schematic setup of a TEM. A beam of highly focused electrons is directed towards a thinned sample. The transmitted electrons penetrate an objective lens and subsequent imaging lenses before they hit the photo plate. An objective aperture is inserted in the back focal planes of the objective lens. This aperture is used to select the electron beam area from which to form the image. A variety of different signals can be used for image formation, among these transmitted and diffracted electrons as well as characteristic X-rays, allowing for a unique information combination concerning shape, distribution, crystallography and chemistry of microstructural detail.

Depending on the positioning of the aperture slits the TEM imagining is divided in two categories. In the bright-field image the aperture blocks the diffracted electron beam and only the incident beam is let through on the photo plate. On the contrary, when the incident beam is deflected so that only the diffracted electrons hit the photo plate. In both cases a purely amplitude contrast image is obtained. A major advantage of microstructure analysis by TEM compared to microstructure analysis by X-ray diffraction is the ability to analyze very small crystal areas down to a diameter of 50-200 nm. The strong interaction of electrons with the nuclei increases the intensity of the reflections.

In this work, TEM was carried out only in the cross-section mode. Bright field images were obtained to determine the depth of the implantation zone and to gain detailed information about the crystal defects within the implantation zone. Electron

diffraction patterns were obtained to gain knowledge about the crystalline quality of the silicon within the implantation zone and also in the surface near region above the implantation zone.

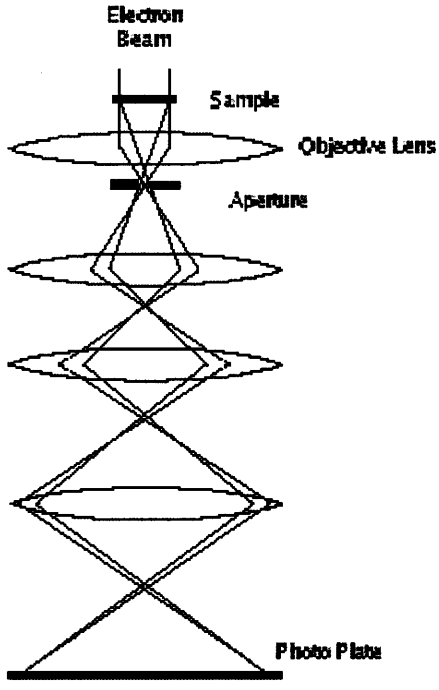

Figure 3.5 Setup of a transmission electron microscope.

The penetration depth of the electrons in the sample is limited and therefore only very thin samples can be analyzed. Hence a requirement for TEM analysis is the thinning of the sample to a thickness of only about 50-100nm. Fig.3.6 shows schematically the steps of the sample preparation for TEM analysis.

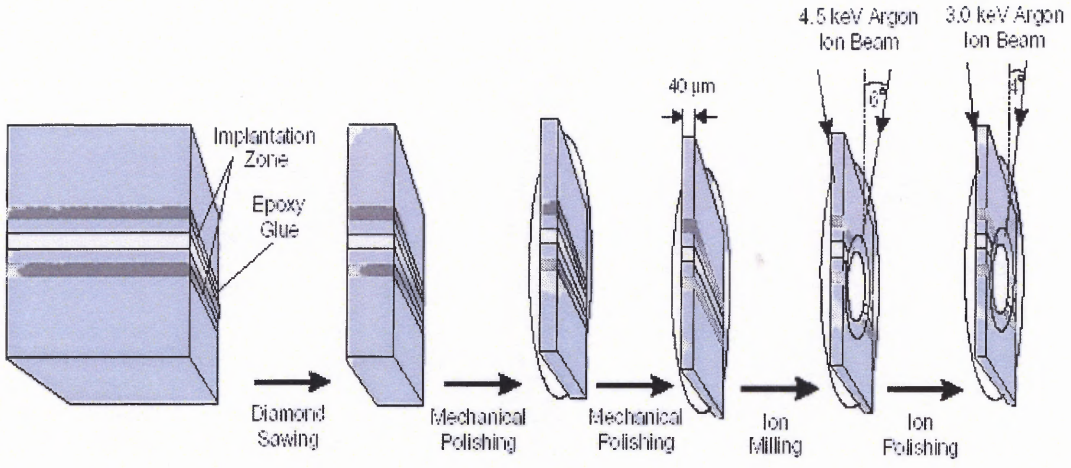

Figure 3.6 Sample preparation process for TEM.

First, the silicon sample is cut in half and the two pieces are glued together with an epoxy glue. Then, a little piece is cut out with a diamond saw and subsequently mechanically polished on one side. Then, the TEM sample is glued to a washer with the polished side facing the washer and is thinned mechanically to a thickness of about 40 µm by polishing the other side of the TEM sample. Afterwards, the sample is placed in an ion-miller on a rotation stage and bombarded with a 4.5 keV argon beam on both sides. The angle between the upper and lower sample surface and the two ion beams are 6°. The argon bombardment creates a crater in the TEM sample, whose edge runs across the cross-section of the sample. In the vicinity of this crater the sample is thin enough for high energetic electrons to penetrate and consequently makes TEM analysis possible. Finally, the TEM sample is further polished within a 3 keV argon ion beam impinging on the TEM sample surface at a glancing angle of 4°.

CHAPTER 4

TRAPPING LAYER FORMED BY DIFFERENT IMPLANTATIONS

Ion implantation is one of the most important processing tools in Si integrated circuit technology. It was discovered by Ohl at Bell Laboratories in 1952. Today, ion beams are ubiquitous in Si technology (see Fig. 4.1). Driven to a very large extent by requirements of the semiconductor industry, there has been an enormous research effort into a broad range of ion beam modification processes in semiconductors over the past 3 decades[49].

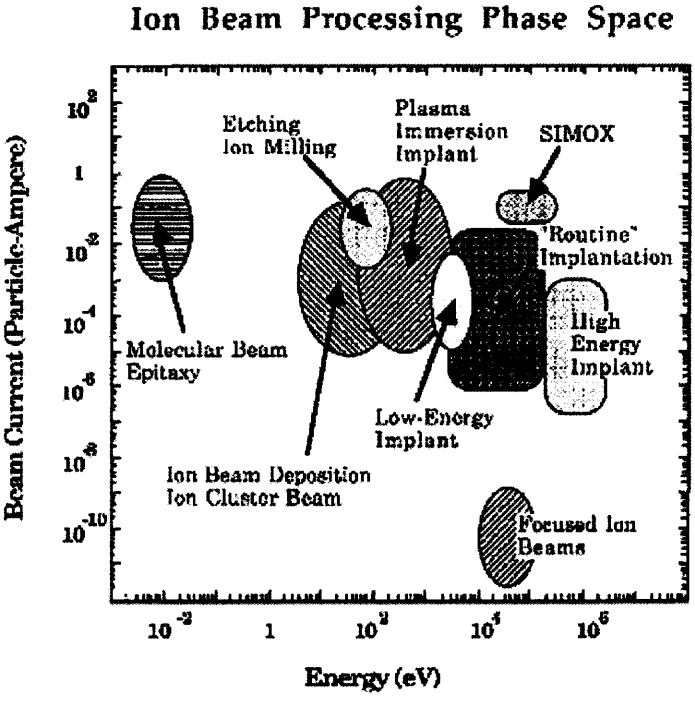

Figure 4.1 Schematic phase space map of the range of ion energies and beam currents used in semiconductor processing.

In this chapter, silicon wafers are implanted by different elements (He, N, Ne, Ar) at appropriate energy. A H trapping layer will be formed in the depth of ~100 nm from

TRIM calculation. Why we choose these implantations, the reason is that two different types of trapping layer are formed, one is vacancy cluster, and the other is gas bubble.

4.1 The mechanism of damage accumulation and its removal in implantation [50-55]

When an energetic ion enters a solid it loses energy by two processes: (i) by elastic or nuclear collisions with the matrix atoms causing direct atom displacements and disorder; and (ii) by inelastic or electronic processes in which the electrons of the solid are excited. In semiconductors, only elastic collisions usually generate lattice damage, whereas in insulators, both processes can induce atomic displacements. The collisional or direct displacement processes that occur during the collision cascade take place on a time scale of 10^{-11} s. After such a time the cascade is said to be quenched and, if the discrete defects resulting are immobile and stable, such disorder will not be quenched in. However, if defects such as vacancies and interstitials are mobile at the implantation temperature, then significant dynamic annealing and annihilation of damage can occur during implantation. Indeed, although discrete point defects in silicon are mobile at room temperature, if the density of defects in the cascade is high then discrete defects appear to be efficiently trapped within damage and implantation damage is mostly stable. In such cases, as the dose is increased and the damage from individual tracks overlap, amorphisation can occur. If no annealing of damage occurs during implantation, then amorphisation, or complete disruption of lattice order, should occur at a dose at which each atom has been displaced approximately once. On the other hand, if significant dynamic annealing occurs, amorphisation can be suppressed and the resultant disorder can build up as a dense array of extended defects, particular dislocation tangles. When

dynamic annealing is dominant, the nature of resultant damage can depend strongly on the implantation temperature (which controls the annealing rates) and dose rate (which controls the rate at which damage is introduced).

4.2 N^+ implantation

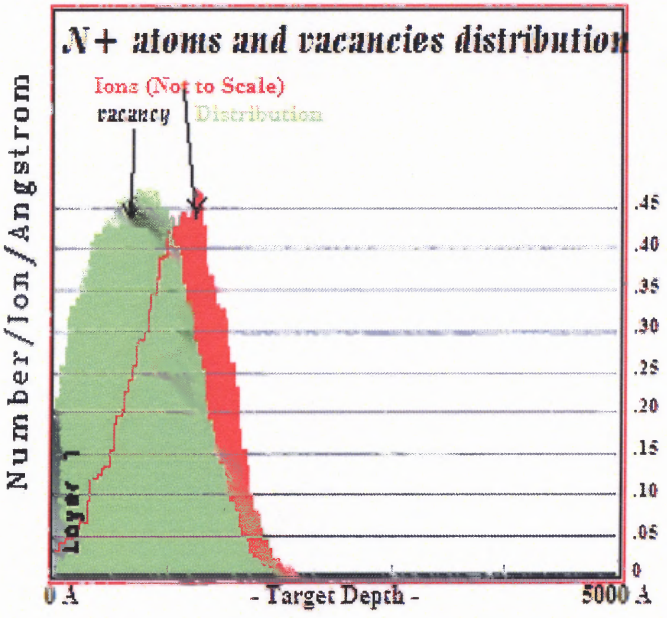

Figure 4.2 Trim simulation result of N^+ implanted in Si at 40 keV.

It was previously demonstrated [56,57,58] that implantation of c-Si with Si^+, N^+, O^+ at elevated temperatures leads to formation of two distinct layers: a dislocation free near-surface layer, which presents mechanical strain of contraction, and a highly dislocated layer located around the region of the end of range of the ions. This double layer structure appear to be formed due to a spatial separation of point defects formed from the Frenkel pairs in collision cascades. The spatial separation of vacancies and self-interstitials results

from the nonzero momentum component of the recoiled Si atoms in the beam incidence direction. As a consequence, in the near surface regions, the vacancy concentration exceeds that of the self-interstitials, while in regions comprising the end of range of the ions, the imbalance in the point defect concentrations reverses. Considering that the dynamic annealing consumes equal concentrations of vacancy and self-interstitials, in the near surface region, vacancy related defects (vacancy clusters) are created, while in the regions comprising the end of range of the ions, the created defects are interstitial related ones (extrinsic type dislocation loops, stacking faults, clusters of interstitial Si atoms, etc). The build up of vacancy clusters distribution in the near-surface layer is responsible for the development of the negative strain (of contraction). On the other hand, the surplus self-interstitial atoms in regions around the end of range of the ions promote the formation of a highly dislocated layer.

After N^+ implantation at 40 keV, two distinct layer are formed in the silicon wafer. From TRIM calculation result in Fig. 4.2, a vacancy rich layer in the near surface region (0~100nm) which shows mechanical strain of contraction (negative strain). From 100nm~200nm, this layer represents positive strain because of extra-interstitial and dislocations.

4.3 He^+ implantation

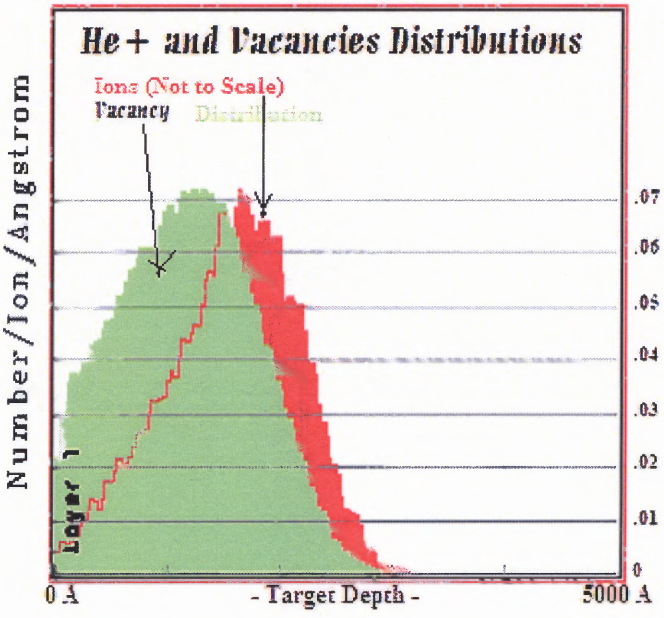

Figure 4.3 Trim simulation result of He^+ implanted in Si at 15 keV.

Noble gas atoms have negligible solid solubility in c-Si. They can be incorporated in silicon as a result of ion beam related processes. In this chapter, we choose He implantation. It is experimentally observed that helium implantation produces a slight excess of self-interstitials, which more over disappear after heating at moderate temperature. The interaction of the isolated vacancy with the interstitial helium has been studied via ab initio molecular dynamics; this study has demonstrated that a helium atom which originally put in a vacancy escapes and that nearest-neighbor sites do not host helium too.[59]

The tensile displacement field surrounding vacancy clusters is expected to attract helium atoms that will eventually form a kind of 'helium atmosphere' [60]. Since the

silicon crystal surrounding a vacancy cluster is manifestly softer than the unperturbed crystal, the arrangement of helium in that region will interfere with the pre-existing displacement field. Since the displacement field is tensile, it is manifestly cheaper to arrange a helium atom in a vacancy-cluster atmosphere.

After silicon wafer is implanted with He at 15 keV, only a positive strain is observed. In the case of He+ implantation, the ballistic mechanisms which produce an excess concentration of vacancy near the sample surface also take place. However, the implanted He^+ atoms diffuse into vacancy rich layer and agglomerate to create bubbles. Finally, only bubbles layer can be formed near 100nm (shown in Fig. 4.4) at 15 keV implantation.

4.4 Ne^+ and Ar^+ implantation

Ar or Ne is the member of the noble gases that has received the greatest attention in the past, since they are cheap and also most widely used noble gas. Compared with He implantation, Ar or Ne atom is bigger and heavier. The implantation of Ar+ ions into Si is known to result in more lattice disorder and argon is particularly hard to out diffuse up to nearly 600 °C [61].

In our research, Ar or Ne implantation is used to generate defects rich layer in the crystalline Si, but it is very easy for Ar implantation to make absolutely amorphization from the wafer surface to the project range [62,63]. How to get buried disorder layer and keep the surface layer as crystalline structure is important.

High beam current is known to give in situ annealing during implantation. The Grob's research[32] show that if silicon wafers were thermally insulated and the beam

current was maintained high enough (about $1\mu A/cm^2$) to exceed an implantation temperature of 200 °C and the amorphization can avoided. Cullis' work[32,61] shows that when Si samples were implanted with Ar^+ (a dose of 2×10^{15} Ar+/cm^2 at 4μA beam current), the layer from the surface to project range are 100% disorder, while a buried layer of disorder can be formed when the silicon samples were implanted with a dose of 2×10^{15} Ar^+/cm^2 at 30μA beam current.

In this paper, high beam current (~$3mA/cm^2$) is used to implant Ar+ into Si samples with a dose ranging from 10^{15} to 4×10^{15} Ar+/cm^2, finding the appropriate substrate temperature that form the buried amorphous layer. After forming the buried amorphous layer, the wafers are annealed at about 600 °C for a certain time. The epitaxial growth can occur in the both sides of the buried disorder layer. The whole process and the TEM picture of this structure are shown in Fig.4.5 and Fig.4.6. From Fig.4.5, we can find a sandwich-like structure in our sample, which is the thin crystal structure near the surface (layer A), disorder layer underneath (layer B), then crystal bulk (layer C). Fig. 4.5(B) show us that twin crystal, amorphous and crystal co-exist in layer B. At the same time, we can find some bubbles in this buried disorder layer. We think that the presence of the Ar bubbles acts as a sink for the vacancies.

From the Fig.4.6, we can find a long bright line along the interface of crystal and amorphous region. We suppose that this bright line is made from congregation of bubbles. Through these presences of the bubbles, the amorphous and the crystalline phases are decoupled. Silicon atoms on the boundary of the bubble which faces the amorphous silicon region lose contact with the single crystal at the opposite boundary of the bubble, thus slowing down the regrowth rate and the symmetry of the regrowth is

broken by the bubble, some polysilicon may appear at the growth surface[61]. We suppose the epitaxial growth rate is governed by the Ar concentration and that the regrowth stops completely if this concentration reaches a certain amount at the amorphous-crystalline interface.

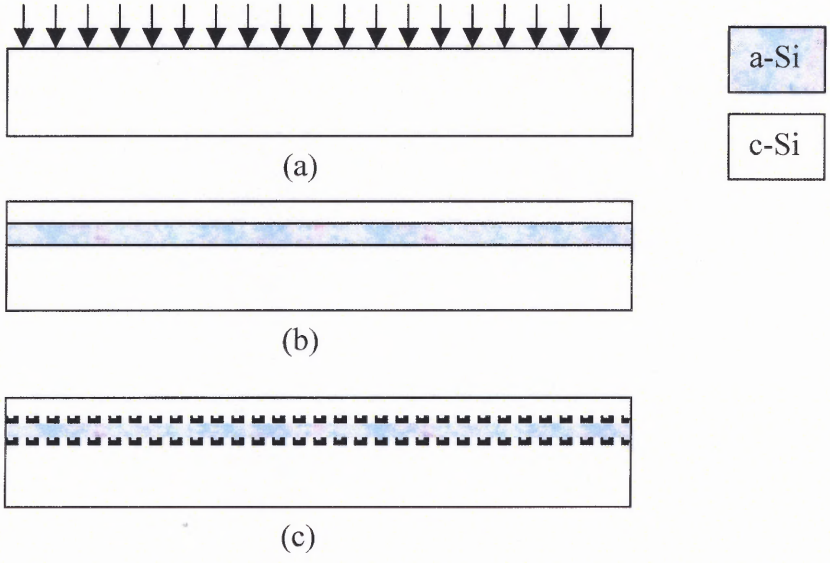

Figure 4.4 (A)Certain dose Ar+ or Ne+ are implanted into silicon wafer at high implantation current; (B)Buried disorder layer is formed after certain implantation; (C)During annealing, epitaxial growth make the buried amorphous layer thinner, and many Ar filled nano-cracks, bubbles appears at growth interface; they stop the epitaxial growth.

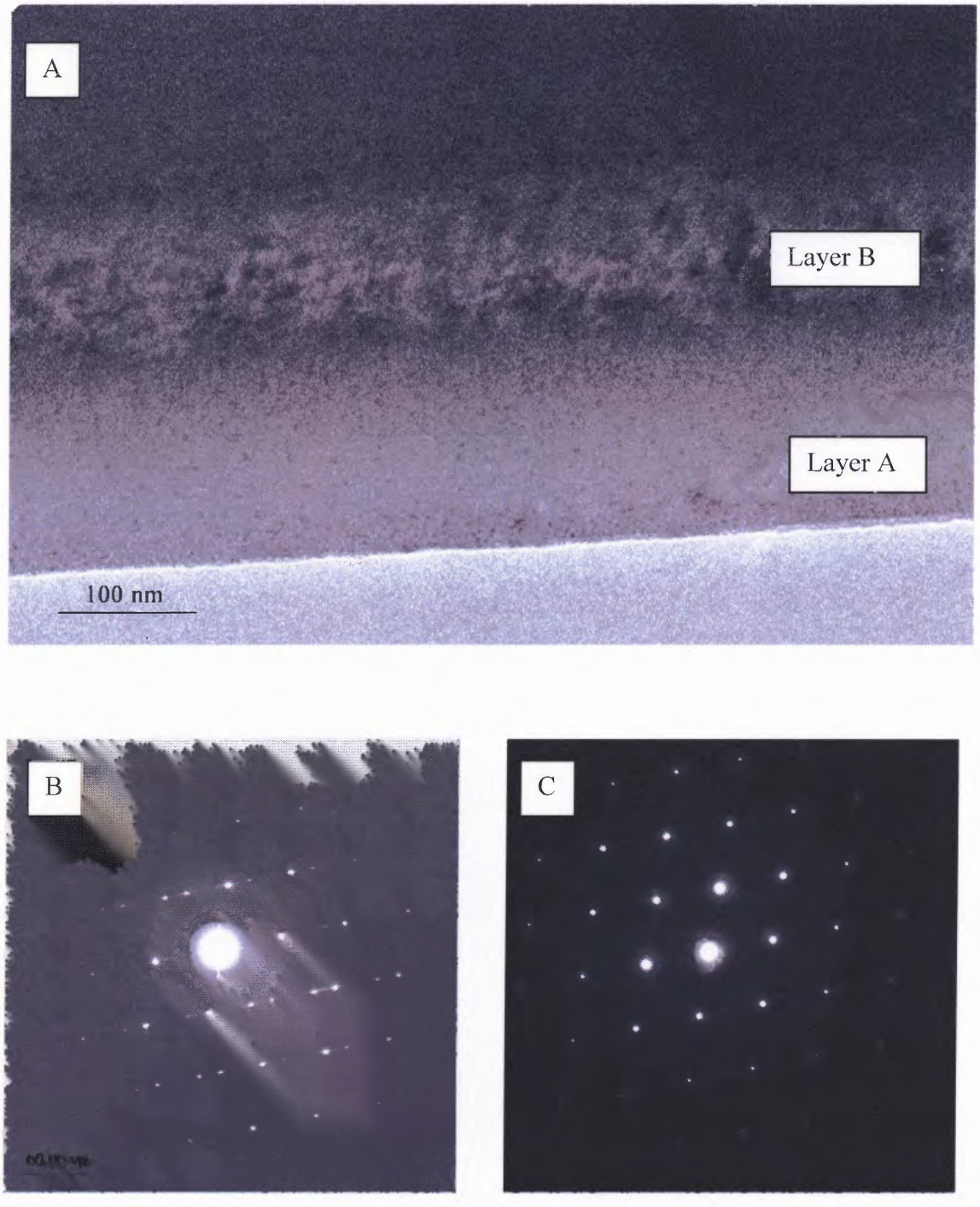

Figure 4.5 (A) Cross section image of Ar implanted wafer annealed at 600 °C; (B) Diffraction image of layer B; (C) Diffraction image of layer A.

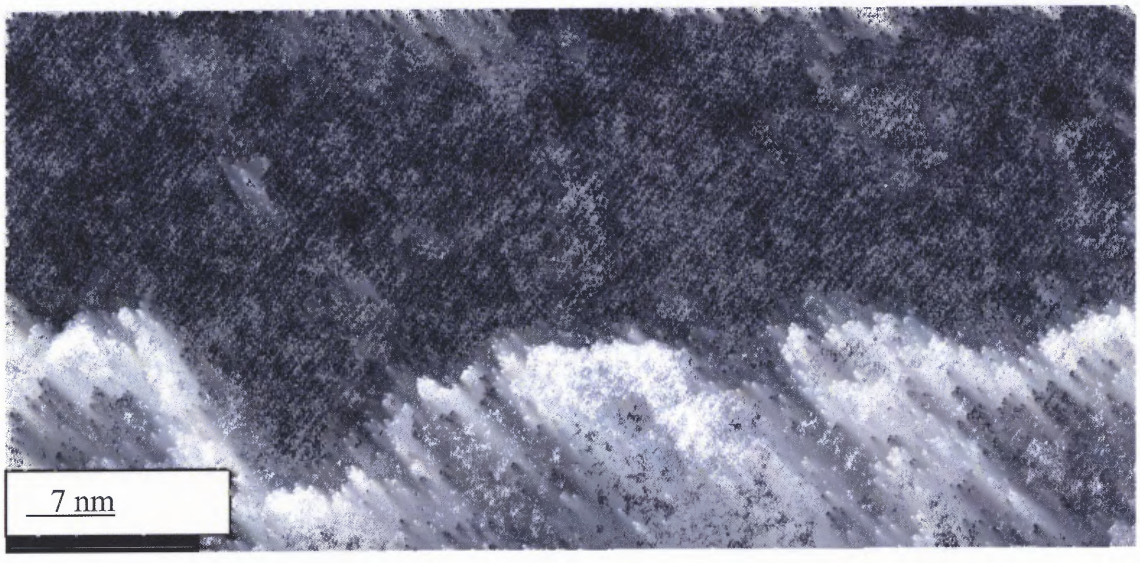

Figure 4.6 TEM picture of the Si sample by Ar Implantation, then annealing. The bright line may be the argon bubbles or nano-cracks at the interface between c-Si and a-Si.

4.5 Summary and Conclusions

In this chapter, silicon wafers are implanted by different elements (He, N, Ne, Ar) at appropriate energy. A H trapping layer will be formed in the depth of ~100 nm from TRIM calculation. Why we choose these implantations, the reason is that two different types of trapping layer are formed, one is vacancy cluster, and the other is gas bubble.

After N^+ implantation at 40 keV, two distinct layers are formed in the silicon wafer. From TRIM calculation result in Fig. 4.2, a vacancy rich layer in the near surface region (0~100nm) which shows mechanical strain of contraction (negative strain). From 100nm ~200nm, this layer represents positive strain because of extra-interstitial and dislocations.

In the case of He^+ implantation, the ballistic mechanisms which produce an excess concentration of vacancy near the sample surface also take place. However, the implanted He^+ atoms diffuse into vacancy rich layer and agglomerate to create bubbles. Finally, only bubbles layer can be formed near 100nm at 15 keV implantation.

Ar or Ne is the member of the noble gases that has received the greatest attention in the past, since they are cheaper and also most widely used noble gas. Compared with He implantation, Ar or Ne atom is bigger and heavier. The implantation of Ar+ ions into Si is known to result in more lattice disorder and argon is particularly hard to out diffuse up to nearly 600 °C.

In our research, Ar or Ne implantation is used to generate defects rich layer in the crystalline Si, but it is very easy for Ar implantation to make absolutely amorphization from the wafer surface to the project range. How to get buried amorphous layer and keep surface layer as crystalline structure is important.

High beam current is known to give in situ annealing during implantation. In this paper, high beam current (~3mA/cm^2) is used to implant Ar^+ into Si samples with a dose ranging from 10^{15} to 4×10^{15} Ar+/cm^2, finding the appropriate substrate temperature that form the buried amorphous layer. After forming the buried amorphous layer, the wafers are annealed at about 600 °C for a certain time. The epitaxial growth can occur in the both sides of the buried amorphous layer. At the same time, we can find some bubbles in this buried disorder layer. We think that the presence of the Ar bubbles acts as a sink for the vacancies.

Through these presences of the bubbles, the amorphous and the crystalline phases are decoupled. Silicon atoms on the boundary of the bubble which faces the amorphous silicon region lose contact with the single crystal at the opposite boundary of the bubble, thus slowing down the regrowth rate and the symmetry of the regrowth is broken by the bubble, some polysilicon may appear at the growth surface. We suppose the epitaxial

growth rate is governed by the Ar concentration and that the regrowth stops completely if this concentration reaches a certain amount at the amorphous-crystalline interface.

CHAPTER 5

THE SILICON-HYDROGEN SYSTEM AND HYDROGENATION PROCESSING

The physics and chemistry of hydrogen in silicon has been the subject of considerable scientific and technological interest for over three decades. This interest has been driven by the omnipresent appearance of hydrogen in silicon processing that always leads to hydrogen incorporation into the substrate, either intentional or unintentional. Importantly, this hydrogen may strongly alter the electrical characteristics of the resultant device by diffusion into active region and passivation of the dopant. Attention has been focused primarily, although not exclusively, on the diffusion of atomic hydrogen, its molecule formation, and its complex formation with and passivation of dopant impurities.

5.1 H Species in Si-H System[64]

"Hydrogen forms more compounds than any other element and hydrogen compounds of all elements excepting noble gases are known"[65] Though hydrogen atom has only one electrons, it however forms a variety of different substances or adducts. All hydrogen compounds hold a number of records:

5.1.1 H^+ - The Carrier of Acidity

Due to its high electron affinity (19.59 eV, i.e. the ionization energy E_0 of neutral hydrogen) and to the absence of any external electron, H^+ penetrates into the electronic cloud of all neutral substances A forming stable adducts AH^+.

5.1.2 H – The Simplest Atom

Due to its simplicity, the determination of the energy spectrum of hydrogen to higher and higher accuracy has ever been the crucial test of microscopic theories. Having an odd number of electrons, it reacts almost immediately with other unpaired electrons.

5.1.3 H_2^+ - The Simplest Molecular Ion

Since H_2^+ is stabilized by one electron only, the problem of calculating its ground-state energy can be solved rigorously. The bond energy and distance of H_2^+ are $0.205E_0$ and $2.00a_0$, respectively. Due to its low bond energy, H_2^+ can be destroyed by proton donation to any other substance except helium and neon.

5.1.4 H_2 – The Simplest Molecule

The minimum of the H_2 total energy is –4.74eV which combined with a zero point energy of 0.22 eV gives a bond energy of 4.52 eV; the bond length is 0.074nm.

5.1.5 H_3^+ - The Smallest Tri-nuclear Molecular Ion

The stability of H_3^+ results from the sum of the H_2 bond energy and proton affinity (4.38 eV). In H_3^+ the nuclei hold the vertices of an equilateral triangle of side 1.66 a_0. In interstellar conditions, H_3^+ is formed with extremely high efficiency via the reaction

$$H_2 + H_2^+ \longrightarrow H_3^+ + H$$

in turn H_3^+ reacts with any other species X to form the adduct XH^+.

5.1.6 H_3 – A Molecule Existing Only in An Excited State

H_3 exists only in an excited state H_3^* and decays spontaneously to H_2+H. H_3^* is formed in an excited state from recombination of H_3^+ with an electron,

$$H_3^+ + e^- \longrightarrow H_3^*$$

in turn, H_3* decays in one of the states with principal quantum number n1=2 via emission of photon, followed by the dissociation in H_2+H,

$$H_3^* \longrightarrow H_3 + hv$$

$$H_3 \longrightarrow H_2 + H$$

5.2 H Diffusion Mechanism in Si

The diffusion of H in Si is complex because of the presence of several charge states and the fact that hydrogen is often present in different forms, namely atomic, molecular (or large clusters), or bound to a defect or impurity. The probability for the formation of these deferent forms is dependent on the defect and impurity concentration in the material and the hydrogen concentration itself. Thus, the apparent diffusivity is dependent on the method of hydrogen insertion. Hydrogen can be introduced into silicon through various process like reactive ion-etching, glow discharge, plasma hydrogenation, or H-ion implantation and consequently each method with its distinct influence on defect or impurity generation in the silicon crystal leads to a different behavior of hydrogen in the material.

Hydrogen atom is light, mobile and very active. Hydrogen diffusion into Si appears to be a mundane issue because it is often believed that diffusivity of H in Si is very high[69,70]. This perception may be attributed to excellent work published by Van

Weirengen and Warmoltz, who measured diffusivity (D_H) at high temperatures and expressed it as[66]

$$D_H = 9.4\times10^{-3}\exp(-0.48eV/kT)\ \text{cm}^2/\text{s}$$

When this expression is extrapolated to lower temperature range in which typical hydrogenation is done, it yields diffusivity of about 2×10^{-9} cm^{-2}/s. This high value of D_H implies that a typical hydrogenation process at 100~400 °C should require only a few minutes for H to diffuse through the entire thickness of Si wafer. However, in practice, the optimum time for hydrogenation by plasma processing ranges from 30 to 60 min, indicating significantly lower diffusivities.

Concentrations of H introduced by typical hydrogenation methods can far exceed the solubility of H in the Si lattice. Fig. 5.1 shows a plot of solubility as a function of temperature. The solubility at 400°C is only about 10^8 cm^{-3} and is lower at room temperature. However, in some paper [67], the H concentrations in excess of 10^{20} cm^{-3} are measured in hydrogenated samples. Some of this reason may be attributed to trapping behaviors of H in Si lattice.

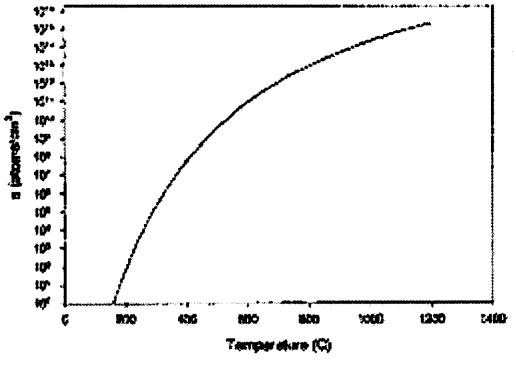

Figure 5.1 Calculated solubility of H in Si lattice as a function of temperature.

In low temperature hydrogenation, H was believed to interact with impurities and defects during the diffusion such as dopants, self-interstitials, vacancies and metals. The interaction forms a variety of complexes, many of which are immobile. In addition to its interactions with other impurities/defects in Si, H itself can form defects, such as dimmers (H_2 and H_2*), platelets, and pile up as H-bubbles at relaxed lattice. These complexes are generally localized in the lattice (therefore referred to "stationary traps"). Formation of these complexes has a profound influence on the flow of H during its diffusion. In essence, these process cause depletion of H from the diffusion flux by trapping or stagnation. The capture rates of H in formation of these complexes are much higher than the release rates. Thus, once formed at the processing temperature, they are fairly stable with a low probability of dissociation (detrapping) and generally require higher temperature to dissociation.

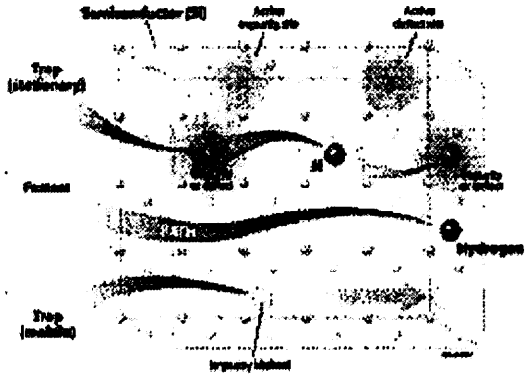

Figure 5.2 Schematic illustration of various path for H diffusion in Si.

Figure 5.2 illustrates various bulk diffusion processes of H in Si. This figure depicts three types of diffusion mechanism in the bulk of Si; the basic interstitial BC-to-BC diffusion, trapping and detrapping at stationary traps and diffusion via "mobile traps" to

account for formation of complexes such as H-V (V=vacancy) pair that can readily diffuse and transport H [68]. Because H can associate itself with impurities and defects in Si, its effective "solubility" is much high than in the perfect Si lattice. An important property of traps is that their trapping and detrapping rates are temperature dependent. In particular, detrapping rate can increase at higher temperature releasing free H to diffuse rapidly. This can be a valuable means of overcoming diffusivity limitation in which traps can be used as H trapping layer.

5.3 H in Silicon that Contains Defects

Ion implantation into crystalline silicon breaks chemical bonds and creates defects in the implantation zone. This effect is crucial in the ion-cut process: Since the diffusivity of H in crystalline silicon is very high, one would expect intense out diffusion of the H-implantation during the heat treatment of the silicon sample. However, the hydrogen gets trapped at the proton implantation induced defects by passivating the dangling bonds in the implantation zone, where the number of lattice defects is very high.

As an example, Fig. 5.3 illustrates possible local Si-H defects, formed at a silicon vacancies and lattice interstitials. A vacancy in the silicon lattice leaves four dangling bonds behind, which can be passivated with H-atoms.

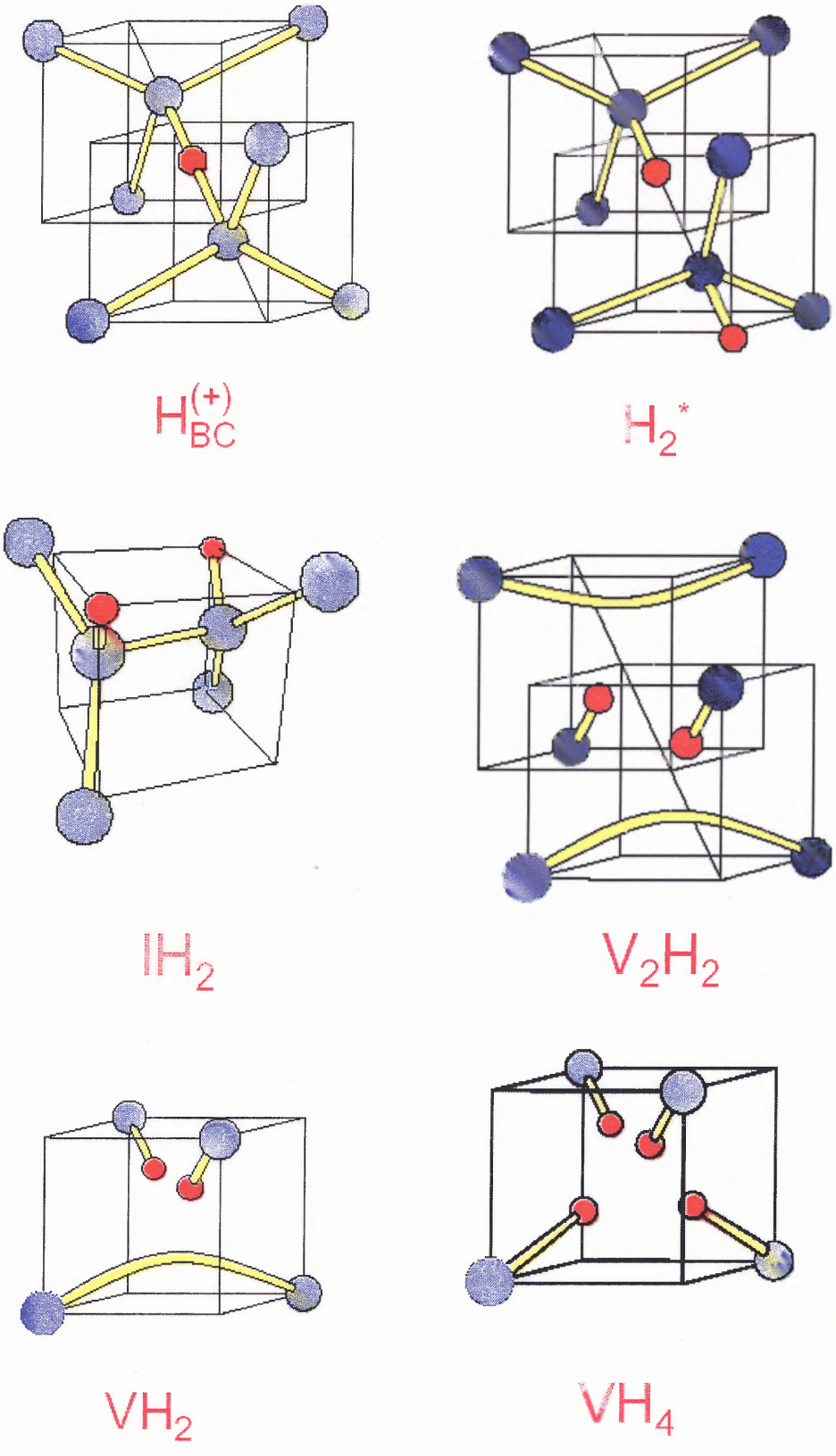

Figure 5.3 Interstitial and vacancy type defects in Si lattice.

Hydrogen in crystalline silicon has been of great theoretical and experimental interest in recent years. A lot of advances in the theoretical and experimental research of hydrogen silicon system in terms of hydrogen complex formation with silicon and impurity atoms and hydrogen molecule formation were achieved [71,72]. Many insights about hydrogen complex formation in H-ion-implanted silicon have been gained from IR vibration spectroscopy. A multitude of vibration bands in silicon that contain H were found, far more than the modes attributed to Si-H, Si-H_2, and Si-H_3. Stein at al. showed that Si-H bonds associated with ion implantation induced vacancy and interstitial-related displacement damage are less stable than surface traps of hydrogen at internal voids. [73] This is in accordance with the evolution of Si-H complexes into H_2-gas bubbles upon annealing.

Detailed information about the evolution of Si-H complexes in H ion-implanted silicon were gained by infrared vibrational studies by Weldon and Chabal et al.[74]. Implanted H atoms form complexes of the form VxHy and IxHy where V denotes a silicon vacancy and I denotes a silicon interstitial, and the subscript have values of x=1 and 2 and y=1-4. Also observed was the so-called H_2* complex, a hydrogen molecule formation, where one H atom is located at the bond centered site and the other at the antibond site with a silicon lattice atom residing in between the H_2 bond. Upon annealing of the H ion-implanted samples, the IR studies uncover a net loss of bound hydrogen and agglomeration of hydrogen at existing vacancies. A comparison of the infrared vibrational studies with elastic recoil detection analysis, an analysis method which monitors not only atomic hydrogen but also molecular hydrogen, revealed that a net

conversion from Si-H complexes into H_2 takes place at elevated temperatures. This is in agreement with the observations of H_2 filled gas bubbles in the implantation zone.

Earlier investigations led to discover the astonishing result that H can insert itself between Si-Si bonds at the bond-centered site to form extended structural defects that are described as hydrogen stabilized platelets.[75] These H-platelets turn out to be the nuclei of H_2 gas bubbles, which lead to ion-cutting in H-implanted material.

Cerofolini et al.[77] hypothesized, that the H_2 molecules that formed within these bubbles do so with a bond length almost equal the H_2 bond length in vacuum, which leads to an energy gain that counterbalance the strain build up around the bubble in the silicon crystal. Recent Raman spectroscopy measurements verified this assumption. The vibration frequency of H_2 molecules is practically the same as the well-known value for gaseous hydrogen.[76]

The interaction of hydrogen in silicon with acceptor or donor dopants turned out to have a considerable influence on the kinetics in the formation of H-platlets and H_2-gas bubbles, which induce the ion-cut.

Studies of neutralization of shallow acceptors in silicon evolved from the perspective that there is a Si dangling bond near each acceptor, and therefore its passivation should eliminate a hole and result in an increased resistivity. First studies of the interaction of hydrogen with acceptors in silicon showed the neutralization of boron by monoatomic hydrogen to be maximized near 100 °C, being limited by diffusion at lower temperatures and by the dissociation of Si-H-B complex at higher temperatures.

Hydrogen in-diffusion experiments into crystalline silicon with a buried layer of high boron concentration showed significant trapping of hydrogen within the boron

doped layer. The amount of H-atoms trapped exceeds by far the amount of boron atoms present in the layer. Theoretical studies showed, that the change of Fermi level, induced by the boron concentration profile has an influence on the charge state. Also, kinetic models for hydrogen passivation of the acceptors indicated that the hydrogen boron capture radius is large, and that molecular formation of H at the boron trap site lead to the trapping of 8 to 12 hydrogen atoms by one boron atom in the silicon crystal.

5.4 Molecular Hydrogen Traps within Silicon

5.4.1 Hydrogen at Tdi

Recent first principle calculations[78] find that $(H_2)_i$ is sited at tetrahedral positions in the silicon lattice aligned along [100] or [111], and possessing a molecular stretch frequency directly comparable to the 3789 cm^{-1} mode observed by infrared and Raman spectroscopy. The observation of a single IR Raman active mode is consistent with the molecule being aligned along [110], and unable to rotate.

5.4.2 Lattice Defects[79,80,81]

Several types of extended defects in silicon are known to exist, with associated vibrational bands around 2100 cm^{-1}, so the behavior of H_2 trapped at such sites becomes of interest in understanding the effects of plasma treatment on silicon.

a. <111> platelets

Of the models so far suggested for the <111> platelet, TEM studies and calculations favor the structure with a pair of hydrogen atoms saturating each broken bond between (111) planes displaced apart ~3A. The stretch frequency for the molecule lie at 4385 cm^{-1} for H_2. The modes of the hydrogen saturating the surrounding silicon atoms fall between 2117 and 2098 cm^{-1}. The experimental values for platelets lie at ~2110 and 1960 cm^{-1}. The molecule has a bond length of 0.748 A when sited in the platelet.

b. Voids(multi-vacancy)

An alternative structure at which molecule might be sited, would be a microvoids in the lattice.

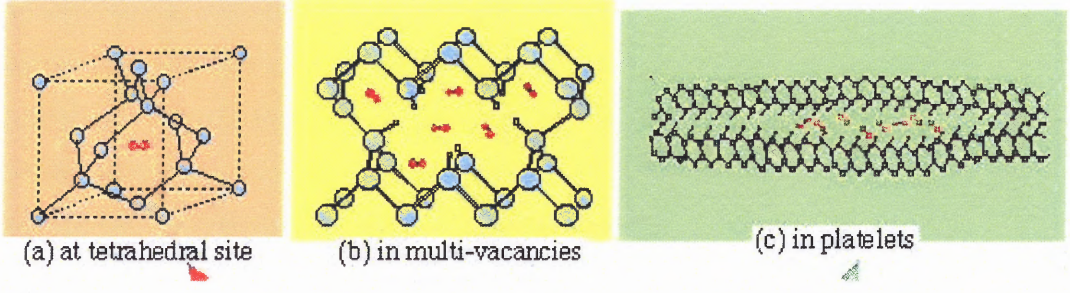

Figure 5.4 Positions in which hydrogen molecule can be resided in Si lattice.

In summary, the research on the hydrogen silicon system showed the apparent diffusivity of atomic hydrogen in the temperature range up to 300 to 400 °C approaches the values from Van Wiering and Warmholz relation only under conditions of low hydrogen concentration and low impurity contents. This is due to the lower probability of self-trapping of hydrogen by molecular or H-platelets formation, and the lower

probability of hydrogen to get trapped by lattice defects and acceptor or donor dopant ions. If enough defects appear in certain area of Si lattice, lots of hydrogen will be trapped and stored in this area. This phenomenon will help us develop the efficient hydrogenation step for our new SOI fabrication method.

5.5 Low Energy H Plasma Reacting with Implanted Wafer

5.5.1 Processing Conditions

In this dissertation, we use Tegal-100 plasma system to process our sample. The maximum RF power is about 300 W and the chamber pressure is 100~600 mTorr. The temperature is 200~350 °C and the processing time is 1~4 hours. These samples were measured by transmission FTIR, then annealed at 600 °C. SEM is used to observe the surface of samples.

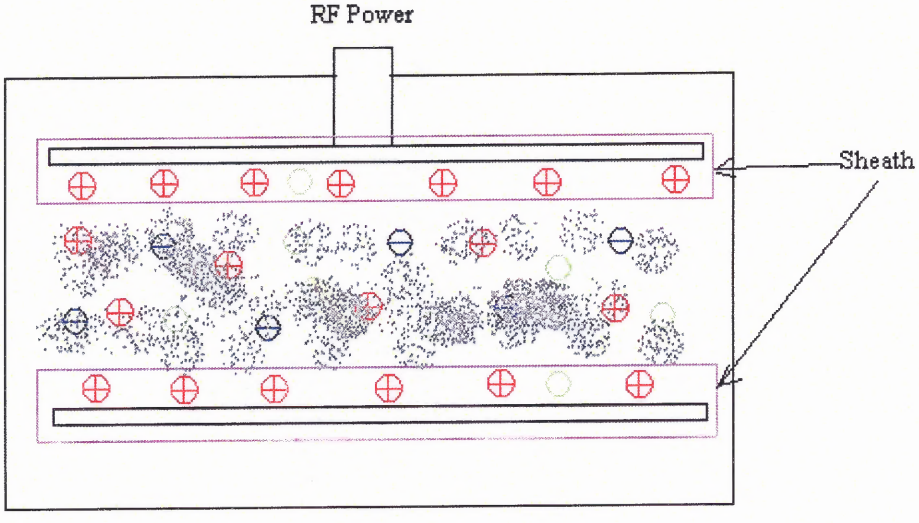

Figure 5.5 Schematic graph of Tegal-100 RF plasma system.

5.5.2 Transmission FTIR and SEM Results

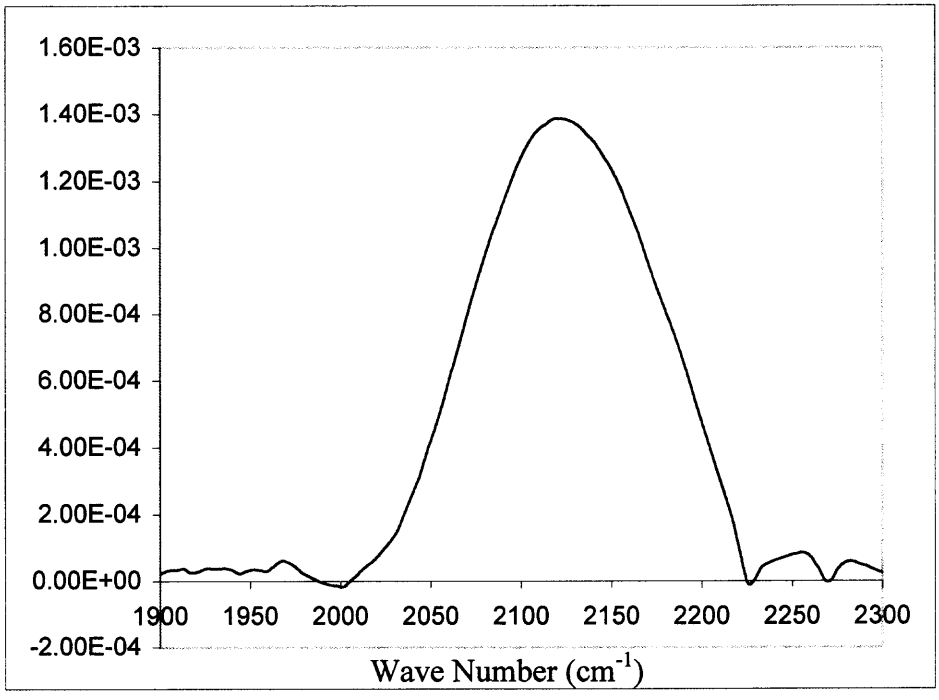

Figure 5.6 FTIR result of pre-implanted silicon samples hydrogenated by low energy H plasma at 200~350 °C.

Figure 5.7 SEM pictures of Si samples surface after hydrogenation.

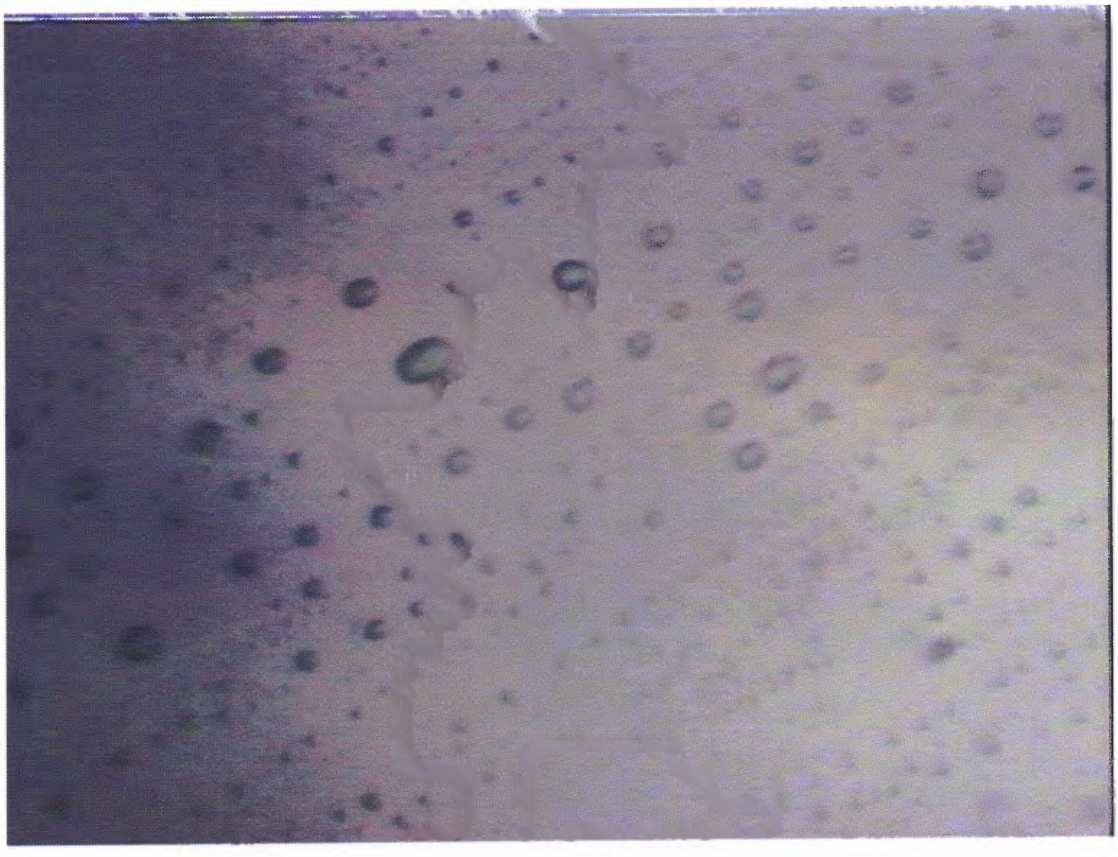

Figure 5.8 Optical picture of Si sample surface after annealing at 600 °C.

FTIR result shows a big absorption band near 2100 cm^{-1}. This absorption band is assigned to H bond in the internal surface. SEM pictures show a small etch effect after low energy H plasma processing. After annealing at 600 °C, some bubbles appear at the surface of Si samples, but these bubbles are not smooth in the whole wafer's surface.

5.5.3 Diffusion and Reaction Mechanism of Low Energy H Ions with Pre-implanted Si Wafer

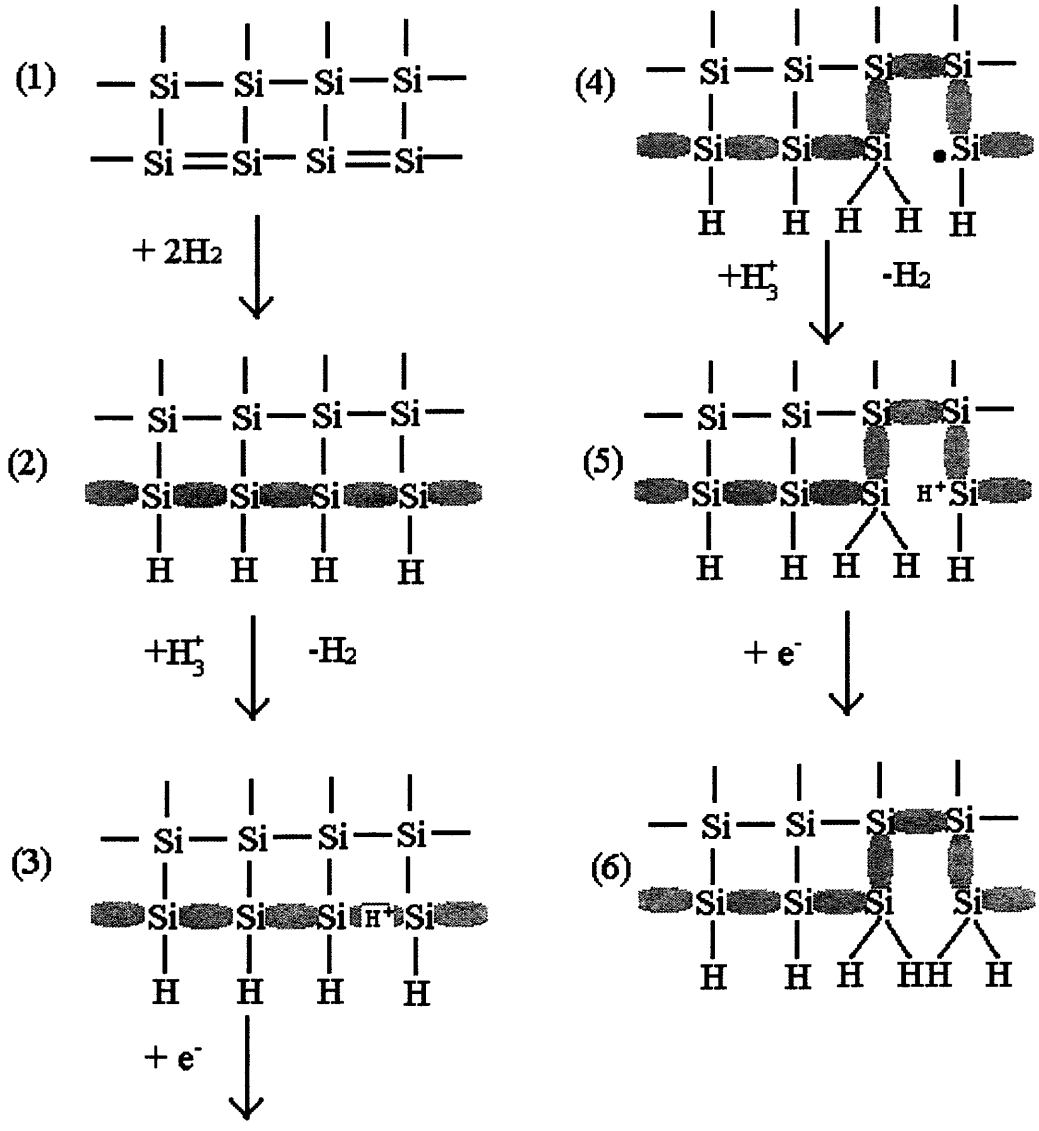

Figure 5.9 Sketch of silicon silanization in a hydrogen plasma.

In general, putting a silicon crystal in a hydrogen atmosphere at a given temperature will result in a low hydrogen concentration, lower than its solid solubility at the considered temperature. A more effective way to insert hydrogen at low concentration in silicon is via redox reactions producing atomic hydrogen at the silicon surface. Higher hydrogen

concentrations can only be achieved by more energetic preparation methods, like plasma treatment or ion implantation.

In weakly ionized hydrogen plasma ions are originally produced via H_2 ionization

$$H_2 \longrightarrow H_2^+ + e^-$$

in turn, H_2^+ reacts fast with environmental H_2 to form H_3^+ and H^+; H_3^+ is stable until it captures an electron thus decaying to H_2 and H via the dissociative recombination pathway while H can be destroyed by reaction with another hydrogen atom to form H_2 or with H_2^+ to form H_3^+. The expected abundances of various hydrogen species in a weakly ionized plasma are therefore $H_2 >> H_3^+ \approx H > H_2^+ >> H^+$[64].

Due to the presence in the plasma of molecular and atomic hydrogen and the extremely strong Bronsted acids H_3^+ and H_2^+, the exposure of a silicon surface to a weakly ionized hydrogen plasma produces the formation of silanic bonds and the protonation of Si-Si bonds exposed to the plasma. Fig.5.9 sketches the details of one (among others) plausible silanization path in a plasma without bias:

(1) the reconstructed surface;

(2) chemisorbs dissociatively H_2 forming silanic bonds;

(3) the plasma exposed Si-Si bonds (dashed) react with H_3^+ forming bond-centered H^+;

(4) the bond-centered H^+ reacts further with an electron from the plasma to form a silanic bond and a silicon radical;

(5) this radical reacts with another H_3^+ ion to form a SiH^+ center;

(6) the SiH^+ center reverts to a silanic center by capturing another electron from the plasma;

The overall process increases both the silanization degree of the surface and the number of Si-Si bonds exposed to the plasma, even beneath the original surface. The silanization process cannot continue indefinitely since sooner or later Si_nH_{2n+2} volatile molecules will be formed thus resulting in a surface etching and exposure of non-hydrogenated silicon to the plasma.

Some processes occur together with surface hydrogenation, essentially related to the migration into the bulk of fast diffusing hydrogen (H or H^+); these species are expected to migrate until they are gettered by impurities, pre-existing defects, or plasma-induced defects. Process-induced defects are expected to play a special role when the silicon target is negatively biased with respect to the plasma. In this case, the deposition of charged species (H_3^+, H_2^+ and H^+) with sufficient kinetic energy generates Frenkel pairs in the subsurface region. The point-defect generation rate is in turn responsible for diffusion in the bulk, formation of extended defects, their interaction with hydrogen, etc. The theoretical prediction of the net generation rate would be possible if the mass and energy distributions of charged projectile were known; in the absence of a complete knowledge of these distributions, the damage imparted to silicon by exposure for a certain time to a weakly ionized plasma with a bias is difficult to describe quantitatively.

Plasma treatment is a very effective way for inserting a high hydrogen amount into silicon. To some extent the hydrogen-related defects formed in plasma-treated silicon are similar to those formed in hydrogen-implanted silicon.

Since the binding energy of hydrogen at a silicon surface is higher than the binding energy in the molecule, silicon exposure to a hydrogen atmosphere at sufficiently high

temperature produces a hydrogenation of the surface with the formation of a silanized surface.

The total absorbed amount was found to be accumulated at the surface or diffused into the bulk. Even though control samples did always show an appreciable surface hydrogen contamination, in plasma-exposed samples a higher surface peak was found; this difference is ascribed to the hydrogen-rich layer formed during the process. This surface accumulation, of difficult quantification due to the pre-existing hydrogen contamination, will henceforth be ignored and the attention will be concentrated on the in-diffused hydrogen.

The hydrogen diffusion into the bulk from the deposited surface layer and the growth of the displacement field differ according to the substrate and deposition conditions. A preliminary study of silicon hydrogenation kinetics by exposure to plasma with no bias for 3 to 8 h showed that the kinetics was exhausted after the first 3 h. For longer exposure, therefore information will be got on the gettering efficiency of dopants, and pre-existing or process-induced defects[82].

In our research, silicon wafer will be implanted to form a trap layer for H. In this trap layer, there are many vacancies, interstitials and micro-voids. Due to the presence in the plasma of molecular and atomic hydrogen and extremely strong Bronsted acids H_3^+ and H_2^+, we propose the surface of Si wafer can be modified by H^+, H_2^+, H_3^+ in H-plasma. Hydrogen species damage the surface strained Si-Si bonds, H_2 can readily dissociate, bind to the surface and diffuse into the Si bulk at low temperature (150~200 °C). At higher temperature (300~350°C), the trapped in silane-like species will be detrapped, and H atoms will diffuse deeper into Si bulk. When these atoms meet the buried disorder

layer and bubbles, they will form another Si-H structure and Hydrogen molecular accumulated in the interstitial voids. This model can be partially verified by Fig. 5.10

The buried disorder layer traps large amount of hydrogen and this effect makes hydrogen diffusion continuously from out-H-plasma to the disorder layer. At the same time, the induced-defects by H plasma processing in the top crystalline layer will also be trapped by the buried disorder layer.

Finally, we can get a heavily hydrogenated buried layer that can be used for SOI exfoliation as shown in Fig 5.11.

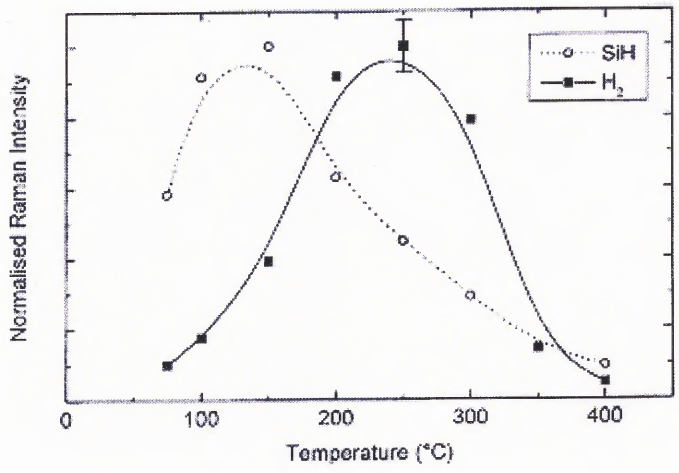

Figure 5.10 Dependence of the integrated SiH and H_2 Raman signal in Si:P on the sample temperature during hydrogen plasma treatment.[83]

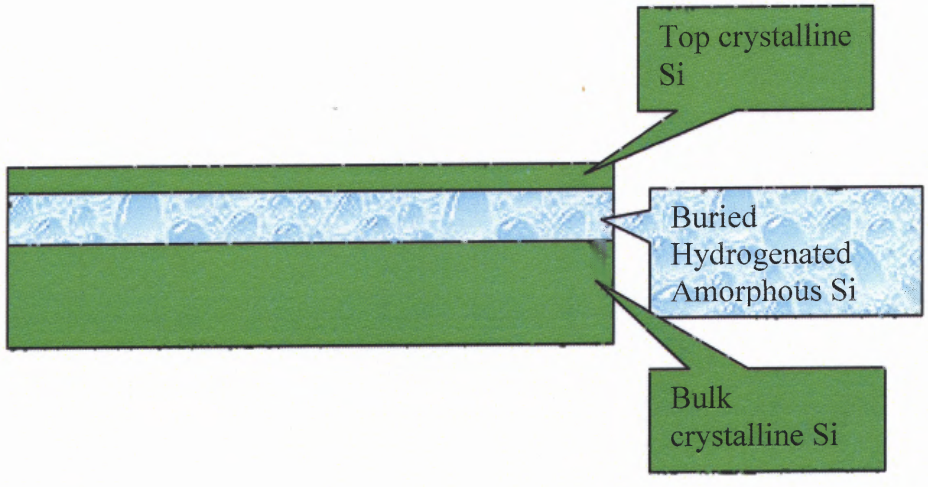

Figure 5.11 Schematic structure of Si wafer after H-plasma processing.

5.6 Pre-implanted Wafer Processed by High Energy Plasma

Plasma immersion ion implantation (PIII) is a burgeoning technique offering many applications in materials and semiconductor processing. In PIII, the sample is immersed in plasma from which ion are extracted and accelerated through a high voltage sheath into the target.

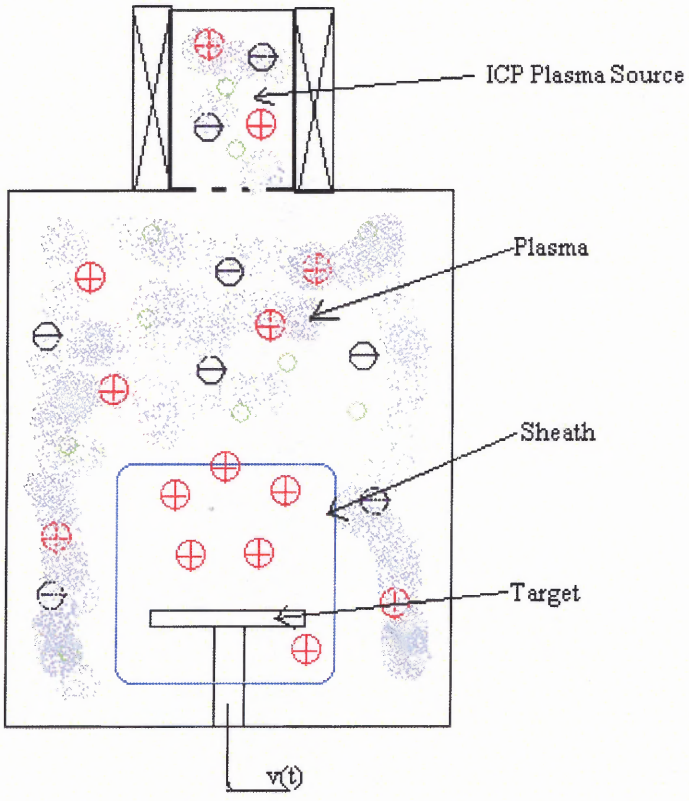

Figure 5.12 Schematic figure of HK PIII system. The target wafer is immersed in a quasi-neutral plasma and a negative DC bias corresponding to the desired implantation energy is applied to the target. A typical implantation dose rate is around 10^{15}~10^{16} $cm^{-2}s^{-1}$[84].

5.6.1 Former Results of PIII for Making SOI Wafer

In spite of the demonstrated viability of the PIII/ion cut technique, refinement of the technology must be made. One of the most important parameters is the thickness uniformity of the SOI. For an ion cut process utilizing conventional beam-line ion implantation with mechanical scanning, the implantation energy and angle are the same over the entire wafer. Any variation in the silicon film thickness depends on the crack mechanism, that is, how smoothly the silicon layer separates along the micro-cavity plane. However, for PIII, since the whole wafer is implanted simultaneously inside the plasma, there is the possibility that the projected range of the implanted hydrogen can vary laterally on the wafer due to plasma nonuniformity and sample stage effects.

Fig. 5.13 displays the thickness distribution of the silicon layer across the wafer. The x-scale shows the distance of the measured area from the center of the wafer. It can be observed that the silicon overlayer thickness is quite uniform in the center area and drop toward the edge.

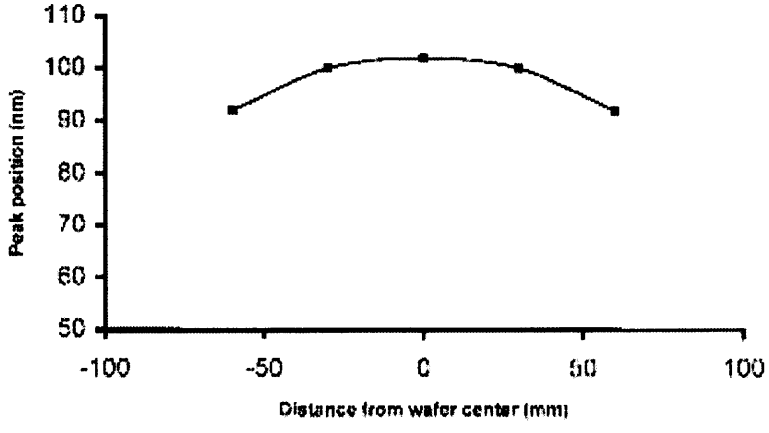

Figure 5.13 Hydrogen projected ranges across the 150-mm wafer determined by SIMS[85].

In PIII, it is usually assumed that ions impact the wafer at a normal angle. As shown in Fig. 5.14, there are two velocity components, Vr that is the radical velocity and Vz which is the axial velocity. The implantation angle θ is defined by

$$\tan(\theta) = V_z / V_r$$

The axial velocity determines how deep the ion will traverse into the silicon. Based on the field lines, ions implanted into the center of the wafer have zero Vr, but the incident angle becomes progressively more glancing toward the edge. Closer to the edge, ions are collected not only from the region directly above but also from the side. The radical velocity component is increased and the incident angle is shallower resulting in a smaller projected range.

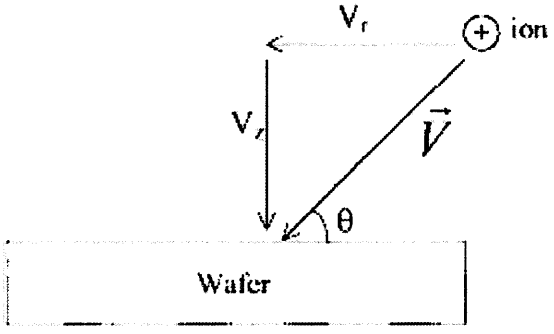

Figure 5.14 Schematic diagram of the incident angle.

Without the line-of-sight limitation, plasma immersion ion implantation (PIII) emulates conventional beam-line ion implantation in inner surface modification pf industrial components. However, dose uniformity on the inner surface is critical. It is found that the retained dose is not uniformly distributed on the inner surface and the maximum dose is observed away from the edge. The exact location of the maximum dose,

which varies with the implant pulse duration, is closer to the center when the pulse width is longer.

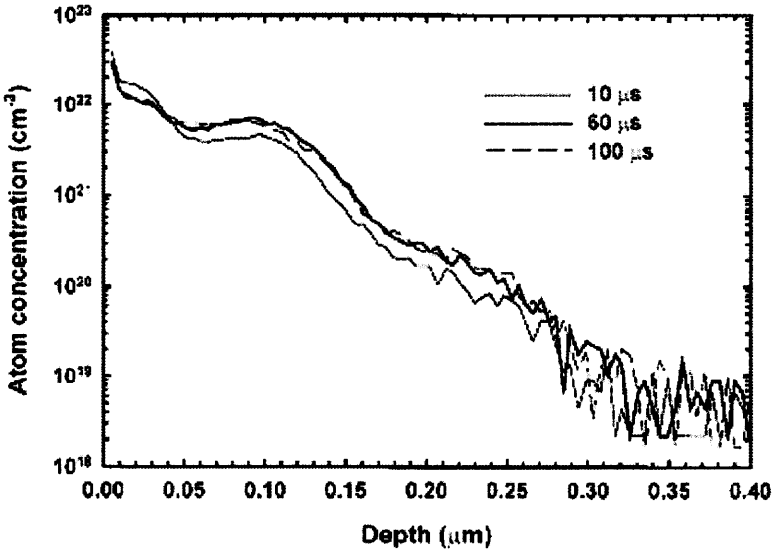

Figure 5.15 SIMS depth profiles of silicon samples processed by H PIII at 20 keV[86].

A high surface hydrogen concentration exists, and the hydrogen in-depth distribution is broader, sometimes extending from the near-surface region to the projected range of H_2^+ if a large quantity of H_2^+ and H_3^+ coexists in the plasma. As the entire wafer is immersed in a hydrogen plasma during PIII, hydrogen atoms can adsorbed on to the wafer surface during the "off-cycle" of the voltage pulse and subsequently diffuse or be knocked into the substrate by ion mixing. If this surface hydrogen concentration is high, it can impede wafer bonding and leaves patches of voids on the acceptor wafer. Another cause of the broadening in the hydrogen profile is the sheath expansion at the beginning of each pulse. When a negative pulse is applied to the wafer, electrons are repelled on the time scale of 10^{-10} s and a plasma sheath is formed. The sheath continues to expand and

ions are brought in motion on the time scale of 10^{-7} s. The time to achieve a static Child law sheath state is on the order of 10 ns or longer. Because the sheath propagation is much slower than ion movement, this period can be described by the quasistatic Child law. Although the ions in quasistatic Child law sheath are implanted at a voltage almost equal to the applied voltage, the ions in the sheath, especially those in the vicinity of sample surface, are implanted at a lower energy. The lowest energy can be near zero if the initial position of the hydrogen ion is just above the wafer at the beginning of the pulse.

In order to attain uniform implantation across the whole wafer, the difference in the incident angle and ion energy must be minimized. In this dissertation, silicon wafer was implanted at first. The buried disorder layer will be formed. When this wafer is processed by H plasma immersion implantation, this buried disorder layer will help trap the H species. Finally we can get the smoothly layer transfer.

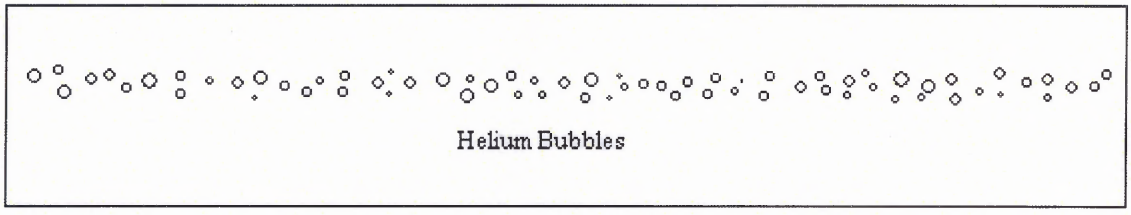

Figure 5-16 (A) Silicon wafer was implanted by He at 20 keV and the buried disorder layer was formed.

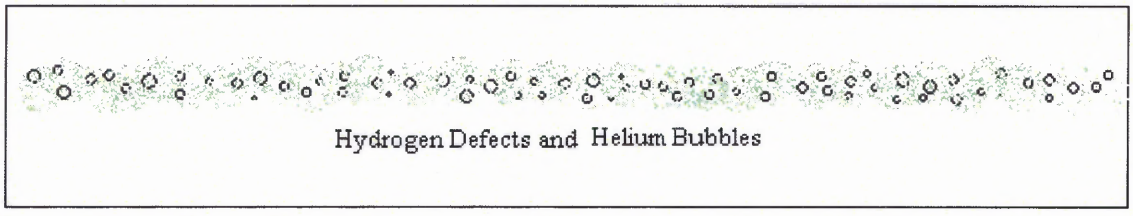

Figure 5-16 (B) The pre-implanted wafer was hydrogenated by PIII at negative bias 20~25 kV.

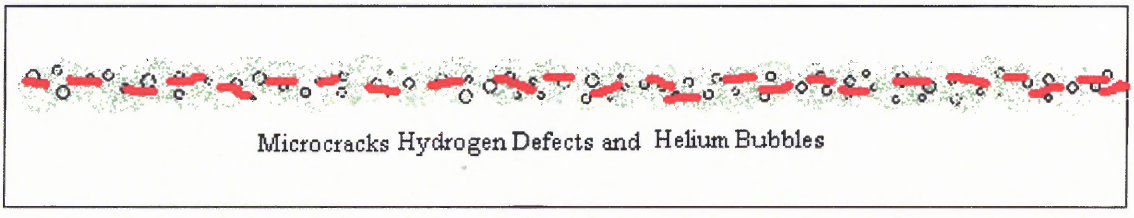

Figure 5-16 (C) The hydrogenated wafer was annealed at 600 °. The microcracks were formed along the buried disorder layer.

5.6.2 SEM Pictures of Pre-implanted Silicon Wafer Hydrogenated by PIII

We choose three types of 4" silicon wafers, B implanted at 200 KeV 5×10^{15} cm^{-2}, Ne implanted at 170 KeV, 5.0×10^{15} cm^{-2}, no pre-implantation. Then all these samples were hydrogenated by plasma ion immersion at 20 kV, 20 min, pulse duration 60 μs. After annealed at 600 °C for 30 min, the wafers were observed by SEM in center and edge.

1. B implanted at 200 KeV 5×10^{15} cm^{-2}

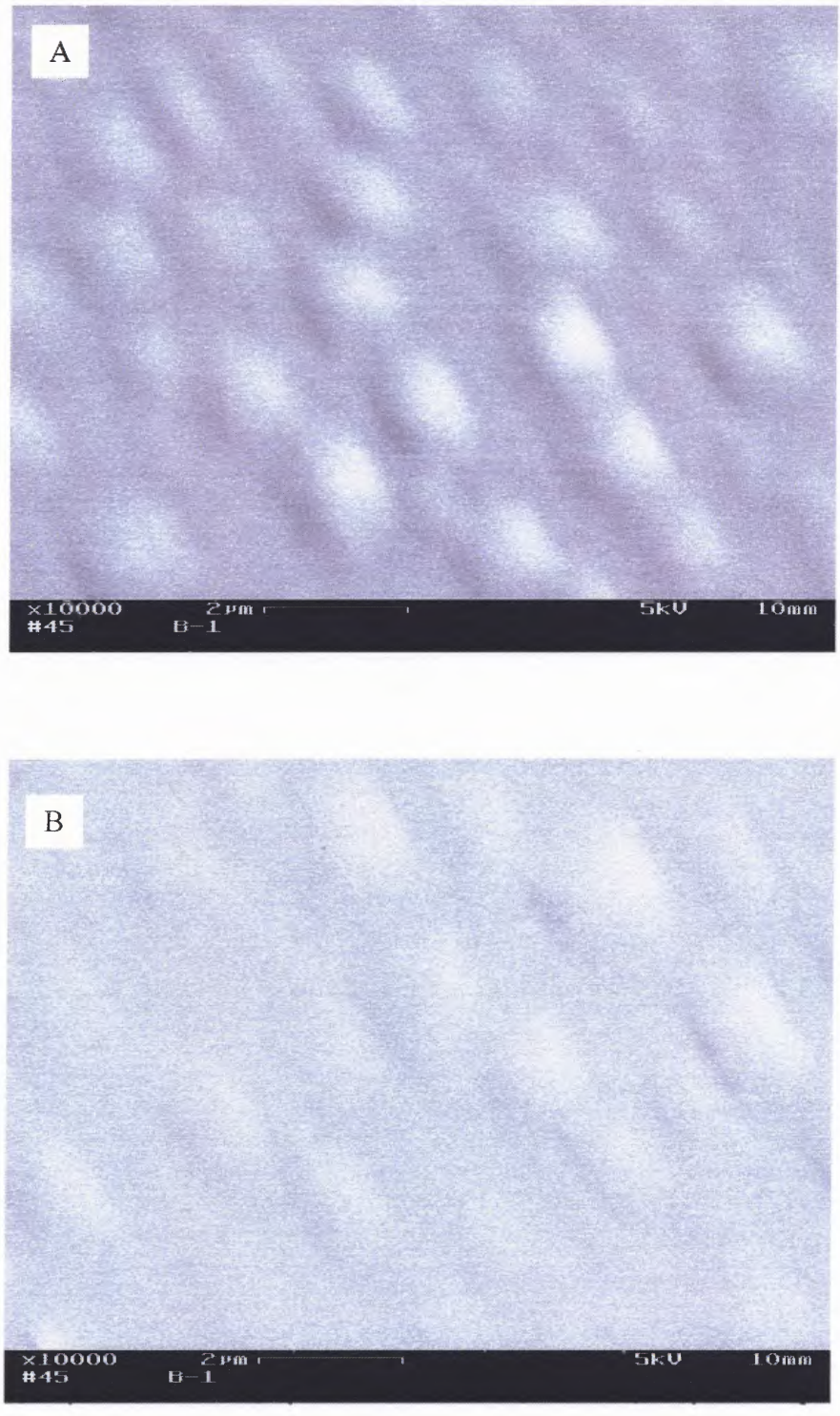

Figure 5.17 SEM pictures of silicon wafer's surface oby B implanted, then H PIII (A) Center area, (B) Edge area.

2. Ne implanted at 170 KeV, 5.0×10^{15} cm^{-2}

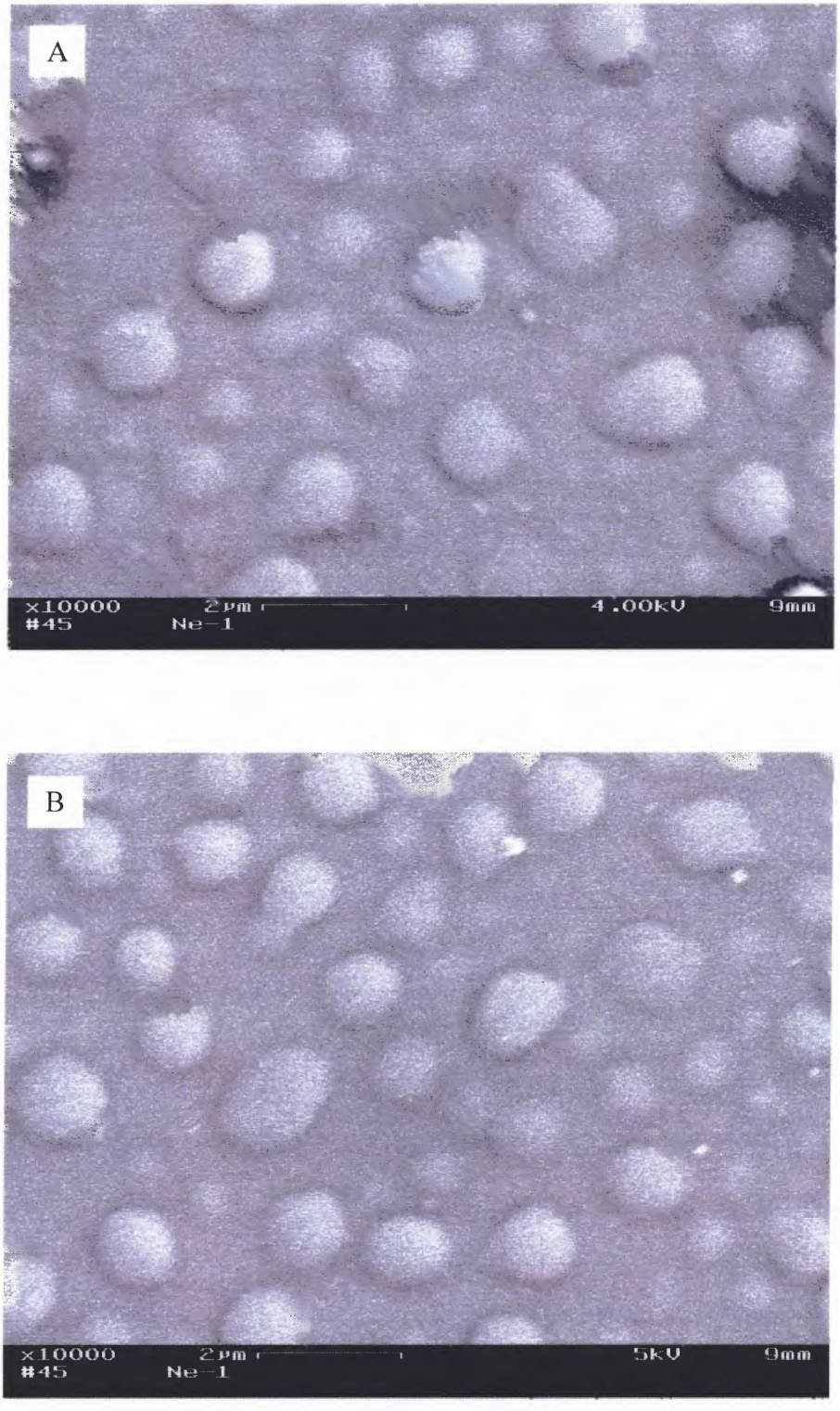

Figure 5.18 SEM pictures of silicon wafer's surface by Ne implanted, then H PIII (A) Center area, (B) Edge area.

3. Only PIII processing

Figure 5.19 SEM pictures of silicon wafer's surface by H PIII (A) Center area, (B) Edge area.

From these SEM pictures (Fig.5.17~5.19), we can find

(1) For Ne pre-implanted sample, bubbles have same density in the center and edge area. However, in B pre-implanted and no pre-implanted sample, there are more bubbles in center area than those in edge area.

(2) Comparing the bubble size in three samples, B and Ne pre-implanted samples have nearly same bubble size that is ~ 1μm. No pre-implantation samples have smaller bubble size that is 0.6~0.8 μm.

So, silicon wafers were implanted by inertial gas to form a buried disorder layer may help trap H species and make the H concentration smooth in the whole silicon surface.

5.6.3 FTIR and AFM Results of Pre-implanted Samples Hydrogenated by PIII

Two types of silicon wafers are choose.

Sample A, Si(100) PIII processing, 400 μS, 60Hz, 25 KeV 22min

Sample B, Si(100), Ne 60 KeV, PIII processing same as sample A

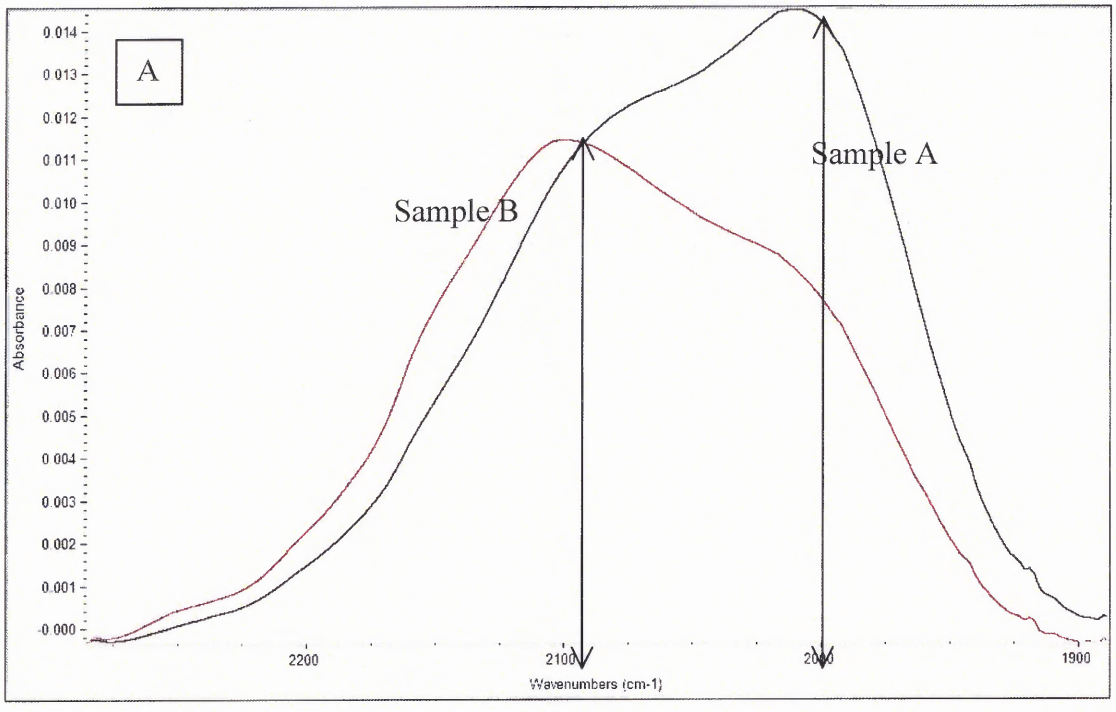
A
Sample A
Sample B
Absorbance
0.014
0.013
0.012
0.011
0.010
0.009
0.008
0.007
0.006
0.005
0.004
0.003
0.002
0.001
-0.000
2200
2100
2000
1900
Wavenumbers (cm-1)

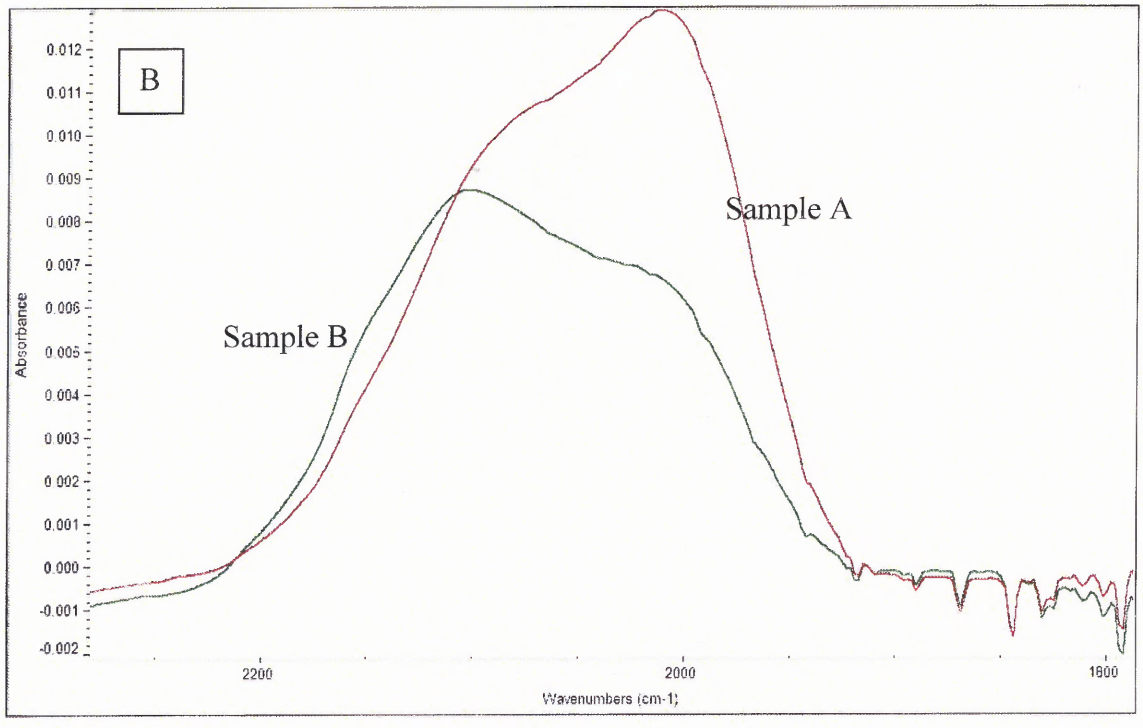
B
Sample A
Sample B
Absorbance
0.012
0.011
0.010
0.009
0.008
0.007
0.006
0.005
0.004
0.003
0.002
0.001
0.000
-0.001
-0.002
2200
2000
1800
Wavenumbers (cm-1)

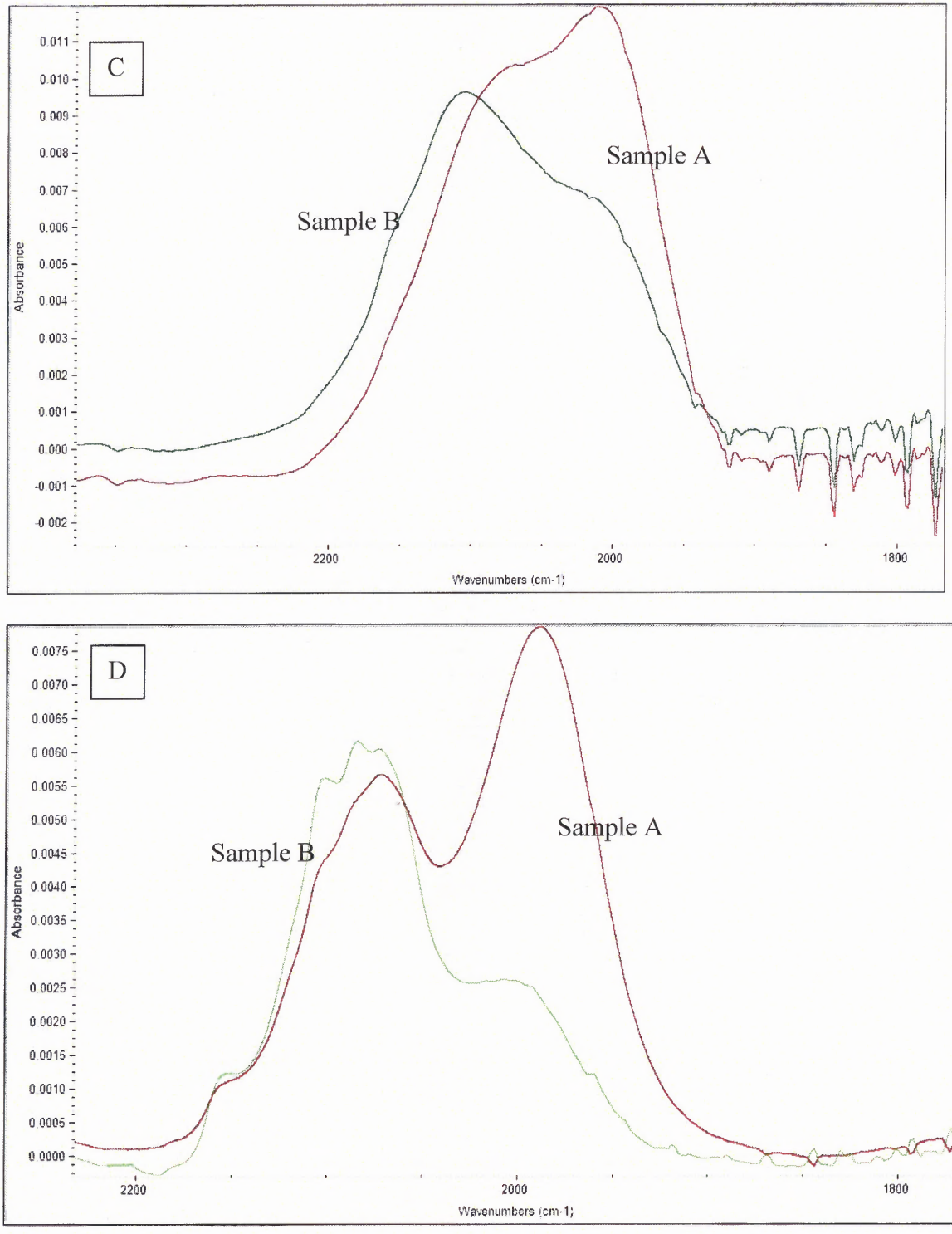

Figure 5.20 FTIR spectrum of Sample A and B, (A) No annealing; (B) Annealed at 100 °C; (C)annealed at 230 °C (D) Annealed at 400 °C

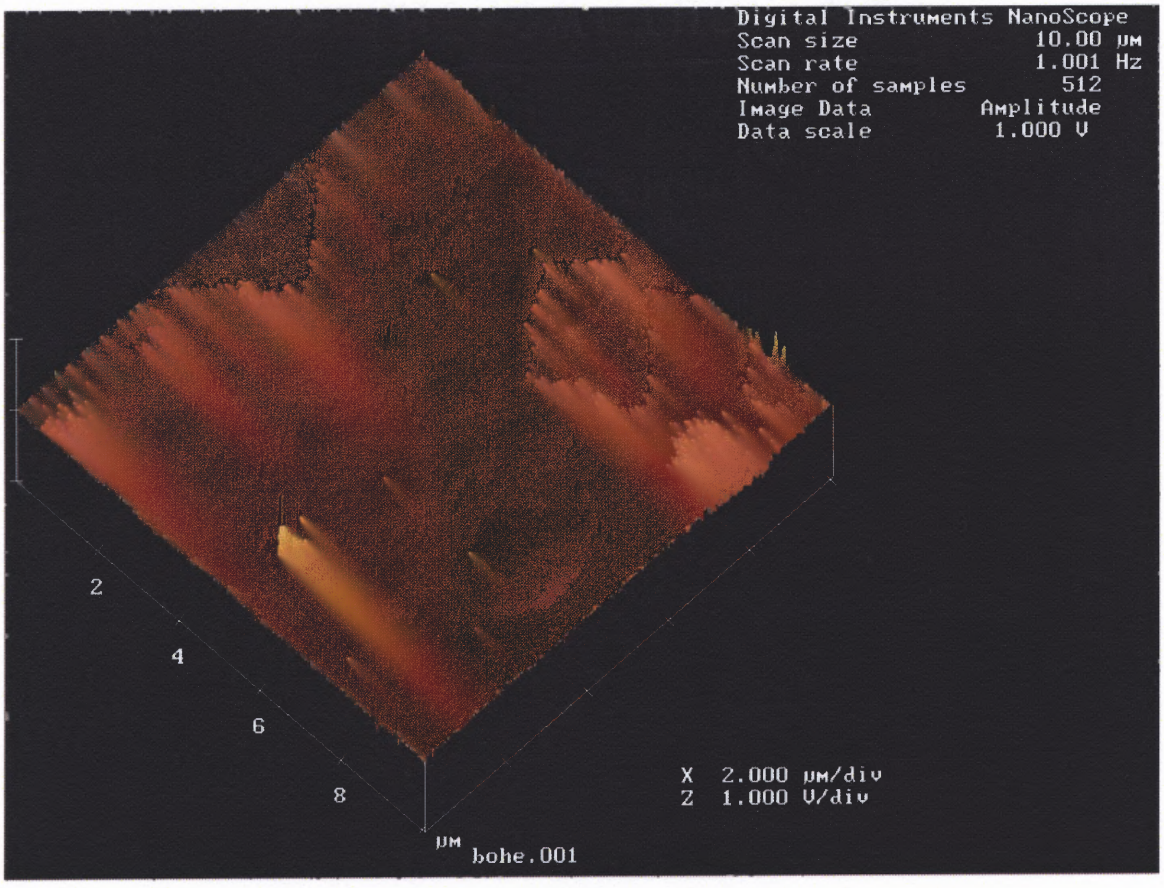

Figure 5.21 AFM picture of sample A surface after annealed at 400°C

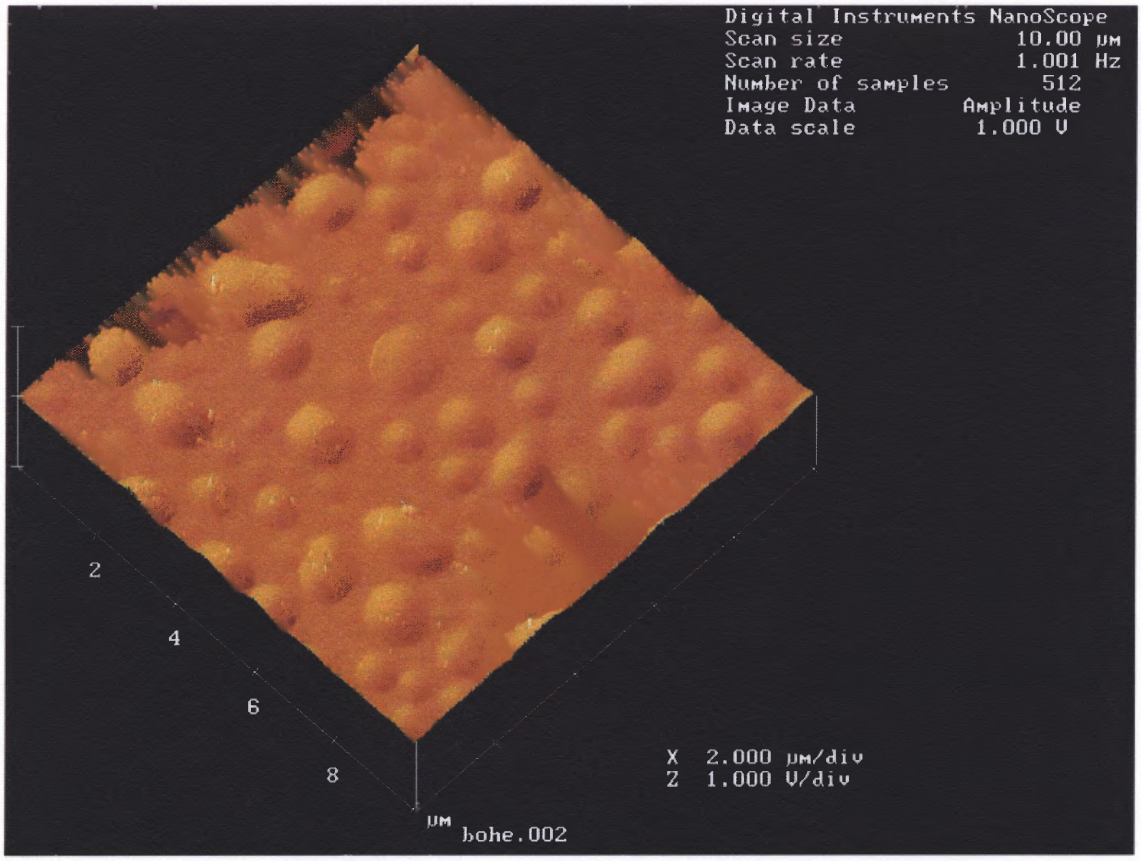

Figure 5.22 AFM picture of sample B surface after annealed at 400°C

Table 5.1 The area of H related absorption peak

Annealing Temp (°C)	He-PIII	PIII
Room temperature	2.43	1.97
100	2.15	1.61
230	2.12	1.58
400	1.06	0.72

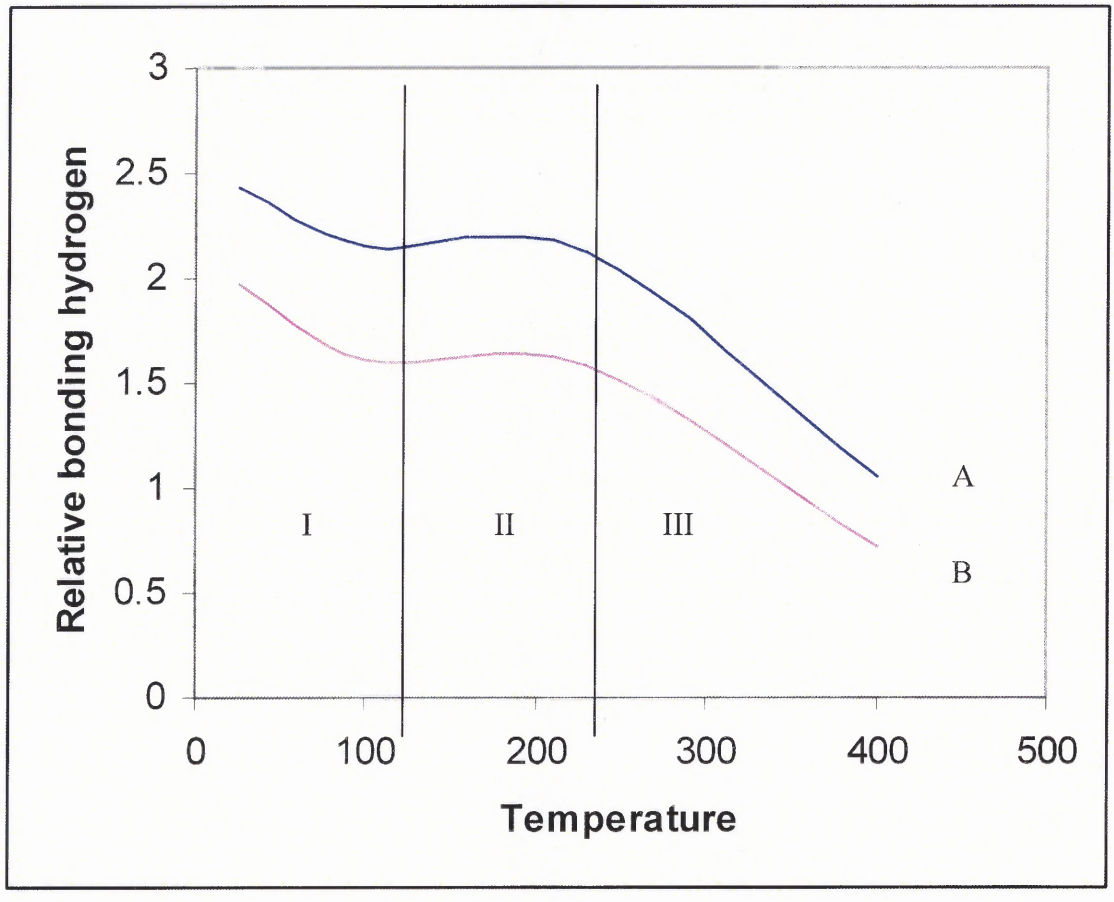

Figure 5.23 The total bonding hydrogen amount as a function of temperature

In above pictures, two overlapping infrared (IR) absorption at ~2000 and 2100 cm^{-1} due to different Si-H stretch mode vibrations are usually detected. The absorption band at ~2000 cm^{-1} was assigned to isolated Si-H bonded in an amorphous network. But attribution of 2100 cm^{-1} is more controversial. Based on an apparent correlation with IR absorption bands around 840 and 890 cm^{-1}, this absorption around 2100 cm^{-1} was originally attributed to $Si-H_2$ or $Si-H_3$ vibrations. However, this correlation is not always observed and it was later argued that a shift in vibrational frequency of 100 cm^{-1} was too large to be explained in this way, so it was suggested instead to be related to the local environment around the Si-H bonds. More specifically, a comparison of the 2100 cm^{-1}

absorption with that observed for Si-H on passivated surfaces led to attribution of this band to H bonded on internal surfaces or voids with Si structure.

From above discussion, we assigned ~2000 cm^{-1} to isolated Si-H bonded in an disorder network, 2100 cm^{-1} to H bonded on internal surface or voids in the Si lattice.

Reading the IR spectrum from our samples, we can find:

(1) In sample A, lots of hydrogen was bonded in the disorder structure and internal surface of voids.

(2) In sample B, main part of H was trapped in the internal surface of voids.

(3) Compared A and B, more hydrogen was trapped in the disorder structure in sample A than that in sample B. Nearly same amount of H was trapped by the internal surface of voids in sample A and B.

(4) As temperature increase, total bonding hydrogen decrease in sample A and B. From fig 5.23, we can find three temperature zones in the whole annealing range.

Zone I: room temperature~100 °C

Zone II: 100 °C~230 °C

Zone III: 230 °C~ >400 °C

In zone I and zone III, the bonding H decrease. In zone I, the desorption rate of sample A is more than sample B. However, in zone III, the desorption rate of sample B is more than that of sample A. In zone II, the total bonding H looks stable in sample A and sample B.

These results are very strange. From the implantation knowledge, the Ne implanted wafer should have more disorder structure than no-implanted wafer. After PIII processing, more hydrogen should be trapped in the disorder lattice in pre-implanted wafer. However, the results are opposite.

I think that lots of voids were generated in silicon wafer after He implantation. These voids can work as getterring sites for abstracting other small defects. In PIII processing, lots of small defects will move to internal voids and the volume of these voids will grow. H will be trapped in the internal surface of voids and form H molecules residing in these voids. AFM pictures show us that the bubbles of sample B are bigger than those of sample A when annealed at 400 °C. This result may give us a decision that more hydrogen gas formed in sample that that in sample B. this is reason why IR absorption band strength is weaker in sample B than in sample A.

In summary, silicon wafer contains lots of internal voids after Ne implantation. These voids will abstract small defects in H PIII processing. Compared with non-implantation samples, less hydrogen was trapped in the disorder structure and main hydrogen was trapped in the internal surface of the voids and H molecules in these voids. We may also postulate that lots of small defects will generate in normal H PIII processing. Inertial gas pre-implantation may help remove these small defects and get good quality transferred layer in the later layer exfoliation

CHAPTER 6

MECHANISM OF WAFER BONDING FOR SOI

6.1 Introduction

Silicon-on-silicon wafer bonding is an outgrowth of silicon-on-insulator technology. Silicon-on-silicon and silicon-on-insulator bonded substrates have significant performance and fabrication advantages over conventional bulk wafer processing for a wide variety of VLSI applications. Silicon-on-silicon wafer bonding is also referred to as direct wafer bonding.

Wafer direct bonding refers to the phenomenon that mirror-polished, flat and clean wafers, when brought into contact, bond to each other at room temperature without the use of adhesive or external force. Therefore wafer direct bonding technology is not prone to the introduction of stress and inhomogeneity in bonded pairs. Wafer direct bonding is also different from the popular anodic bonding that employs heating and electric fields and requires at least one of the bonding wafer to be a glass wafer or a wafer covered by a glass layer containing mobile ions.

Wafer direct bonding technology is essentially based on an understanding of the fundamental question of why broken pieces of any solid material usually can not be reversibly rejoined at room temperature in ambient even if the mating surfaces are perfectly complementary. It was understood that the main factors that prevent reversible rejoining appear to be the changes of the surface immediately after separation, including surface reconstruction, adsorption, oxidation, roughening and contamination that reduce the surface energy significantly, or prevent the surfaces from coming in close proximity.

Based on this understanding, wafer-bonding technology was introduced such that two wafers with surfaces that are sufficient smooth, flat and clean can bond to each other without any adhesive or external forces at room temperature in ambient forces.

6.2 Parameters that Influence Bonding Quality [89-90]

Parameters that mainly influence bond quality of bonded hydrophilic silicon wafers are generally recognized as: (i) surface cleanliness; (ii) saturated surface hydrophilic; (iii) surface roughness and non-flatness.

6.2.1 Surface Smoothness

Wafer direct bonding is based on intermolecular van der waals attraction forces between mating surfaces of the wafers. Macroscopically, all intermolecular forces are short-ranged forces; therefore sufficient surface smoothness is crucial for wafer bonding. The adequate level of smoothness of the mating surface depends on the surface bonding species that determine the distance over which the intermolecular forces are effective.

For mating surfaces that are terminated by non-polar molecular group, the attraction force is mainly a dispersion force resulting from the nonzero average value of the temporary dipole moment due to charge distribution fluctuation. The surface force F between two bodies decrease rapidly with distance t, e.g. with the inverse third power for flat plates

$$F \sim t^{-3} \tag{6-1}$$

For the dispersion force to be effective, the peak-valley distance of the surface roughness should be of the same order as the lattice constants of most materials, i.e. around 3-5.5A corresponding to the root mean square micro-roughness of ~0.5 A.

If polar groups, especially those with hydrogen atoms such as H-F, H-O, and H-N, terminate the bonding surfaces, a strong form of dipole-dipole attraction is present, termed hydrogen bonding. The bond energy of each hydrogen bond is typical about 10% of that of a covalent bond. In hydrogen bonding, the hydrogen atom in a surface polar molecule interacts with an electronegative atom, such as O, N and F, of an adjacent molecule on the mating surface.(Fig.6.1) Moreover, if excess polar molecular are present around mating surfaces, hydrogen bonding can be formed not only between the polar molecules and the surface polar groups but also between the polar molecules themselves. Fig 6.1 shows the bonding bridge formed by clusters of water molecules at the bonding interface between hydrophilic silicon wafers. For many polar molecules such as HOH or HF, a cluster of two or three polar molecules is energetically more favorable than two or three isolated molecules . The linkage of the polar molecules may form a bridge between two mating surfaces. In this way, a 'long range' intermolecular force can be realized and the requirement of surface smoothness for room temperature bonding is greatly eased. For surface terminated by OH, NH and FH, the root mean square micro-roughness can be up to ~5 A.

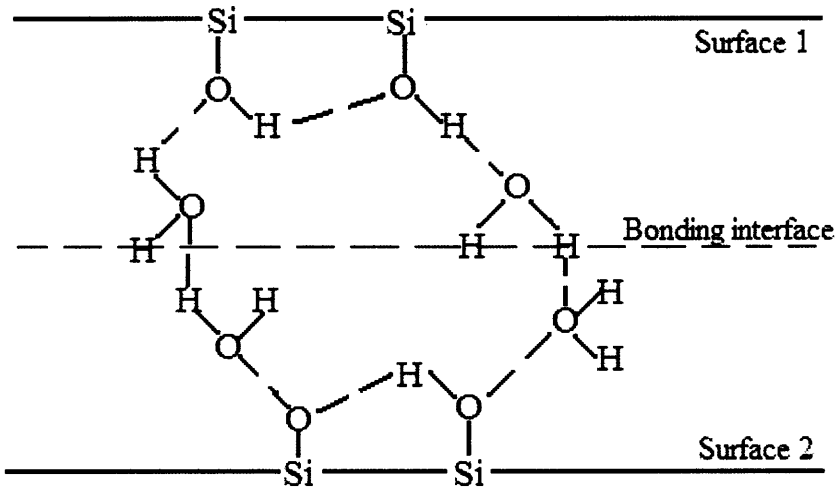

Figure 6.1 Schematic of water bonding bridge between two hydrophilic Si bonding wafer on associated Si-OH groups.

The microscopic surface smoothness of mating wafers provides the attraction force necessary for wafer bonding. When two wafers are bonded, the energy required to separated two bonding wafers can be expressed as the products of the number of the bonds formed on a unit area (bond density), n, and the energy of each bond Eb:

$$\gamma = \frac{nE_b}{2} \tag{6-2}$$

If the bonding wafers are identical, the total bonding energy is two times that of the specific surface energy of one of the bonded wafers. For convenience, the bonding energy is usually defined as the average specific surface energy γ of the two bonding surfaces when the bonded pair is partially separated by a separator such as a razor blade of thickness t_b as a schematically shown in Fig 6.2.

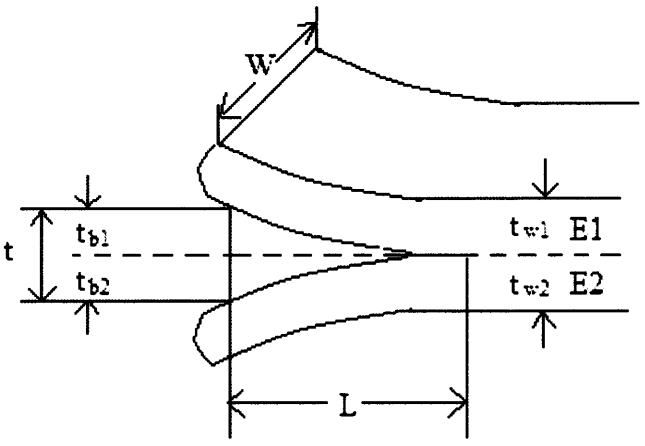

Figure 6.2 The average specific surface energy γ of a bonding surface when the bonded pair is partially separated by a separator such as a razor blade.

This method is based on the equilibrium between the elastic forces of the bent separated part of a pair and bonding forces at the crack tip. In the case of bonded pairs with identical wafers of thickness t_w and $E_1=E_2=E$ where E is Young's modulus, the bonding energy γ can be obtained from the equilibrium crack length :

$$\gamma = \frac{3Et_{w1}^3 t_b^2}{32L^4} \tag{6-3}$$

For bonded pairs of wafers of different thickness t_{w1} and t_{w2} and/or elastic properties E_1 and E_2, the sum of the two surface energies γ_1 and γ_2 on the two partially separated surfaces becomes:

$$\gamma_1 + \gamma_2 = \frac{3t_b^2 E_1 t_{w1}^3 E_2 t_{w2}^3}{8L^4 (E_1 t_{w1}^3 + E_2 t_{w2}^3)} \tag{6-4}$$

When one wafer of a bonded pair is much thinner than the other wafer of the same material, $t_{w2} >> t_{w1}$ and $E_1=E_2=E$, the surface energy is expressed as

$$\gamma = \frac{3Et_{w1}^3 t_b^2}{16L^4} \tag{6-5}$$

Since only molecules that are in sufficient proximity can form bonds between each other, the number of bonds is determined by the smoothness of the contacting surfaces. If mating surfaces are sufficiently smooth, a large bonding energy will result from higher bond density on the surfaces and the higher energy of each bond formed across the two surfaces.

6.2.2 Surface Flatness

However, the wafer surfaces are never perfectly flat. The macroscopic flatness non-uniformity or waviness of the wafer surfaces leads to a gap generation at the interface when two such surfaces are brought into contact. According to the theory of small elastic deflection of a thin plate, if the bonding energy γ is sufficiently high, the gaps with the height 2h and extension 2R (Fig. 6.3) caused by waviness of the bonding surfaces can be closed by elastic deformation of the two wafers. Assuming bonding of two identical wafers with thickness tw, for $R>2t_w$ (Fig6.3(a)) the bonding energy γ required to close the gaps is given by:

$$\gamma > \frac{2E' t_w^3 h^2}{3R^4} \qquad (6\text{-}6)$$

where E' is given by $E/(1-\nu^2)$ with E being Young's modulus and ν Poison's ratio.

For $R<2t_w$ (Fig. 6-3 (b)), the condition for gap closing is independent of wafer thickness and is given by:

$$\gamma > \frac{h^2 E'}{12.25R} \qquad (6\text{-}7)$$

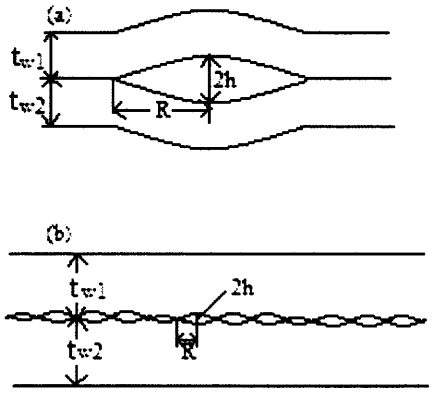

Figure 6.3 Schematic of gaps between wafers for (a) $R>2t_w$ and (b) $R<2t_w$.

The closure of gaps results in a gain in bonding energy because new bonds at the newly closed interface can develop and the elastic energy resulting from deformation is usually smaller than the increased bonding energy of the newly formed bonds.

From equation (6-6), it is clear that large bonding energy, long gap extension and small thickness of wafers can significantly enhance the bondability. Wafer bonding can greatly benefit from the improved wafer surface finishing and advanced CMP (chemical mechanical polish) technology routinely employed in VLSI fabrication.

6.2.3 Surface cleanliness

As discussed above and according to equation (6-2), in order to achieve a successful bonding, the mating surfaces must be sufficiently clean and terminated only with desired bonding species that are maximized in density. In other words, surface contaminants can significantly reduce the surface reactivity and lower the bonding energy.

Moreover, trapped interface particles can result in bubbles many orders of magnitude larger than the particles. A particle with a diameter of 2h can form an unbonded interface or bubble with a diameter of 2R for $R>2t_w$:

$$R = \left(\frac{0.67 E' t_w^3}{\gamma} \right)^{1/4} h^{1/2} \qquad (6\text{-}8)$$

A particle of about 1μm diameter leads to a bubble with a diameter about 5000 times larger (0.5cm) for typical 4-in diameter Si wafers with a thickness of 525μm.

The trapped contaminants at the bonding interface are also the main cause of the interface bubbles that are generated during subsequent annealing after bonding. It has been found that hydrocarbons at the mating surfaces act as the nucleation sites for interface bubbles and hydrogen is the main components of the bubbles in Si/Si bonded pairs.

6.3 Bonding Process

The whole bonding processes were with <100>, 4 inch diameter, 525 μm thickness, hydrogenated wafer, and with <100>, 4 inch diameter, ~500 nm oxidized, Si substrate. In order to bond wafer successfully, special attention has to be paid at the following three fundamental steps:

(1) Surface preparation to obtain clean and hydrophilic surface;

(2) Pre-bonding at room temperature in air to join and accommodate two surfaces;

(3) Bond annealing (strengthening) at elevated temperature in different ambient to obtain covalent siloxane bonds between two wafers.

6.3.1 Pre-join Surface Preparation

Cleaning of the silicon surface has a great impact on surface chemistry and topography. Three types of clean process are used in this chapter, those are (1) RCA clean; (2) Plasma active, then RCA clean; (3) Nitric Acid Active.

6.3.1.1 RCA Clean

The RCA cleaning technique does not attack silicon, and only a very thin layer of silicon dioxide is removed in the process. The procedure was also designed to prevent relating of metal contaminants from solution back to the wafer's surface. When finished, the polished side should be specula with no residue.

1. Solution preparation:

Each will be prepared made in 1000 ml polypropylene beakers.

A. Organic clean solution of $DIH_2O:NH_4OH:H_2O_2$ (5:1:1)

*** Always add reactive compounds(acid/base) to water ***

a.) 625mL DIH_2O

b.) 125mL NH_4OH

c.) 125mL H_2O_2

Stir solution with clean teflon rod. Place beaker into the temperature-controlled water bath and adjust the power to maintain the solution at 75 °C.

B. Oxide strip solution of DIH_2O:HF (50:1)

This solution will be prepared. Simply transfer the solution from the bottle to the 1000 ml beaker and place in water bath maintained at 25 °C.

C. Ionic clean solution of DIH_2O:HCl: H_2O_2 (6:1:1)

*** Always add reactive compounds(acid/base) to water ***

a.) 690mL of DIH_2O

b.) 115mL of HCl

c.) 115mL of H_2O_2

Stir solution with clean teflon rod. Place beaker into the temperature-controlled water bath and adjust the power to maintain the solution at 75 °C.

D. Fill a 1000 ml beaker with DI water for rinsing.

2. Procedure:

1. Place wafer(s) on teflon carriers.
2. Submerge the carrier with wafer in the Organic Clean solution for 10 minutes.
3. Remove carrier from the bath and rinse wafer in the DI water beaker for 1 minute.
4. Submerge the carrier with wafer in the Oxide Strip solution for 15 seconds.

5. Remove carrier from the bath and rinse wafer in the DI water beaker for 1 minute.
6. Submerge the carrier with wafer in the Ionic Clean solution for 10 minutes.
7. Remove carrier from the bath and rinse wafer in the DI water beaker for 1 minute.
8. Remove carrier from the DI water beaker and blow dry with nitrogen.
9. Take wafer to next processing step or place in a carrier box.

6.3.1.2 Plasma Active

All wafers were processed by oxygen or argon plasma under 300 mTorr pressure and 50 W. Then these wafers were clean by RCA procedure.

6.3.1.3 Nitric Acid Process

To mitigate the surface roughening occurring during RCA standard cleaning(SC1) treatment, diluted SC1 was used as described in table 6-1. In this stage, a trade-off between cleaning efficiency and surface roughing has to be achieved. As it can be seen from table 6-1, modified RCA cleaning was followed by oxide removal in diluted HF to expose silicon surface and rinse in deionized (DI) water.

At this point, dry wafers were immersed into hot nitric acid at 70 or 110 °C, allowing growth of few monolayers of fresh hydrous chemical oxide. After prolonged DI water rinsing, wafers were dried with nitrogen.

Table 6.1 Modified RCA preparation of silicon wafers

RCA cleaning – modified at 70 °C, 10 min
SC1 – (0.25 NH_4OH: 1 H_2O_2 : 5 H_2O)
DI, 10 min
HF:H2O 1:100 at 25 °C, 5 min
DI, 10 min
HNO_3 at 70 °C or 110 °C, 15 min
DI, 30 min

6.3.2 Pre-bonding

Pre-bonding step has to follow immediately after surface preparation. Two wafers were put into intimate contact by use of Teflon carrier and at room temperature. It was found important to initiate bonding in the center by locally pressing the center region from the top, thus enabling bonding phenomenon to propagate radically. The aim of this operation is to squeeze out the air trapping at the bond interface.

It is known that effective bond area and consequently bonding energy can be increased by applying external static pressure that increase the surface energy. By doing this, EV501 wafer boner was used. The EV501 bonding station was shown in Fig 6.4.

Figure 6.4 Photo of EV501 bonding station.

6.3.3 Bond Wafer Annealing

The final step in low-temperature bonding is bond annealing, when transformation of silanol to strong siloxane bonds takes place at elevated temperature. Bond strengthening was performed at different temperatures in the range of 80 °C to 1100 °C, and in different ambient.

6.3.4 Bond Quality Characterization

To determine the size and density of voids or bubbles, IR transmission investigation was performed by setup with homemade IR camera, as shown in Fig.6.5. Results will be discussed below.

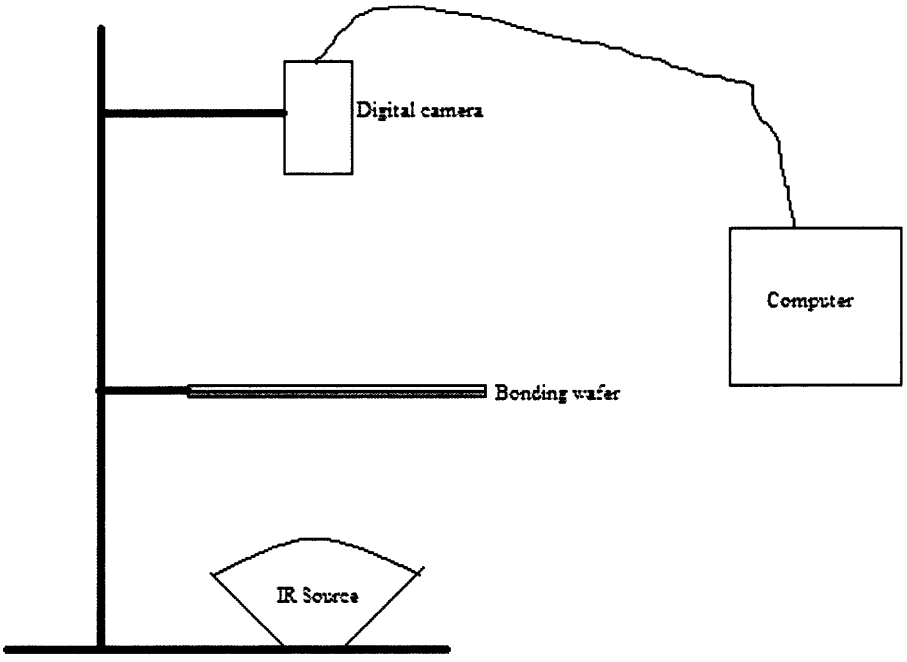

Figure 6.5 Setup for bond characterization by IR transmission method applied in our work.

6.4 Experiments Results

6.4.1 IR Pictures of the Bonding Wafer via Plasma Active

IR pictures show that bonding quality is well at room temperature except for the edge area of the wafer. As temperature increased from room temperature to ~1000 °C, no big difference can be observed in these pictures.

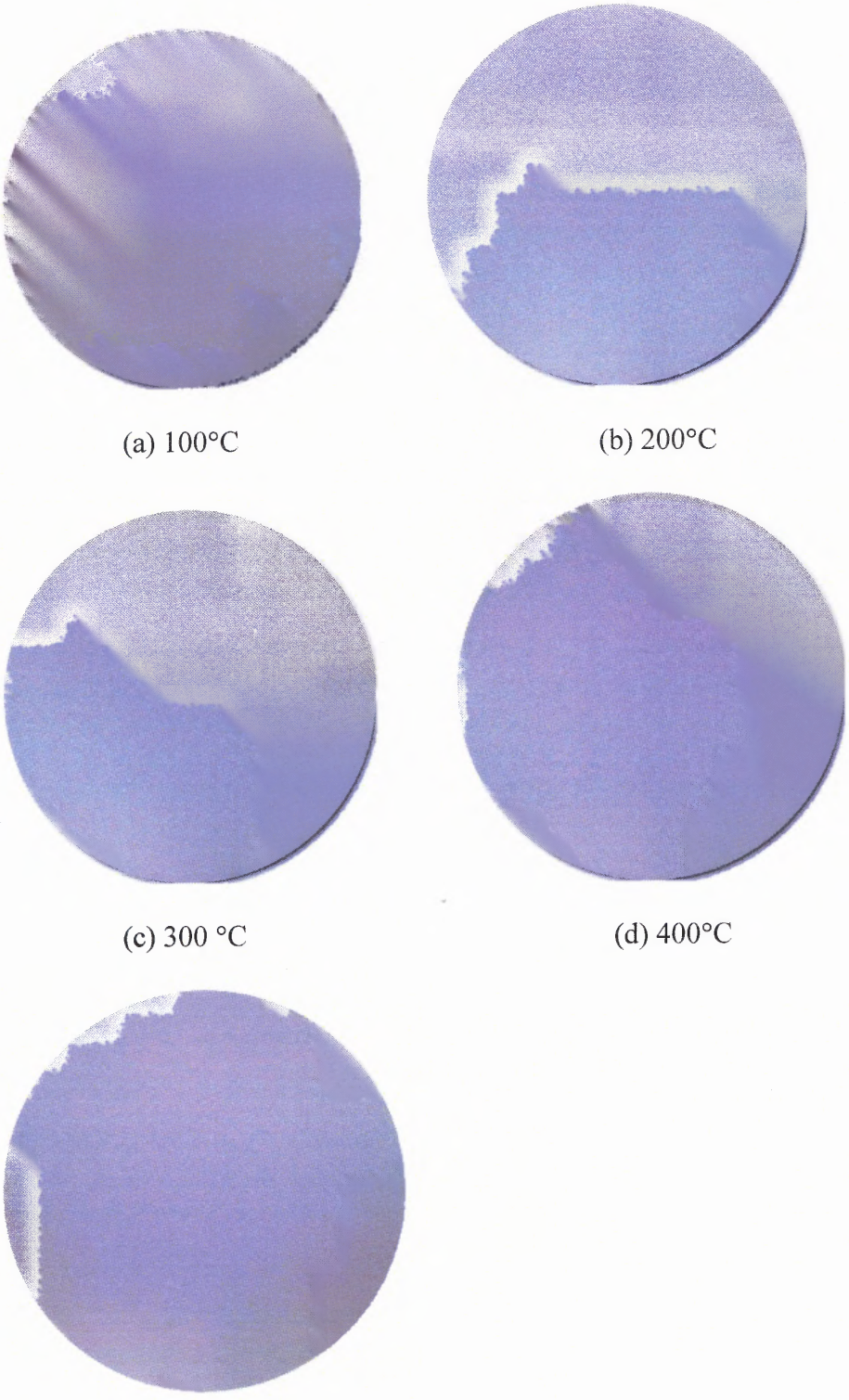

(a) 100°C (b) 200°C

(c) 300 °C (d) 400°C

(e) 1050 °C

Figure 6.6 IR pictures of the bonding wafer via plasma active, annealed from room temperature to 400 °C.

6.4.2 IR Pictures of Bonding Wafer via RCA Clean

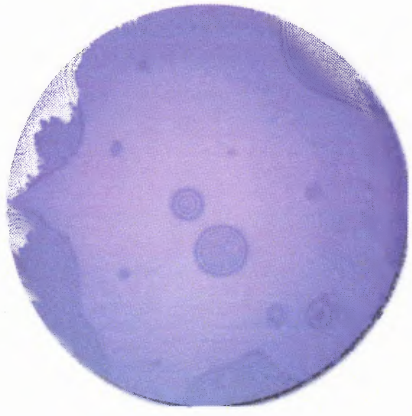

(a) room temperature

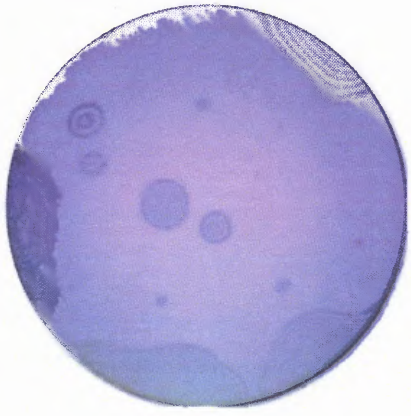

(b)100°C

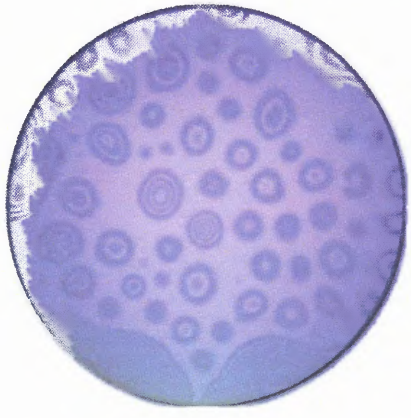

(c) 200°C

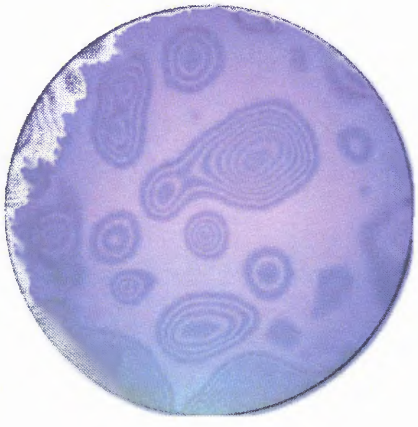

(d) 300°C

(e) 400°C

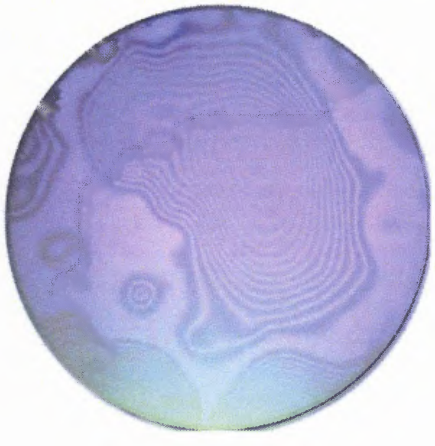

(f) 1000°C

Figure 6.7 IR pictures of bonding wafer via RCA clean, annealed from room temperature to 1000 °C.

From these pictures, we can find that some voids exist at the bonding interface at room temperature. When temperature arrives at 200 °C, lots of voids appear. The size of these voids will increase and form a continuous area when temperature increase. This unbond region cannot decrease even though the wafer was annealed to 1050 °C.

6.4.3 IR Pictures of Bonding Wafer by Nitric Acid Active

From the IR pictures, we found that a few voids exist in the bonding interface. When the temperature increase to 350 °C, some small spots appear. But when the wafer is annealed to 1050 °C, these spots disappear. Only the original voids were left.

(a) room temperature

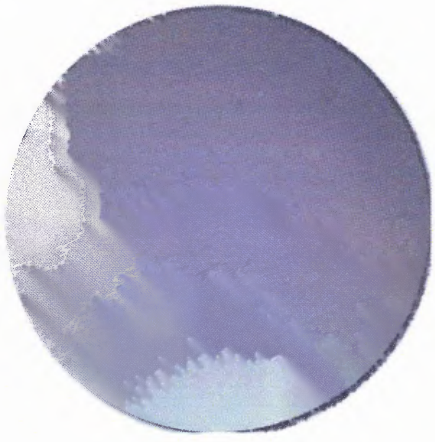

(b)100°C

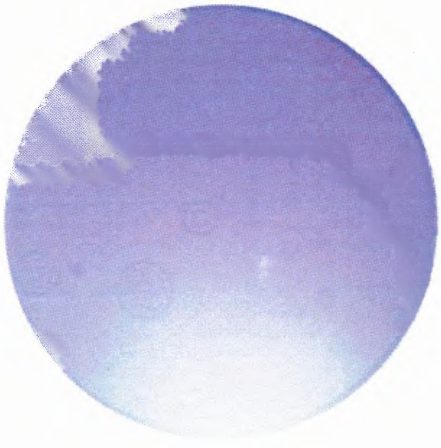

(c) 250°C

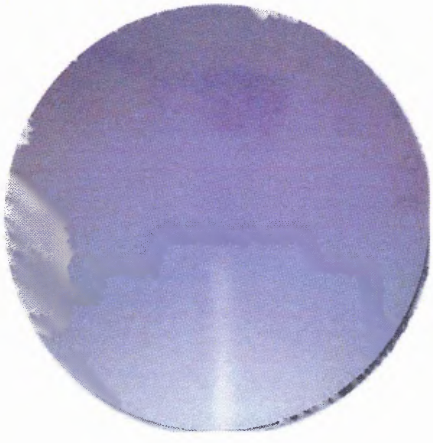

(d) 350°C

(e) 450°C

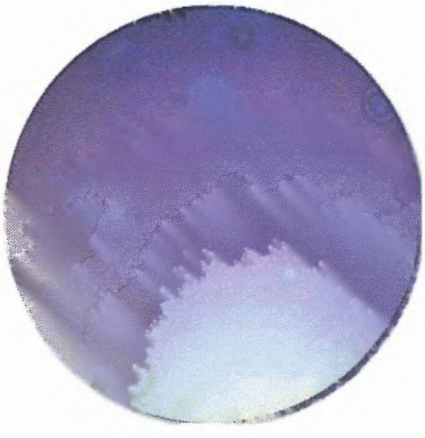

(f) 1050°C

Figure 6.8 IR pictures of bonding wafer by Nitric acid active, annealed from room temperature to 1050 °C.

6.5 Discussion

Methods that are commonly utilized to inspect this kind of macroscopic failures are IR transmission image, X-ray topography and ultrasound microscopy. Infrared transmission imaging method is most often used to study the voids or imperfections at the bonding interface and was employed also in this study. The origins of voids can be: (i) particles left on the surface after cleaning; (ii) locally increased microroughness due to poor polishing; or (iii) trapped gases at the interface.

For the RCA clean only active bonding wafers, it is found that when the bonding wafer is annealed to 200 °C, lots of small voids will appear. We suppose that these voids were induced from the water and left gas after two wafers were bonded. The following reactions may show these procedures.

$$Si - OH + HO - Si \leftrightarrow Si - O - Si + H_2O \qquad (6\text{-}1)$$

$$Si + 2H_2O \rightarrow SiO_2 + 2H_2 \qquad (6\text{-}2)$$

If interface water is successful removed from interface via out-diffusion, what is less probable, or time- and temperature-dependent dissociation takes place, then strong siloxane bonds are formed. Interfacial species must either react at the interface or dissolve into the oxide and bulk in order to allow the oxides to mate tightly. If water is trapped at the interface, bubbles are formed as described by several authors[91-92]. For unbonded part of the area, a term bubble or void is normally used. Water within bubbles can play a role at elevated temperatures via enhanced dissociation process thus releasing pressure that makes the bubbles to finally disappear. However, they simultaneously generate from other reasons, possible sources being hydrogen from dissociation process

(Eq. 6-2) or vaporized hydrocarbon (CHx). Plasma active or hot nitric acid active may be a good way to remove these voids.

During the last 10 years, many models were proposed by different authors[93,94]. The model recently proposed by Tong and Goesele [95] offers a very concise and consistent into bonding mechanism and it is primarily based on the fact that surfaces brought together are originally prepared hydrophilic, i.e., covered with silanol groups which act as adsorption sites for water molecules. It is now widely accepted that silicon surface hydrophilicity, caused by hydroxyl groups and physisorbed water, plays a major role in the process of bonding two silicon interfaces. Hydrophilic nature of the silicon surface can be obtained either by oxygen plasma activation or by wet oxidizing agents (nitric acid, SC1 cleaning solution)

With dry plasma treatment, the desorption of undesired adsorptives and the activation of free sites for the adsorption of OH groups is achieved simultaneously. Treatment in plasma results in fully hydrated surface and exhibits long-term stability of hydrophilic surface nature.

Wet oxidizing treatment of clean hydrophobic silicon surface in hot HNO_3 renders not only the growth of strained native oxide with sufficient density of attached silanol groups, but also removes CH adsorbed species from the surface. Hattori et al.[96] showed that the structure of this oxide can be characterized by the distribution of Si^{3+} suboxide and that the correlation to Si-H bonds can be established. This correlation explains that enhanced formation rate of native oxide in nitric acid is due to increased mobility of oxidizing species through present Si-H network. Distribution of Si^{3+} is uniform in contrast to other hydropylization chemicals, which result in a piled up distribution at the

interface. This was also also confirmed by Jiao et al. [97], who reported that beside sufficient Si-OH also Si-H surface terminations are found simultaneously on the surface. Aoyama et al. [98] have showed by selective etching with photoexcited fluoide and by STM observations that SiO_2 formed in HNO_3 or SC_1 is not a uniformly thick layer, but has rather an island structure, with some islands connected mutually together, thereby confirming the existence of both Si-OH and Si-H surface termination appearing simultaneously.

6.6 Summary and Conclusions

Silicon-on-insulator bonding is an operation for ultra-fine alignment, joining and thermal bonding of two wafers, namely 'handle' and 'device' substrates. Prior to the joining step, both wafer substrates are ultra-clean. Each pre-join silicon wafer surface is 'hydrophilic'. The thermal annealing operation is performed using a 'wet' oxidation step at elevated temperatures. The effectiveness of bonding is dependent upon the degree of hydrophilic ability as well as surface flatness. The equality of the interface layer within a bonded pair is evaluated in terms of density of voided or disbonded regions as well as electrical yield. The density of micro-voids within an interface layer is directly dependent on light point defect density of the pre-join substrates. It is found that lots of voids can be generated in bonding wafers by only RCA clean active, annealed to >200 °C, and these voids can not disappear until annealed to 1050 °C. We suppose these voids were induced from dissociated H_2 from water and evaporated CH_x. Plasma active and hot nitric acid active for direct wafer bonding may be a good choice for SOI fabrication.

CHAPTER 7

SUMMARY AND CONCLUSIONS

In our Tegal-100 plasma system, we can find the sheath bias range is from 0~1000 V if the maximum power is 300 W. The sheath potential will increase as the power increase, and decrease as ions concentration increase. In the pulsed PIII mode, if the voltage V_0 applied to the sample stage is less than the dc threshold voltage V_{DC}, the sheath will never hit the chamber wall regardless of the pulse duration. Even though the pulse voltage is higher than V_{DC}, the plasma may not extinguish if the pulse is turn off before the sheath edge dynamically propagates to the chamber wall where the RF source is. In our PIII system, the chamber distance is ~1 m, so the maximum voltage is ~30 KV, the effective pulse duration is ~0.0001s.

Silicon wafers are implanted by different elements (He, N, Ne, Ar) at appropriate energy. A H trapping layer will be formed in the depth of ~100 nm from TRIM calculation. Two different types of trapping layer are formed, one is vacancy cluster, and the other is gas bubble.

In this trap layer, there are many vacancies, interstitials and micro-voids. Due to the presence in the plasma of molecular and atomic hydrogen and extremely strong acids H_3^+ and H_2^+, the surface of Si wafer can be modified by H^+, H_2^+, H_3^+ in H-plasma. Hydrogen species damage the surface strained Si-Si bonds, H_2 can readily dissociate, bind to the surface and diffuse into the Si bulk at low temperature (150~200 °C). At higher temperature (300~350°C), the trapped in silane-like species will be detrapped, and H atoms will diffuse deeper into Si bulk. When these atoms meet the buried disorder layer

and bubbles, they will form another Si-H structure and Hydrogen molecular accumulated in the interstitial voids.

In plasma-ion-immersion-implantation processing, compared with non-implantation samples, less hydrogen was trapped in the disorder structure and main hydrogen was trapped in the internal surface of the voids and H molecules in these voids in He-implanted sample. We may also postulate that lots of small defects will be generated in normal H PIII processing. Inertial gas pre-implantation may help remove these small defects and get good quality transferred layer in the later layer exfoliation

It is found that lots of voids can be generated in bonding wafers by only RCA clean active, annealed to >200 °, and these voids can not disappear until annealed to 1050 °C. We suppose these voids were induced from dissociated H_2 from water and evaporated CH_x. Plasma active and hot nitric acid active for direct wafer bonding may be a good choice for SOI fabrication.

REFERENCES

1. G G Shahidi (2002), "SOI technology for the GHz", IBM J. Res. & Dev. 46, 121.

2. Makoto Yoshimi(2002), "Current status and future directions of SOI technology", Solid-State Electronics, 46, 951-958.

3. G. Shahidi, A. Ajmera, F. Assaderaghi, R. Bolam, A. Bryant, M. Coffey, H. Hovel, J. Lasky, E. Leobandung, H-S Lo, M. Maloney, D. Moy, W. Rausch, D. Sadana, D. Schepis, M. Sherony, J. W. Sleight, L. F. Wagner, K. Wu, B. Davari, T.C. Chen (1999). Mainstreaming of the SOI Technology. in Proceedings of 1999 Int. SOI Conference, Oct.4-7, Rohnert Park, CA, 1-4.

4. R. DeJule (1999), .SOI Comes of Age. Semiconductor International, Nov. 67-74.

5. K.Izumi, M.Doken, H.Ariyoshi (1978), CMOS Devices Fabricated on Buried SiO_2 Layers Formed by Oxygen Implantation into Silicon, Electronics Letters, 14, 593-594.

6. The International Technology Roadmap for Semiconductors, 2003 edition , http://public.itrs.net/Files/2003ITRS/Home2003.htm.

7. M.Zvanut, R.Stahlbush (1999), Comparison of Trapped Hole Characteristics in Buried Oxides., in Proceedings of the 9th Int. Symp. On Silicon-on-Insulator Technology and Devices, Electrochemical Society, 99(3), 195-200.

8. Takashi Ogawa (2001), Solid state Technology, 2, 16-19.

9. T. Yonehara, K Sakaguchi, N Sato (1994), Appl. Phys. Lett. 64, 2108-2010.

10. T. Yonehara, K. Sakaguchi, N Sato (1999), Proc. 9th Int. Symp. On Silicon-on-Insulator Tech. And Devices, USA, 111-114.

11. M. Bruel (1994), .Process for the production of thin semiconductor material films. US Patent 5,374,564.

12. B. Aspar, C. Lagahe, H. Moriceau, E. Jalaguier, A. Mas, O. Rayssac, M. Bruel - A.J. Auberton-Herve (1999), T. Barge, and F. Letertre The Smart Cut® Process: Status and New Developments. In: Semiconductor Wafer Bonding: Science, Technology, and Applications, Proceedings of Fifth International Symposium on Semiconductor Wafer Bonding: Science, Technology and Applications - Honolulu, Hawaii ed. by V. C. E. Hunt, H. Baumgart, and U. Goesele, PV 99-35.

13. S. Cristoloveanu (1999), .SOI: A metamorphosis of silicon. IEEE Circuits and Devices Magazine. 15, 26-32.

14. A.Auberton-Herve (1999), .Smart-Cut. Technology: Industrial Status of SOI Wafer Production and New Material Development., Proceedings of the 9th Int. Symp. On Silicon-on-Insulator Technology and Devices, Electrochemical Society, 99-3, 93-106.

15. U. Gosele, Q. Y. Tong (1998), Semiconductor Wafer Bonding: Science & Technology, Wiley, 288.

16 P. K. Chu and X. C. Zeng (2001), Hydrogen Induced Surface Blistering of Sample Chuck Materials in Hydrogen Plasma Immersion Ion Implantation, Journal of Vacuum Science & Technology A,19(5), 2301 – 2306.

17. Z. N. Fan, X. C. Zeng, D. T. K. Kwok, and P. K. Chu (2000), Surface Hydrogen Incorporation and Profile Broadening Caused by Sheath Expansion in Hydrogen Plasma Immersion Ion Implantation, IEEE Transactions on Plasma Science, 28(2), 371- 375.

18. P. K. Chu (2002), Contamination Issues in Hydrogen Plasma Immersion Ion Implantation of Silicon – A Brief Revie, Surface & Coatings Technology, 156, 244 – 252.

19. L. W. Wang, R. K. Y. Fu, X. C. Zeng, P. K. Chu, W. Y. Cheung, and S. P. Wong (2001), Damage in Hydrogen Plasma Implanted Silicon, Journal of Applied Physics, 90(4) 1735 – 1739.

20. W. G. En, I. J. Malik, M. A Bryan, S. Farrens, F. J. Henley, N. W. Cheung, C. Chan (1998), .Genesis process.: A new SOI wafer fabrication method. IEEE International SOI Conference Oct 5-8 1998, 163-164.

21. Alexander Y. Usenko, Alexander G. Ulyashin, Thinner SOI Using Plasma Hydrogenation (2002), Japanese Journal of Applied Physics, 41, 5021-5023.

22. A.Y. Usenko, W.N. Carr, and B. Chen (2002), Plasma Hydrogenation Of A Buried Trap Layer In Silicon: Formation Of A Platelet Layer, in: PV 2002-17 Plasma Processing XIV, ed. by G. S. Mathad, M. Yang, R. E. Sah, and M. D. Allendorf, presented at 201st Meeting of Electrochemical Society, Philadelphia, PA, May 12-17, 2002, The Electrochemical Society, Pennington, NJ, 50-60.

23. A.Y. Usenko, W.N. Carr, B. Chen, Layer Transfer Process for SOI with Improved Manufacturability, Abstracts of International Conference on Alternative Substrate Technologies, Cancun, Mexico, September 15-19, 2002.

24. A.Y. Usenko, W.N. Carr, B. Chen, Y. Chabal (2002), "Alternative Smart-cut-like Process for Ultra-thin SOI Fabrication" Proceedings of the 13th Annual IEEE/SEMI Advanced Semiconductor Manufacturing Conference and Workshop ASMC 2002 - April 30 - May 2, 2002 at the Seaport Hotel, Boston, Massachusetts, USA, 6-11.

25. A.Y. Usenko, W.N. Carr, B. Chen (2002), Hydrogen Platelet Layer In Silicon Formed From Hydrogen Trapped Onto Microbubbles Of Gases Materials Research Society Symposium Proceeding 719E, 2002, F9.6.1-F9.6.6.

26. A.Y.Usenko, W.N. Carr (2001), Blistering on Silicon Surface Caused by Gettering of Hydrogen on Post-Implantation Defects, Materials Research Society Symposium Proceeding 681E, I3.3.1-I3.3.6.

27. A.Y. Usenko, and W.N. Carr (2001), Electrolytic Hydrogenation Of Buried Preamorphized Layer In Silicon For SOI Wafer Process, Silicon-on-Insulator Technology and Devices *X*, ed. by S. Cristoloveanu, P. L. F. Hemment, K. Izumi, G. K. Celler, F. Assaderaghi, Y.-W. Kim, PV 2001-3.

28. A.Y.Usenko, W.N. Carr (2000), Hydrogenation of Trap Layer as an SOI Process Step, Proceedings of 2000 IEEE SOI Conference, Wakefield, MA, 16-17.

29. A.Y. Usenko, W.N. Carr, B. Chen(2002), Crystal Fracture Induced By Decorating Of Post-Implantation Defects: Silicon Layer Delaminating, 14th International Conference on Ion Implantation Technology, IIT 2002 September 22-27, 2002, Taos, New Mexico, USA.

30. A. Grob, P. Rohr, G. mariani, J. Sevely, J. J. Grob (1996), Kinetics of impurity gettering on buried defects created by MeV argon implantation, Nucl. Instr. And Meth. In Phys. Res. B 112,169-172.

31. Martin D. Giles (1993), Transient phosphorus diffusion from silicon and argon implantation damage, Appl. Phys. Lett 62(16), 1940-1942.

32. T. E. Seidel, R. L. Meek and A. G. Cullis (1975), Direct comparison of ion-damage gettering and phosphorus-diffusion gettering of Au in Si, J. Appl. Phys. 46, 600-607.

33. Valery A. Godyak, Natalia Sternberg (1990), Daynamic model of the electrode sheaths in symmetrically driven rf discharges, Physical Review A, 42(4), 2299-2311.

34. Mark A. Sobolewski (1999), Experimental test of models of high-plasma-density, radio-frequency sheaths, Physical Review E, 59(1), 1059-1071.

35. Michael A. Liberman (1988), Analytical solution for Capacitive RF sheath, IEEE Transactions on plasma science, 16(6), 638-644.

36.E. Neyts, M. Yan, A. Bogaerts, R. Gijbels (2003), Particle-in-cell/Monte Carlo simulations of a low-pressure capacitively coupled radio-frequency discharge: Effect of adding H2 to an Ar discharge, J. Appl. Phys. 93(9), 5025-5033.

37. Z. L. Dai, Y. N. Wang, T. C. Ma (2002), Spatiotemporal characteristics of the collisionless sheath and the ion energy distributions arriving at rf-biased electrodes, Physical Review E, 65, 036403.

38. Theodoros Panagopoulos, Demetre J Economou (1999), Plasma sheath model and ion energy distribution for all frequencies, J Appl. Phys. 85(7), 8979-8988.

39. Deepak Bose, T. R. Govindan, M. Meyyappan (2001), Semianalytical ion current model for radio-frequency driven collisionless sheaths, J Appl Phys. 89(11), 5932-5938.

40. Mark A. Sobolewski (2000), Sheath model for radio-frequency-biased, high-density plasmas valid for all ω/ωI, Physical review E, 62(6), 8540-8553.

41. Deepak Bose, T. R. Govindan, M. Meyyappan (2000), Ion dynamics model for collisionless radio frequency sheaths, J Appl Phys. 87(10), 7176-7184.

42. N. Xiang, F. L. Waelbroeck (2003), Effects of presheath dynamics on radio-frequency sheaths, J Appl Phys. 93(9), 5034-5042.

43. F. L. Waelbroeck (2002), Analytic solution for low-frequency rf sheaths in pulsed discharges, Physical review E 65, 066407-1~-11.

44. Andre Anders (2000), Handbook of Plasma Immersion Implantation and Deposition, ISBN 0-471-24698-0, John Wiley & Sons, Inc. 343-377.

45. Paul K. Chu (1998), Instrumental and Process considerations for the Fabrication of Silicon-on-Insulator (SOI) Structures by Plasma Immersion Ion Implantation, IEEE Transaction on Plasma Science, 26(1), 79-84.

46. Zhi-Neng Fan, Qing-Chuan Chen, Paul K. Chu, Chung Chan (1998), Low Pressure Plasma Immersion Ion Implantation of Silicon, IEEE Transactions on Plasma Science, 26(6), 1661-1668.

47. J.I. Goldstein, D.E. Newbury, P. Echlin, D.C. Joy, C. Fiori and E. Lifshin (1981), Scanning Electron Microscopy and X-Ray Microanalysis, Plenum Press, New York, London, 1981, chapt. 4.2.5.

48. M.H. Loretto (1984), Electron beam analysis of Materials, Chapman and Hall, London, New York, 1984, chapt. 3.

49. E. Chason, S. T. Picraux etc (1997), Ion beams in silicon processing and characterization, J. Appl. Phys. 81(10), 6513-6561.

50. O. W. Holland, S. J. Pennycook, Gerald L. Albert (1989), New Model for damage accumulation in Si during self-ion irradiation, Appl. Phys. Lett. 55(24), 2503-2505.

51. F. Uesugi, Y. Kikuchi, K. Watanabe, I. Hoshimoto (1998), Residual defects in low energy and low dose antimony ion-implanted silicon, J. Appl. Phys., 83(10), 5159-5163.

52. T. Motooka, O. W. Holland (1992), Amorphization processes in ion implanted Si: ion species effects, Appl. Phys. Lett. 61(25), 3005-3007.

53. P. K. Giri, S. Tripurasundary etc (2001), Crystalline to amorphous transition and band structure evolution in ion-damaged silicon studied by spectroscopic ellipsometry, J. Appl. Phys. 90(2), 659-669.

54. T. Motooka (1998), The role of defects during amorphization and crystallization processes in ion implanted Si, Materials Science and Engineering A 253, 42-49
55. T. Motooka, O. W. Holland (1991), Amorphization processes in self-ion-implanted Si: Dose dependence, Appl Phys. Lett. 58(21), 2360-2362.

56. O. W. Holland, S. J. Pennycook, Gerald L. Albert (1989), New model for damage accumulation in Si during self-ion irradiation, Appl. Phys. Lett. 55(24), 2503-2505.

57. O. W. Holland, J. D. Budai, D. W. White (1990), Uniaxial lattice expansion of self-ion-implanted Si, Appl. Phys. Lett. 57(3), 243-245.

58. J. P. de Souza, Yu. Suprun-Belevich, H. Boudinov, C. A. Cima (2001), Mechanical strain and damage in Si implanted with O and N ions at elevated temperatures: Evidence of ion beam induced annealing, J. Appl. Phys. 89(1), 42-46.

59. V. Raineri, S. Coffa etc (2000), He-vacancy interactions in Si and their influence on bubble formation and evolution, Physical Review B, 61(2), 937-945.

60. A. Peeva, P. F. P. Fichtner etc (2002), Gettering of copper in silicon at half of the projected ion range induced by helium implantation, J. Appl. Phys. 91(1), 69-77.

61. A. G. Cullis, T. E. Seidel, R. L. Meek (1978), Comparative study of anneal neon-, argon-, and krypton-ion implantation damage in silicon, J. Appl. Phys. 49, 5188-5198.

62. C. A. Cima, H. Boudinov, etc (2000), Strain development and damage accumulation during neon ion implantation into silicon at elevated temperatures, J. Appl. Phys. 88, 1771-1775.

63. A. Markwitz, V. J. Kennedy, H. Baumann (2003), Formation of micrometer sized crater shaped pits in silicon by low-energy Ne+ implantation and electron beam annealing, Nucl. Instr. And Meth. In Phys. Res. B 206, 179-183.

64. G. F. Cerofolini, R. Balboni, etc (1995), Hydrogen Precipitation in Highly Oversaturated Single-Crystalline Silicon, Phys. Stat. Sol. (a) 150, 539-586.

65. F. A. Cotton, G. Wilkinson (1988), Advanced Inorganic Chemistry, 5th ed., Wiley, New York.

66. Van Wiengen and N. Warmholtz(1956), Physica 22, 849-857.

67 B. Sopori, M. I. Symco, R. Reedy, K. Jones, R. Matson (1997), "Mechanism of Hydrogen Diffusion in Silicon Solar Cells during Forming Gas Anneal", 26th IEEE Photovoltaic Specialist Conference.

68. B. L. Sopori, Y. Zhang, R. Reedy (2002), "H Diffusion for Impurity and Defect Passivation: A Physical Model for Solar Cell Processing", 29th Photovoltaic Specialist Conference.

69. K. J. Chang, D. J. Chadi (1989), "Hydrogen bonding and diffusion in crystalline silicon", Physical Review B, 40, 11644~11653.

70. Chris G. Van de Walle (1994), "Energies of various configurations of hydrogen in silicon", Physical Review B, 49, 4579~4585.

71. B. N. Mukashev, Kh. A. Abdullin, etc (2001), Hydrogen-enhanced clusterization of intrinsic defects and impurities in silicon, Physica B 302-303, 249-256.

72. Yu. V. Gorelkinskii, Kh.A. Abdullin, B.N. Mukashev (1999), Hydrogen-induced extended complexes in silicon, Physica B 273-274, 171-175.

73. H. J. Stein, S. M. Myers, D. M. Follstaedt (1992), Infrared spectroscopy of chemically bonded hydrogen at voids and defects in silicon, J. Appl. Phys. 73, 2755-2768.

74. M. K. Weldon, V. E. Marsico, Y. J. Chabal etc (1997), On the mechanism of the hydrogen-induced exfoliation of silicon, J. Vac. Sci. Tech. B 15(4), 1065-1074.

75. S. J. Jeng, G. S. Oehriein, G. J. Scilla (1988), Hydrogen plasma induced defects in silicon, Appl. Phys. Lett. 53, 1735-1738.

76. J. N. Heyman, J. W. Ager III, E. E. Haller, etc (1992), Hydrogen-induced platelets in silicon: Infrared absorption and raman scattering, Physical Review B 45, 44-48.

77. C. F. Cerofolini, L Meda (1992), Hydrogen-related complexes as the stressing species in high-fluence, hydrogen-implanted, single-crystal silicon, Physical Review B, 46(4), 2061-2070.

78. S K Estreicher, K wells, P A Fedders, Pablo Ordejon (2001), Dynamics of interstitial hydrogen molecules in crystalline silicon, J. Phys.: Condens. Matter 13, 6271-6283.

79. B. Hourahine, R. Jones (1998), Hydrogen molecules in silicon located at interstitial sites and trapped in voids, Physical Review B, 57, R12 666.

80. J. Grisolia, F. Cristiano, G. Ben Assayag, A. Claverie (2001), Kinetic aspects of the growth of platelets and voids in H implanted Si, Nuclear Instruments and Methods in Physics Research B 178, 160-164.

81. B. Hourahine, R. Jones, S. Oberg (1999), Molecular hydrogen traps within silicon, Materials Science and Engineering B 58, 24-25.

82. R. Tonili, A. Monelli, F. Corni, S. Frabboni, G. Ottaviani, G. Queirolo (1996), Silicon interstitials generation during the exposure of silicon to hydrogen plasma, Materials Science and engineering B 36, 158-161.

83. A.W.R. Leith, J. Weber, V. Alex (1999), Formation of hydrogen molecules in crystalline silicon, materials Science and Engineering B 58, 6-10.

84. Paul K. Chu (2003), Semiconductor applications of plasma immersion ion implantation, Plasma Phys. Control Fusion 45, 555-570.

85. Zhineng Fan, Paul K. Chu, et al (1999), Thickness uniformity of Silicon-on-insulator fabricated by plasma immersion ion implantation and ion cut, IEEE Transactions on Plasma Science, 27, 633-636.

86. Zhineng Fan, Xuchu Zeng, Dixon Tat-Kun Kwok, Paul K Chu (2000), Surface hydrogen incorporation and profile broadening caused by sheath expansion in hydrogen plasma immersion ion implantation, IEEE Transactions on plasma science, 28, 371-375.

87. S. A. McQuaid, S. Holgado et al (1997), Passivation, structural modification, and etching of amorphous silicon in hydrogen plasmas, J. Appl. Phys. 81, 7612-7618.

88. J. Lasky (1986), Wafer bonding for silicon-on-insulator technologies, Appl. Phys. Lett. 48, 78-80.

89. M. Shimbo, K. Furukawa, K. Fukuda, K. Tanzawa (1986), Silicon-to-silicon direct bonding method, J. Appl. Phys. 60(8), 2987-2989.

90. Q. Y. Tong, G. Cha, R. Gafiteanu (1994), low temperature wafer direct bonding, J. Microelectromech. Syst. 3, 29-35.

91. K. Mitani, V. Lehmann, R. Stengl, et al(1991), Causes and prevention of temperature-dependent bubbles in silicon wafer bonding, Jpn. J. Appl. Phys. 30(4), 615-622.

92. G. Kissinger, W. Kissinger (1993), Void free silicon bond strengthening in the 200-400 °C range, Sensors and Actuators A 36, 149-156.

93. T. Abe, T. Takei, A. Uchiyama, K. Yoshizawa, Y. Nakazato (1990), Silicon wafer bonding mechanism for silicon-on-insulator, Jpn. J. Appl. Phys. 29(12), L2311-L2314.

94. R. Stengl, T. Tan, U. Gosele (1989), A model for the silicon wafer bonding process, Jpn. J. Appl. Phys. 28(10) 1735-1741.

95. Q. Tong, U. Goesele (1996), A model of low temperature wafer bonding and its applications, J. Electrochem. Soc. 143(5), 1773-1779.

96. T. Hattori, K. Takase, H. Yamagishi (1989), Chemical structures of native oxides formed during wet chemical treatments, Jpn. J. Appl. Phys. 28(2), L296-L298.

97. J. Jiao, D. Lu, B. Xiong, W. Wang (1995), Low temperature silicon direct bonding and interface behaviors, Sensors and Actuator A 50, 117-120.

98. T. Aoyama, T. yamazaki, T. Ito, Nonuniformities of native oxides on Si(001) surfaces formed during wet chemical cleaning, Appl. Phys. Lett. 61(1), 102-104.

99. Tobias Höchbauer (2001), On the Mechanisms of Hydrogen Implantation Induced Silicon Surface Layer Cleavage, Ph D Dissertation, 53-58.